CORA Cork Open Research Archive
Cartlann Taighde Oscailte Chorcaí

Title	Laser-induced graphene for electrochemical sensing applications
Authors	Vaughan, Eoghan
Publication date	2023
Original Citation	Vaughan, E. 2023. Laser-induced graphene for electrochemical sensing applications. PhD Thesis, University College Cork.
Type of publication	Doctoral thesis
Rights	© 2023, Eoghan Vaughan. - https://creativecommons.org/publicdomain/zero/1.0/
Download date	2026-11-14 15:02:13
Item downloaded from	https://hdl.handle.net/10468/15034



UCC
University College Cork, Ireland
Coláiste na hOllscoile Corcaigh

Ollscoil na hÉireann, Corcaigh

National University of Ireland, Cork





Laser-Induced Graphene for Electrochemical Sensing Applications

Thesis presented by

Eoghan Vaughan

for the degree of

Doctor of Philosophy

Tyndall National Institute

University College Cork

Supervisors: Dr Daniela Iacopino and Dr Aidan Quinn
Head of Department: Dr Fatima Gunning

2023

Table of Contents

List of Abbreviations and Acronyms ..... **vi**

Declaration viii

Acknowledgements ..... **ix**

Thesis Abstract ..... **x**

Chapter 1: Introduction **1**

1.1 Abstract 1

1.2 Laser-Induced Graphene 2

1.3 Precursor Materials 9

1.4 Material Characterisation 11

1.5 LIG Electrochemical Sensors 16

1.6 Electrochemical Methods 18

1.7 Conclusions 23

1.8 Thesis outline 23

1.9 References 24

Chapter 2: Visible Laser Scribing Fabrication of Laser-Induced Graphene Electrodes: Morphology, Electrochemical Properties and Applications as Disposable Sensor Platform **33**

2.1 Abstract 33

2.2 Introduction 34

2.3 Experimental Section 37

2.3.1 Materials 37

2.3.2 Electrode Fabrication 37

2.3.3 Characterisation 37

2.3.4 Electrochemical Analysis 38

2.4 Results and Discussion 39

2.4.1 Morphological Characterisation 39

2.4.2 Electrochemical Characterisation 44

2.4.3 Biosensor Performance 54

2.5 Conclusions 61

2.6 References 63

Chapter 3: Laser-Induced Graphene Biosensors for Label-Free Detection of IL-6 ..... **66**

3.1 Abstract 66

3.2 Introduction 67

3.3 Materials and Methods 70

3.3.1 Materials 70
3.3.2 Electrode Fabrication 71
3.3.3 Characterisation 71
3.3.4 Electrode Modification 72
3.3.5 Electrochemical Analysis 72
3.3.6 Electrochemical Interleukin-6 (IL-6) Detection 72
3.4 Results and Discussion 73
3.5 Conclusions 85
3.6 References 86
Chapter 4: Direct Laser Writing of Chitosan-Borax Composites: Towards Sustainable Electrochemical Sensors 91
4.1 Abstract 91
4.2 Introduction 92
4.3 Experimental Section 95
4.3.1 Materials 95
4.3.2 CS-based Films Preparation 95
4.3.3 LIG Fabrication 95
4.3.4 Characterisation 96
4.3.5 Electrochemical measurements 97
4.4 Results and discussion 98
4.4.1 Material optimisation 98
4.4.2 CS/40B-LIG Characterisation 105
4.4.3 Electrochemical characterisation 113
4.5 Conclusions 116
4.6 References 116
Chapter 5: Sustainable Laser Induced Graphene Electrochemical Sensors from Natural Cork for Sensitive Tyrosine Detection 122
5.1 Abstract 122
5.2 Introduction 123
5.3 Experimental section 125
5.3.1 Materials 125
5.3.2 Electrode fabrication 126
5.3.3 Characterisation 126
5.3.4 Electrochemical analysis 127
5.3.5 Electrochemical pre-treatment activation 128
5.4 Results and discussion 128

5.4.1 Device fabrication 128
5.4.2 Laser settings optimisation 129
5.4.3 Material characterisation 132
5.4.4 Electrochemical characterisation 139
5.4.5 Tyrosine detection 145
5.5 Conclusions 151
5.6 References 152
Chapter 6: Summary and Future Work 157
6.1 Summary of Thesis 157
6.2 Future Work 161
6.3 Publications 162

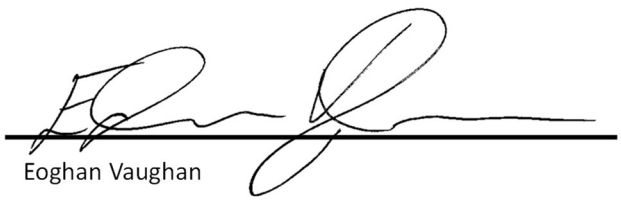
List of Abbreviations and Acronyms

A	Electrode area
AA	Ascorbic acid
ABS	Sodium acetate buffer
Ag/AgCl	Silver/silver chloride reference electrode
ATR-FTIR	Attenuated total reflection-fourier transform infrared
B	Borax
BET	Brunauer–Emmett–Teller
BSA	Bovine serum albumin
C	Concentration
CE	Counter electrode
CNTs	Carbon nanotubes
Cork-LIG	Laser-induced graphene from cork precursor
CS	Chitosan
CS/xB	Chitosan/Borax films with x borax content
CV	Cyclic voltammetry/voltammograms (method or graph)
CVD	Chemical vapour deposition
DA	Dopamine
DA	Depth adjustment (when referring to laser parameters)
$D_{O/R}$	Diffusion coefficient of oxidised/reduced species
DoS	Density of states
DPV	Differential pulse voltammetry
$E_{1/2}$	Formal potential
EDC	1-ethyl-3-(3-dimethylaminopropyl) carbodiimide
EDX	Energy dispersive x-ray spectroscopy
E_i	Initial potential
ELISA	Enzyme-linked immunosorbent assay
E_P	Peak potential
EPPG	Edge plane pyrolytic graphite
E_S	Switching potential
ET	Electron transfer
F	Faraday constant
FBS	Fetal bovine serum
FTIR	Fourier transfer infrared spectroscopy
FWHM	Full width at half maximum
GC/SWCNT	Glassy carbon-modified single wall carbon nanotube
GDL	D-(+)-Gluconic acid δ-lactone
GO	Graphene oxide
HET	Heterogeneous electron transfer
$I_{D/G/2G}$	Intensity of the D, G or 2D Raman peak
IL6	Interleukin-6
I_P	Peak current
IR	Infrared
IR-LIG	Laser-induced graphene produced by an infrared laser
k^0	Electron transfer rate constant
KCl	Potassium Chloride
L_i	Track length for transmission line measurements
LIG	Laser-induced graphene
LOD	Limit of detection
LP	Laser power

M	Molar
n	Number of electrons transferred in reaction, or number of iterations of measurement
N.A.	Numerical aperture
NHS	N-hydroxysuccinimide
PBA	1-pyrenebutyric acid
PBS	Phosphate buffer saline
PI	Polyimide
PI-LIG	Laser-induced graphene produced from polyimide
R	Universal gas constant
R_{CT}	Contact resistance
RE	Reference electrode
R_{SH}	Sheet resistance
SEM	Scanning electron microscopy
SWV	Square wave voltammetry
T	Absolute temperature
TEM	Transmission electron microscopy
TGA	Thermal gravitational analysis
TLM	Transfer length method
Tyr	Tyrosine
UA	Uric acid
UHV	Ultrahigh vacuum
UV	Ultraviolet
UV-LIG	Laser-induced graphene produced by ultraviolet laser
W	Track width for transfer line method
WE	Working electrode
XPS	X-ray photoelectron spectroscopy
α	Charge transfer coefficient
ν	Scan rate
Ψ	Dimensionless parameter used in Nicholas method
ΔE_P	Peak separation

Declaration

This is to certify that the work I am submitting is my own and has not been submitted for another degree, either at University College Cork or elsewhere. All external references and sources are clearly acknowledged and identified within the contents. I have read and understood the regulations of University College Cork concerning plagiarism and intellectual property.



Eoghan Vaughan

Acknowledgements

Firstly, I would like to acknowledge the contributions of my supervisors, Daniela and Aidan. Many thanks are due to them for guidance, advice and direction, and of course for affording me the opportunity to work and study in their group in the first place. I am especially grateful for Daniela's mentorship. I would also like to acknowledge my thesis examiners – Lorraine Nagle and Andrea Lamberti.

There are a few good folk that I have come to know along the way. Cathal once taught me everything that I once knew about electrochemistry. Humble beginnings. I know more now thankfully. Thanks to Jahid for his quiet words of wisdom and for the sandwich animation which he once made in Microsoft PowerPoint. Thanks to Tarun and Veronica for the many seafood dinners that we have shared. Thanks to Alida, Richard and Kathleen for the extended coffee breaks which powered the work that I got done. I appreciate the sacrifices that Claudia made when she ditched her group to join us four lunch. Shane and I co-captained and co-managed and coordinated the take-down of the staff team in the historic 2022 winter instalment of the staff vs students charity soccer match, which will long be remembered. Credit also goes to Patricia for stealing a lamp from The Pavilion, on Carey's Lane, which was inspiring. Other notable contributors to a good time in Tyndall include: Julie, Alessandra, Hassan, Ian, Kimberly, Yunyun, Rob. And more I'm sure. But it is likely that nobody will ever read this section, so nobody will get too sore about not having their name mentioned here.

Thesis Abstract

The fabrication of laser-induced graphene (LIG) allows rapid, inexpensive patterning of electrode designs onto various substrates. LIG is a material whose properties can be tuned by altering the fabrication process, to suit the desired application.

In this thesis, LIG materials were developed using a low-power hobbyist visible laser system, for electrochemical sensing applications. Polyimide (PI) was studied initially as a precursor, with the resultant LIG electrodes showing excellent electrochemical properties. Then LIG electrodes were bio-modified for the sensitive detection of Interleukin 6 (IL-6). Bioplastic precursors, as an alternative to PI, were explored as a potential route to *green-LIG* devices. Chitosan-based sheets were graphitised, and the properties of this LIG were investigated. The electron transfer rates at such electrodes are promising for future device applications. Finally, cork is used as a LIG precursor. Electrochemical cork-LIG sensors showed remarkable properties, with rapid electron transfer rates and a low detection limit for Tyrosine and dopamine.

The results contained in this thesis present fast, inexpensive and eco-friendly options for LIG electrochemical sensor development.

Chapter 1: Introduction

1.1 Abstract

The fabrication of laser-induced graphene (LIG) by direct laser writing is a rapid, inexpensive and versatile method for fabricating 3D graphitic materials. The process allows controlled design of porous structures, particularly suitable for electrochemical sensing.

In this introduction the development of LIG fabrication, from its emergence in 2014 to the wide field of research that now exists, is discussed. The materials from which LIG can be made, and requisite material properties, are investigated. Standard material characterisation methods employed for LIG assessment are examined. This is followed by a discussion of the characteristics of LIG which make it an attractive active material for chemical, and particularly electrochemical, sensing; including how these properties are controlled and manipulated in the fabrication process. We discuss the surface qualities which make LIG electrodes particularly conducive to bio-modification for bio-sensing purposes, and how these surface qualities are controlled in the fabrication procedure. Finally, a brief overview of the methods of electrochemical characterisation that will be employed throughout this thesis is given.

1.2 Laser-Induced Graphene

Low-dimensional allotropes of carbon have been widely studied over the past century. Zero-dimensional fullerenes were first realised by researchers at Rice University in 1986.[1] Fullerenes have found applications in the fields of medicine, biopharmaceuticals and dentistry.[2] One-dimensional carbon nanotubes were discovered in 1991, and are used in areas such as biomedicine, sensors, supercapacitors as well as composites.[3, 4] Graphene was first discovered in 2004 by Novoselov *et al.*, by the mechanical exfoliation of graphite.[5] Graphene is a 2D sheet of six atom rings of sp^2 hybridised carbon. Since its discovery, graphene and graphene-like materials have been extensively researched due to their remarkable physical and chemical properties.[6-12] Graphene is a widely applied in areas such as sensing technology, biotechnology, electronics, energy storage, and publications on graphene are distributed between chemistry, physics, engineering, chemical engineering and material science journals.[13-20]

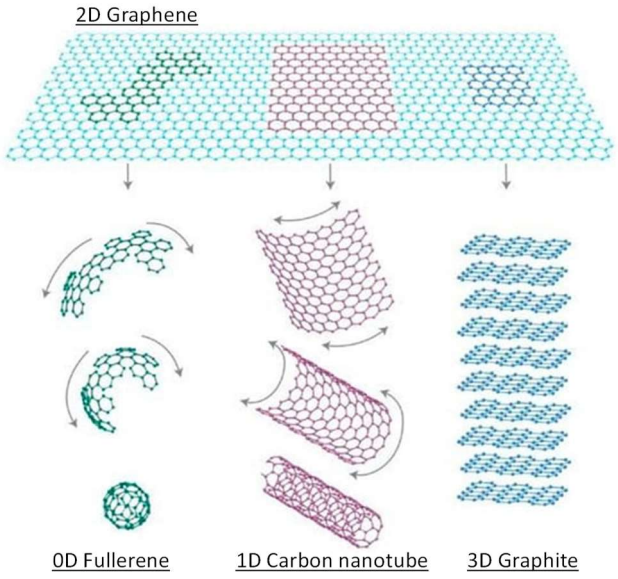


Figure 1.1 2D hexagonal sheet of graphene and derivative carbon allotropes. Reproduced with permission from [21]. Copyright 2007, Nature Publishing Group.

Methods of graphene synthesis include micromechanical exfoliation of graphite,[5] liquid-phase exfoliation,[22] chemical vapour deposition (CVD),[23, 24] pulsed laser deposition.[25] These standard methods are well developed in terms of quality graphene synthesis, but present problems related to developing a time-effective, cost-effective, and scalable procedure.[26, 27] Micromechanical exfoliation of graphite requires the repeated use of scotch tape to peel a smaller and smaller number of graphene layers from the bulk and transferral to a substrate. This method is excellent in terms of isolating few-layer graphene samples, and in terms of structural integrity. While very useful for fundamental studies, this method is time consuming, low-yield, and controlling inter-sample variability in terms of flake size and number of layers is extremely difficult. CVD is a method of depositing gaseous reactants onto a target substrate. CVD of graphene requires a transition metal substrate such as Ni, Pd, Ru or Cu. By this method large area growth of reasonably high quality graphene can be achieved. CVD encounters problems related to removal of the grown graphene layer from the substrate, and in control of defects.[28]

Three dimensional porous graphene structures have proven to be excellent materials for electrodes and energy storage devices.[29] Such structures maintain important electrical qualities of graphene, and additionally provide access to a high-surface area 3D network. 3D porous graphene structures differ from pristine graphene in terms of the defective state of the lattice. The folds and wrinkles that lead to the 3D nature of the material are defect-driven. For electrochemical purposes, it has been shown that impurities in graphene-like electrodes, such as surface functional groups, promote electrocatalytic activity. [30, 31] For example, Yuang *et al.* reported that carboxyl groups on graphene-oxide coated glassy carbon electrodes catalysed the oxidation of glutathione.[30] Stergiou *et al.* compared different graphene electrodes for the

electrochemical detection of ascorbic acid (AA), with graphene oxide sensors showing the lowest overpotential for the reaction. The oxidation of AA occurs via a proton-coupled electron transfer mechanism of the endiol group. The electrocatalytic effect of oxygen groups on the reaction was attributed to their ability to withdraw two protons from the endiol group.[31] Liu *et al.* produced oxygen rich graphene from carbon fibres, whose carboxylic and carbonyl groups were attributed with catalysing the oxygen evolution reaction.[121] In another example, Lu *et al.* reported correlation between the oxygen content of oxidised nanotubes (up to 9% O) and the oxygen reduction reaction activity at the electrode.[122] The catalytic performance was attributed to –COOH groups at armchair edges of the nanotubes and to C-O-C groups at the basal sites. In addition to functional groups, the folded and wrinkled morphology of 3D porous graphene leads to increased exposure of graphitic edge defects, well known to exhibit enhanced electron transfer kinetics versus the basal plane.[32, 33] Methods for producing 3D graphene foams include physical and chemical routes.[34-40] While proving useful for fabrication of high quality 3D graphene, these methods suffer from high energy demand and from being time consuming (hours of treatment per sample), as well as a lack of ability to control the shape of the product.[29] As such, the need for a straightforward, low-cost and scalable method of producing graphene and graphene-like materials is essential.

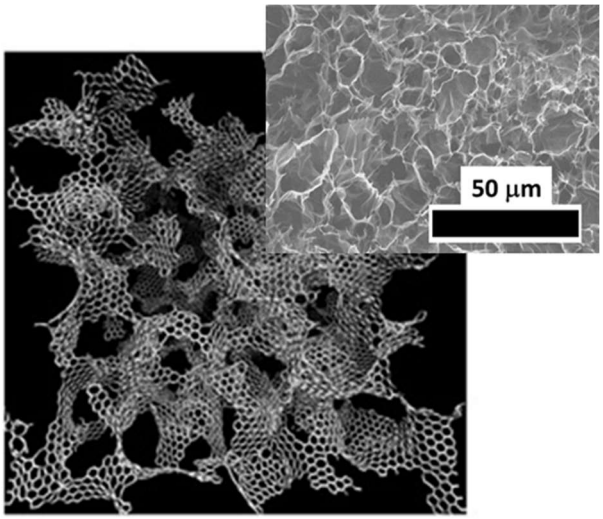


Figure 1.2 3D porous graphene structure model with SEM micrograph of true structure inset. Adapted with permission from [41]. Copyright 2017, Qin et al.

Recently, Lin *et al.* reported on a method of 3D porous graphene fabrication termed laser-induced graphene (LIG).[42] By this method, a commercial polymer tape (Kapton) based on polyimide (PI) is irradiated with an infrared CO_2 laser. The irradiated area is converted by photochemical and photothermal mechanisms to a graphene-like material. The patterning is controlled by the use of computer-controlled laser writer. The use of a laser to pattern graphene features on graphene oxide (GO) has been explored for over a decade,[43-45] however, GO is a high-cost material in bulk.[46] LIG provides a high surface area (~340 m^2g^{-1}), high thermal stability (>900 °C), and low sheet resistance (<10 Ω/sq).[42] The LIG fabrication method offers many advantages: rapid production time; low cost; scalable; perform in ambient; control of design; control of morphology; versatile surface chemistry.

LIG is formed by localised high pressure (>3 GPa), high temperature environments (>2500 °C).[47] This is caused by lattice vibrations due to the incident photon energy. At such high temperatures, C-N, C-O, C-H and C=O bonds break. The remaining aromatic compounds rearrange, forming graphene or graphene-like structures.[42] Given the formation conditions, the remaining carbon atoms do not perfectly arrange into pristine, 2D graphene sheets. The lattice includes pentagonal and heptagonal rings

alongside the hexagonal structure. These defects give rise to the bends and folds in the LIG network.[48] Evidence for the loss of nitrogen and oxygen is commonly seen in XPS spectra of laser graphitised materials, where their relative atomic percentage are massively reduced and sp^2 C becomes the main constituent.[42, 49, 50] With the cleavage of oxygen and nitrogen bonds, these atoms quickly recombine and create gas pockets. The release of these gases are the cause of the porous nature of LIG. It follows that increased laser power should lead to an increased rate of release of gases, and hence larger pore size.[46] Pore sizes have been reported to range from the nanometre scale (< 9 nm) to hundreds of microns (as large as 300 μm) based on factors such as laser power, speed, energy density.[42, 123] Tuning pore size and porosity is useful in many applications, such as electrochemistry, energy storage, and catalysis.[49, 51-53]

Lasing environment plays an important role in the formation of functional groups at LIG surfaces. Most commonly, LIG is produced in air. This availability of oxygen feeds the formation of surface oxygen groups. Surface oxygen content varies widely in the literature, from 5 – 25% by XPS.[49, 54-58] Li *et al.* have shown that surface functionality, and importantly hydrophobicity/hydrophilicity of LIG, can be manipulated by performing the lasing of PI under a controlled environment. [59] In their work they used a chamber and different gaseous environments to produce LIG. From air (15% O) to O_2 (11% O) to Ar and H_2 (~3% O) the oxygen content dropped considerably. They showed by contact angle that high O% LIG has superhydrophilic properties, whereas low O% LIG has superhydrophobic surface. They showed also that an SF_6 environment serves to hinder the formation of C-O bonds, the result being a LIG surface which is, again, superhydrophobic. As well as environment, lasing parameters (laser wavelength, power, speed) have also been shown to affect the LIG produced in terms the presence and concentration of functional groups.[42, 60, 61] Lin *et*

al., in their seminal paper, showed that for their LIG, carbon concentration reaches a maximum at approximately 2.4 W laser power. Past this point carbon content falls while oxygen increases.[42] For electrochemical purposes, a hydrophilic surface is desired to allow access of aqueous electrolyte to the 3D porous, high surface area LIG network, and the presence of oxygenated surface groups have been shown to improve electrocatalytic properties for certain applications.[30, 31]

Laser parameters affect the morphology of LIG, which can range from a relatively thin layer, planar yet porous structure, to an increasingly 3D fibrous structure.[62, 63] Applications have been found for both types. Singh *et al.* showed that fibrous LIG is much more effective than its planar counterpart in inhibiting the growth of bacterial biofilms.[64] Conversely, Vivaldi *et al.* showed that a planar, porous LIG electrode is preferable to a fibrous one for the electrochemical detection of uric acid and tyrosine in sweat, due to the irreproducibility of the fibrous electrode.[65] Murray *et al.* showed that there is a broad area in the parameter space of laser power and scan speed where PI is graphitisable.[62] Sheet resistance ($R_{SH,}$ procedure explained in section 1.4) was used as a parameter to characterise the electrical quality of the LIG produced. Interestingly, they found that there were two regions where minima in R_{SH} were obtained, the regions not correlating to a constant ratio of scan speed and laser power.

LIG was initially, and is most commonly fabricated with infrared CO_2 lasers (λ = 10.6 μm). There is a growing volume of literature based on the use of visible (450 nm, 405 nm) and UV (355 nm) laser sources.[49, 54, 58, 66-69] In their comparative study, Wang *et al.* showed that IR and UV LIG differed in terms of morphology and quality.[70] They showed that in both cases, similar photochemical and photothermal effects caused the conversion of PI to graphitic structures. Santos *et al.* performed a comparative study on electrode performance of IR-LIG and UV-LIG, and found the

IR-LIG to possess faster electron transfer rates and higher sensitivity towards dopamine sensing.[71]

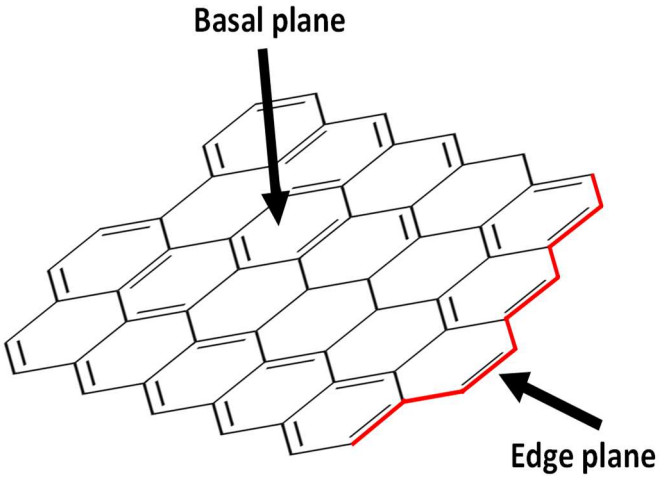


Figure 1.3 Indication of the basal and edge plane in graphene. Terminal highlighted is an example of the edge defect.

Vital to the electrochemistry of LIG, and graphitic materials in general, are defects. We have already discussed how oxygen functionalities contribute to electrocatalytic properties, and how the five- and seven-membered carbon rings in the graphene lattices of LIG lead to the folds and bends that increase the exposure of edge defects. In graphene, we term the plane perpendicular to the graphene sheet the basal plane, and along the graphene sheet the edge plane. This is elucidated in Figure 1.3. Edge defects are the terminals of the graphene sheets within the LIG structure. They have been shown to be the most reactive sites for chemical activity of graphitic materials.[33] Due to the termination of the lattice, edges are disordered, and are characterised by the presence of sp^3 hybridised rings, and oxygen functional groups such as carboxyl, carbonyl and ether groups.[72] In graphene, edge defects can be oxidised in air and absorbed oxides at basal sites have been shown to migrate to edge sites.[73] Due to this, oxygen content in LIG electrodes has been used to indirectly account for a high density of edge defects, towards an explanation of fast electrochemical reaction kinetics.[71]

It is clear that the surface qualities of LIG are variable. Its fabrication is a tuneable process, and the qualities sought from the material are obtained by careful optimisation of the procedure.

1.3 Precursor Materials

In their initial investigation of LIG, Lin *et al.* tested fifteen different polymer structures, and found two to be graphitisable.[42] The requisite property was the presence of aromatic repeat units. These provided the sp^2 hybridised C six-membered rings which dominate the form of LIG. PI is the most commonly used precursor for LIG, and its chemical structure is shown in Figure 1.4. Since then many high-temperature thermoplastics and thermoset materials have been found to be graphitisable, by modifying the LIG technique using defocused laser sources or multiple laser passes, for example.[74]

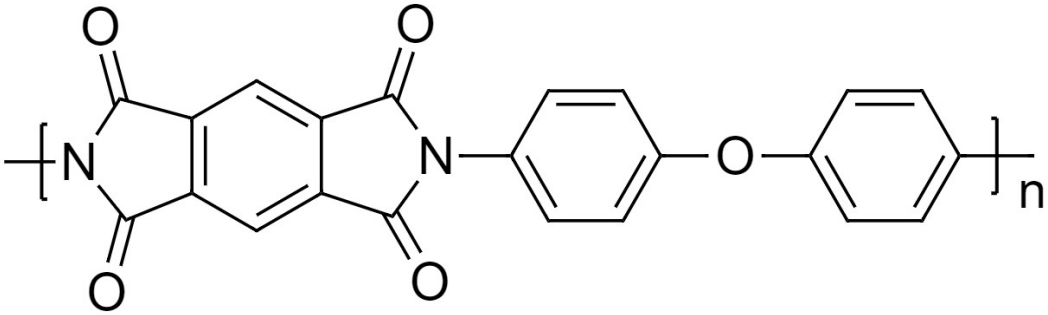


Figure 1.4 Chemical structure of polyimide repeating unit.

Beyond PI, phenolic resin, polyetherimide and polydimethylsiloxane are synthetic polymers found to be successful precursors to LIG.[42, 67, 75] Considering the extent of research in the field of LIG, the sustainability of fabrication methods must be considered. This means searching beyond synthetic and fossil-fuel derived polymer precursors, to realise a 'Green-LIG'. Bioplastics use naturally occurring polymers such as polysaccharides as an alternative to petroleum. Examples of using bioplastics for LIG have been shown for lignin and chitosan, both materials producing materials with

electrochemical applications. Lei *et al.* produced nitrogen-doped LIG on a lignin-based film, with excellent electron transfer properties.[76] By modification with Prussian blue and catalytic enzymes, they successfully detected glucose and lactate. Larrigy *et al.* developed a bioplastic recipe which allowed them to produce a flexible and water-soluble substrate.[77] The material was converted to LIG by a 3-step lasing process, and they showed it to be suitable for use as a dissolvable electrochemical platform.

Green-LIG has also been produced from natural materials without processing. Wood, leaves, paper, coal, cork and even food such as bread, coconut shells and potato peels have been successfully converted.[54, 74, 78-82] The presence of biopolymers cellulose and lignin provide the necessary carbon content. Chyan *et al.* showed that carbon-containing precursors can be turned to graphene by a two-step lasing process.[74] The first step results in the formation of amorphous carbon, the second in formation of LIG. They claim that any carbon-containing precursor which can be converted to amorphous carbon can be converted to LIG by this method. The fabrication of LIG from wood resulted in high quality LIG with R_{SH} as low as 10 Ω/sq. An inert atmosphere was required for these results, as laser-treatment in air led to ablation of the wood. It was noted that wood with higher lignin content resulted in higher quality LIG. This confirms the importance of a cross-linked aromatic structure in the precursor. Also noted by Ye *et. al* are the favourable qualities of lignin as an carbon-containing biopolymer over cellulose and hemicellulose.[78] The reactivity of aliphatic moieties of cellulose cause faster decomposition when laser treated, compared with lignin.

Cork typically has higher lignin content than wood, as well as a lower content of cellulose and hemicellulose.[83, 84] Suberin is the major biopolymer constituent of cork,

which is made up of aliphatic and aromatic domains. From these properties we understand why cork is an excellent candidate for a LIG precursor. Imbrogno *et al.* used a 450 nm laser to create supercapacitors on cork stoppers.[54] Cork-LIG has also been used for triboelectric generators.[85] Carvalho *et al.* applied cork-LIG as a piezoresistive sensor for human gait measurements.[86] Cork-LIG has been shown to be of excellent quality by Raman spectroscopy and by IR measurements, with R_{SH} values of 10 Ω/sq.[57] Despite these attractive characteristics, cork-LIG has not yet been exploited as an active material for chemical sensing.

1.4 Material Characterisation

The quality of LIG is most often characterised by x-ray photoelectron spectroscopy (XPS), Raman spectroscopy, scanning electron microscopy (SEM), and sheet resistance. Together, these techniques inform us of the elemental nature, bonding structure, chemical structure, crystallinity, morphology, hydrophobicity, and electrical properties of the material.

Typical SEM micrographs of LIG are displayed in Figure 1.6. In panel a) we see that the porosity of LIG is revealed, the nature of which suggests their formation by exploding pockets of trapped gas. High-magnification images can provide information relating to pore size (more accurately assessed by Brunauer-Emmett-Teller analysis). We see peaks and valleys, evidence of the raster movement of the laser head when scribing the design. Cross sectional SEM, as displayed in Figure 1.6b, is used to determine the depths of LIG formations. An immediately notable difference between the surface nature in Figure 1.6a and c is observed: in a) we see LIG as a 3D structure, compact and porous; different fabrication conditions of the LIG in c) have resulted in a fibrous LIG.[63]. For varying methods, materials, and applications, SEM is necessary to reveal the microstructure which contributes to the material's changing properties.

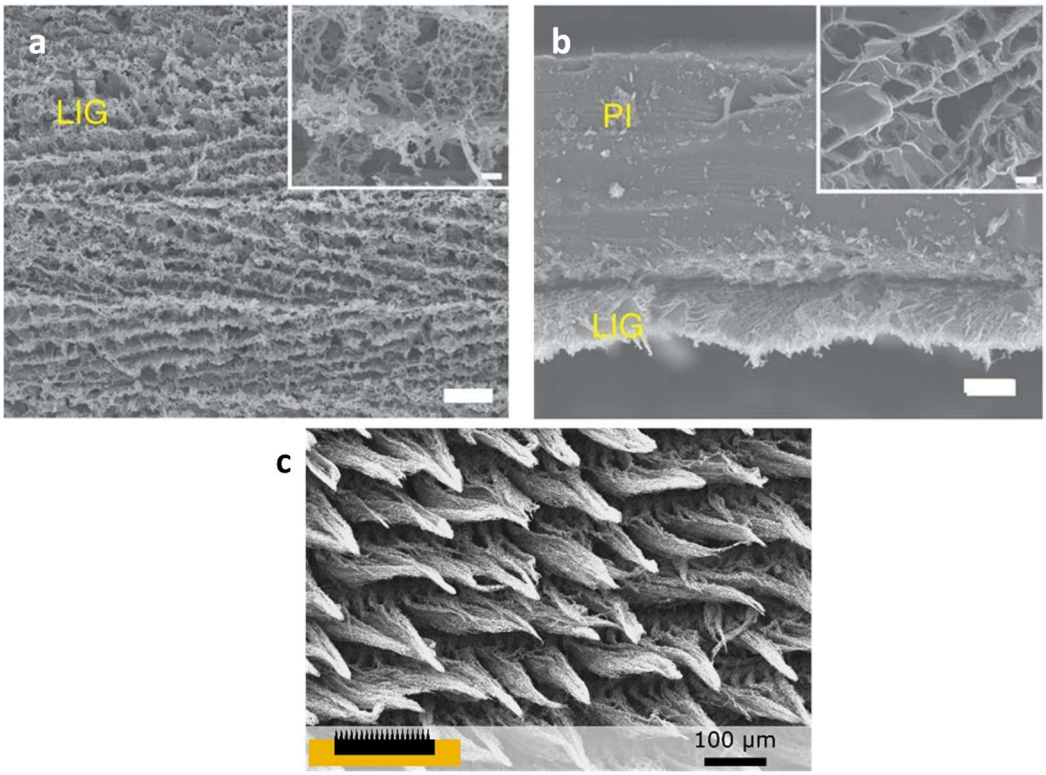


Figure 1.6 SEM micrographs of **a)** LIG surface, scale bar 10 µm; inset is high-magnification image with scale bar 1 µm; **b)** LIG cross section showing depth of formation on PI, scale bar 20 µm; inset is corresponding high-magnification image, scale bar 1 µm; **c)** fibrous LIG surface. Panels a) and b) adapted with permission from [42]. Copyright 2014, Nature Publishing Group; panel c) adapted from [63] Copyright 2020, American Chemical Society, Washington, DC.

XPS is one of the most widely applied surface analysis techniques. The operational principle is based on the energy distribution of photon-excited electrons of surface atoms. The binding energies of electrons are characteristic of chemical states of the atoms, which is used to identify elements and their bonding states. XPS informs us about the surface states of a material (1 – 10 nm probing depth).[120] Regions of interest in an XPS survey of LIG samples are generally the C1s and O1s peaks. For doped samples, regions such as N1s or B1s may also be of interest. The C1s peak of LIG is commonly deconvoluted into five contributions: C-C sp^2, C-C sp^3, C-OH, and C=O. (see Figure 1.7) As many as seven peaks can be assigned – an extra pi-pi transition peak and a COOH peak.[87] The C-C sp^2 peak is nominally assigned at a binding energy of 284.5 eV; the C-C sp^3 peak is around 285 eV.[88, 89] Positive shifts in binding energy

of 1.5, 2.5 and 4 eV are typical for C-OH, C=O and COOH functional groups, respectively, though the exact shifts are not precise.[90] For LIG, a high content of sp^2 C-C reflects successful conversion to a graphitic material. The ratio of sp^2 C-C to other C contributions is a good indicator of the quality of the lasing process. Information relating to the nature of the sp^2 bonding – whether the material is more graphene- or graphite-like – can be obtained from the KLL Auger spectrum. The so called D parameter is determined as the difference between the maximum and minimum of the first derivative of the C KLL spectrum.[91] D values of 13.5 – 15 eV are typical for graphene, whereas values around 21 eV are typical for graphite.[92]

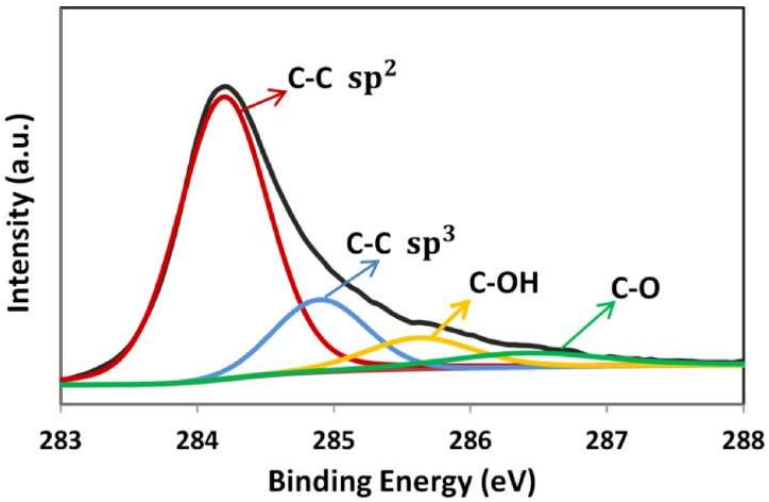


Figure 1.7 Typical deconvoluted C1s spectrum with bond assignments indicated. Reproduced with permission from [93]. Copyright 2015, IOP Publishing Ltd.

Concerning the O1s peak, there is less of an emphasis on its deconvolution and peak assignment in LIG literature, rather the O content of a sample is important. As mentioned before, O content of a LIG sample relates to hydrophilicity, to chemical reactivity, as well as electrochemical activity. The ratio of C/O by XPS is, therefore, very useful information.

Raman spectroscopy is an excellent partner to XPS. In graphene research, Raman spectroscopy can be used for determining the number of layers, defectiveness, disorder and overall quality.[94] For pristine single layer graphene, the Raman signature displays

two peaks: G and 2D.[95] The G band is due to the high frequency E_{2g} phonon – a degenerate in-plane optical mode. The G peak is not dispersive, meaning its position does not vary with phonon excitation energy, and always lies in the range 1500 – 1630 cm^{-1}.[96] The 2D band is an overtone of the D peak, which is activated by the breathing modes of the hexagonal graphene ring. The D peak is not Raman active without defects, but the 2D peak is always present due to the conservation of momentum being fulfilled by two phonons with opposite wave vectors.[94] The Raman signatures of pristine single layer and of disordered multilayer graphene are displayed in Figure 1.8. The disordered spectrum has many more active modes arising from defect activation. The D peak is dispersive, and is generally centred around 1355 cm^{-1}. The intensity ratio of the D to G peak (I_D/I_G) is a crucial parameter in classifying the degree of disorder in a graphitic sample.[96] Ferrari and Robertson developed a three class framework for categorising disorder by monitoring I_D/I_G and correlating this data with the G band position. Samples are classed from graphite to nanocrystalline graphite to low sp^3 amorphous carbon to high sp^3 amorphous carbon. From pristine graphite (I_D/I_G = 0), with increasing disorder I_D/I_G will increase. Crystallites become smaller and more distorted, and aromatic rings may open. At a certain point I_D will begin to fall in relation to I_G, because the value of the latter is related to modes of sp^2 atoms, while I_D is related to six-membered rings. This means that for increasing disorder in amorphous carbon, I_D/I_G will fall (the opposite of the initial case).[96] This apparent anomaly is most easily clarified for LIG materials by inspection of the 2D peak. For the amorphous carbon region along this disorder trajectory, the 2D peak becomes diffused or even disappears. LIG materials are most often reported as containing nanocrystalline graphitic domains.

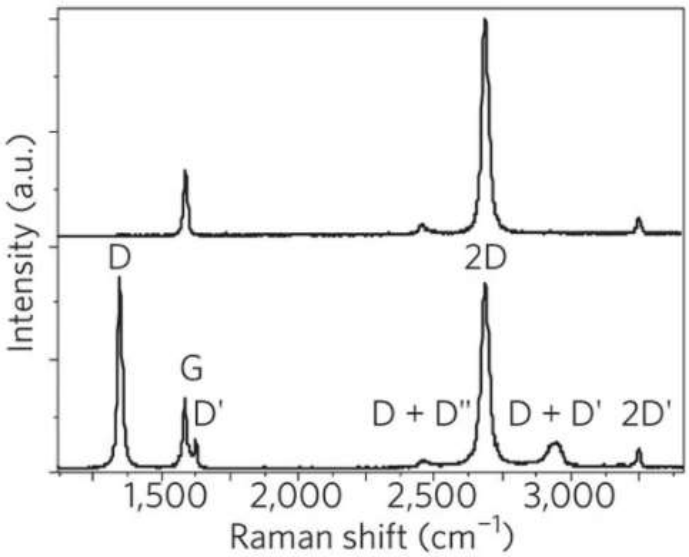


Figure 1.8 Raman signature of pristine (top) and disordered (bottom) graphene. Reproduced with permission from [94]. Copyright 2013, Nature Publishing Group.

Sheet resistance ($R_{SH,}$ measured in Ω/sq.) of a film is determined by transmission line measurements (TLM). TLM structures with a defined aspect ratio are probed for resistance measurements at varying lengths, L_i. The track resistance (R_i) of a length of material between two probes is related to L_i via:

$$R_i = R_{CT} + (R_{SH} \times L_i)/W$$

where R_{CT} is the contact resistance, R_{SH} is the sheet resistance of the sample, and W is the track width. Taking several measurements, a plot f R_i versus L_i allows the determination of R_{SH} and R_{CT} by linear regression. TLM is commonly applied to LIG materials because their dimensions allow them to be treated as thin films. Values of R_{SH} can vary widely – from <15 Ω/sq to >100Ω/sq.[42, 82] As always, such physical properties of LIG depend on the lasing conditions and the precursor material. It is desirable to achieve a low R_{SH} value for most LIG applications, as a highly resistive LIG electrode will also behave as a disruptive circuit element.

1.5 LIG Electrochemical Sensors

Electrochemical sensors are an attractive sensing option because of their simplicity and low cost. LIG has proven an especially useful electrode material because of its tuneable surface and ease of control over electrode design. As-fabricated LIG (without surface enhancement/modification) have been shown to exhibit rapid electron transfer kinetics towards many reactions. Characterising and optimising a LIG electrode is a multifactor process. Typically, electron transfer kinetics of the ferri/ferrocyanide reaction ($[Fe(CN)_6]^{3-/4-}$) or the hexaammineruthenium reaction ($[Ru(NH_3)_6]^{2+/3+}$) are used to characterise LIG electrodes, as these are well understood, reversible one-electron reactions. Achieving an electrode surface and design with fast kinetics for these reactions indicates on optimised set up, which can then be used for more complex analytes. For example, Kulyk *et al.* characterised their LIG electrode using both of these redox couples, before sensing uric acid.[97] Similarly, Santos et al. used $[Fe(CN)_6]^{3-/4-}$ and $[Ru(NH_3)_6]^{2+/3+}$ before successfully sensing dopamine in the presence of uric acid and ascorbic acid.[71]

Such characterisations and optimisations of raw LIG electrodes are vital for further purposing of the electrodes. Electrochemical sensors are important for medical purposes. Electrochemical biosensors provide a low-cost and fast alternative to established laboratory methods such as colorimetric and fluorescence assays. In comparison, electrochemical methods do not require such arduous analysis of results, equipment can be portable rather than lab-based, and response times are rapid which allows for real-time, in situ detection.[98-100] Biological fluids are complex solutions, which contain many species capable of undergoing redox reactions. Some such analytes may be individually detected at electrodes with fast enough charge transfer kinetics.[49, 101-103] More commonly, functionalisation of the surface with biological

compounds is necessary for the required selectivity. LIG surfaces are readily bio-modified due to their defective state and high surface area.[104]

Antibodies recognise unique molecules. Successful attachment of antibodies to LIG electrodes have resulted in highly selective sensors. The presence of antigen-antibody complexes at an electrode surface alters charge transfer capabilities, a feature, which can be exploited for detection and quantitative analysis. Soares *et al.* modified their LIG electrode with polyclonal antibody *anti-salmonella* to monitor salmonella enterica in chicken broth.[98] Change in transfer resistance, determined by electrochemical impedance spectroscopy, was used to quantify salmonella levels. The detection limit was 13 ± 7 CFU mL^{-1} with a response time of 22 minutes. The functionalisation procedure is outlined in Figure 1.5. The successful immobilisation of the salmonella antibodies was facilitated by EDC/NHS treatment of the electrode surface, which then allowed for carbodiimide cross-linking with the antibody. By a similar mechanism, Oliveira *et al.* attached SARS-Cov-2 specific antigen to a LIG electrode for the detection of COVID-19 antibodies.[105] Current responses by differential pulse voltammetry at the functionalised LIG sensors was used to distinguish positive and negative COVID samples in human blood serum.

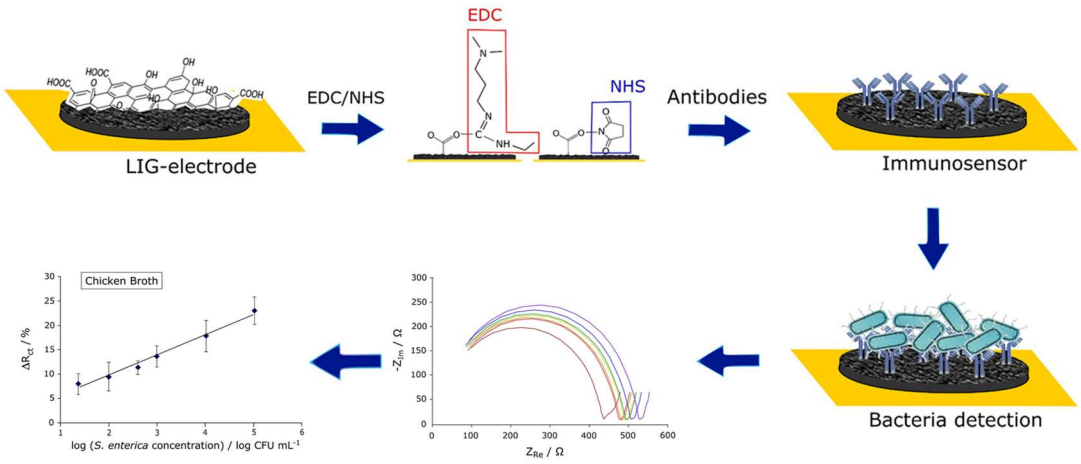


Figure 1.5 Schematic of the surface functionalisation process. Adapted with permission from [98]. Copyright 2022, American Chemical Society.

Enzymatic electrochemical sensing is another method of achieving selectivity in biosensors. Whereas antibody/antigen electrochemical sensors can work by enhancing reactions or by inhibiting access to the electrode surface, enzymatic electrochemical sensors work by using an enzyme to catalyse the oxidation of a particular molecule. LIG electrodes are particularly suitable for such enzymatic modification. For example, glucose oxidase was used to functionalise LIG electrodes made by CO_2 and by UV lasers, for selective glucose detection.[106, 107] Chitosan was used to facilitate the enzyme modification, which was similarly the case for lactate sensing by modifying LIG with lactate oxidase.[108]

Numerous other examples of LIG functionalisation exist in the literature,[109-111] extending the concept of LIG as a versatile material beyond fabrication parameters. Not only may the surface characteristics be tuned to suit the purpose of an as-produced device, but also to better facilitate modification, if desired.

Important also, when considering LIG as a material for biosensing, is that LIG has been proven to be biocompatible. d'Amora *et al.* investigated the impact of LIG materials on biological models with high homology with humans (zebrafish).[124] Their study found that LIG did not show toxic effects or interfere with the development of specimens, even when administered at high concentrations (100 mg ml^{-1} in E3 medium). These findings prove that LIG devices provide a safe route option for biological sensing devices.

1.6 Electrochemical Methods

The most prominent role played by LIG devices is in electrochemical sensing. We have discussed how the surface properties of LIG are conducive to functionalisation, allowing sensitive detection of biomolecules such as dopamine, lactate, glucose, thrombin and salmonella.[24, 108, 111-114] These functionalised electrodes are successful

not only due to the surface properties of LIG which make it easily modifiable, but also due to the excellent electrochemical properties of the raw material. When we speak of excellent electrochemical properties in relation to LIG, more specifically we mean electron transfer rate, current response and active surface area. The simplest method of characterising an electrode is by cyclic voltammetry (CV).

CV is a potential sweep method where the potential of the working electrode is varied linearly between two values (switching potentials). For one cycle, the time-potential profile is simply a triangle – from the initial potential, E_i, to the switching potential, E_s, and back to E_i, as shown in Figure 1.9a. The parameters of interest when running a CV scan are the potential window (E_i - E_s) and the scan rate, ν, in V s^{-1}. ν is the rate of change of potential with respect to time, i.e. the slope of the potential profile of Figure 1.9a. The oxidation and/or reduction potentials of the analyte of interest must lie in the set potential window, and importantly the electrode must undergo no interfering reactions in this range (reduction of surface groups for example, or hydrolysis of water in aqueous solutions). Peak current (I_P) and peak separation (ΔE_P) depend on ν, and measuring their response to varying ν allows important insight into an electrodes fundamental properties.[115]

Current is plotted against potential of the working electrode, relative to a stable reference, commonly Ag/AgCl. The Ag/AgCl electrode is based on the reversible redox reaction between solid silver and solid silver chloride in a chloride salt solution:

$$AgCl(s) + Ag(s) + e^- <=> Ag(s) + e^- + Cl^- + Ag^+$$

The potential of this cell depends on the activity (or effectively the concentration) of the Cl^- ion. For a standard Ag/AgCl reference electrode, the solid electrode is contained within a glass cell surrounded by an electrolyte solution containing chloride of defined concentration, giving a stable reference potential. When using Ag/AgCl

paste as a quasi-reference electrode, the reference potential can vary with solution due to changing Cl^- concentrations (Cl^- activity).

LIG is generally restricted to macro-electrode fabrication. The typical shape of a CV for a macro-electrode is displayed in Figure 1.9b. Peaks in current are due to additional electron flow from charge transfer reactions (faradaic) – oxidation of the analyte species at higher potentials and reduction at lower potentials. For macro-electrodes, the current drops after the peak due to the reaction being diffusion limited – the semi-infinite linear diffusion regime does not allow the rate of unreacted analyte reaching the electrode surface to reach a steady-state with the rate of electron transfer. For microelectrodes, for example, a sigmoidal response is achieved because of more efficient mass transport to the electrode surface – radial diffusion of electrolyte allows for a steady state current to be reached. The peaks are built on a current caused by background processes (non-faradaic), mainly charging at the electrode/electrolyte interface. This interface behaves as a double layer capacitor, as charged electrolytic species continuously migrate towards the surface as its potential changes. Peak currents are read using a baseline subtraction to negate the contribution of the charging current. The baseline is extrapolated from the linear region preceding faradaic reactions. A typical CV profile is displayed in Figure 1.9b.

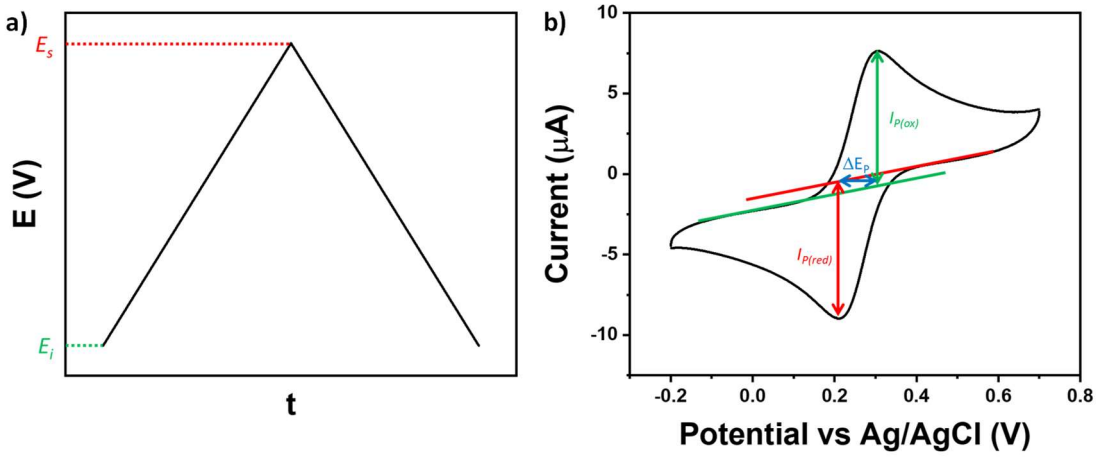


Figure 1.9 a) Potential profile for CV **b)** Typical CV with charging current baselines, peak currents, and peak separation indicated.

Electrochemical reactions occur only at the electrode/solution interface – heterogeneous reactions. Generally, reaction rates depend on mass transfer of analyte to the electrode, and kinetics of electron transfer at the surface. In the absence of stirring (convection), mass transfer is contributed to by migration and diffusion. Migration is the movement of molecules in response to a potential gradient; diffusion is the movement of molecules in response to a concentration gradient. The situation is simplified in most electrochemical experiments by the addition of an excess concentration of non-electroactive ions – the supporting electrolyte. The excess ions effectively eliminate the potential gradient, allowing us to view diffusion of analyte as the dominant mass-transfer mechanism.[115]

The kinetics of electron transfer at the electrode surface are characterised by the standard heterogeneous electron transfer (HET) rate constant, k^0 (cm s^{-1}). Reversible electrochemical reactions exhibit a ΔE_P value $59/n$ mV at 25 °C, where n is the number of electrons involved in the charge transfer reaction.[115] This value is often achieved for CV at LIG electrodes with high k^0 at low values of ν. Increasing ν sufficiently leads to the electron transfer rates becoming competitive with the rate of the changing potential.[116] The effect is a positive shift in the oxidation peak and a negative shift in the reduction peak; overall an increase of ΔE_P. The range where electrode reactions are deemed *quasi-reversible* (200 mV > ΔE_P > 60 mV) is useful for investigating the kinetics of electrode reactions. This is done by using the method of Nicholas, whereby ΔE_P and ν are related to k^0 via the dimensionless ψ parameter:[116]

$$\Psi = \mathrm{k}^0\left(\frac{D_O}{D_R}\right)^{\frac{\alpha}{2}}\sqrt{\frac{RT}{n\pi F D_O \nu}}$$

where $D_{O/R}$ are the diffusion coefficients of the oxidised and reduced analyte forms respectively, α is the charge transfer coefficient, R is the universal gas constant, F is Faraday's constant and n is the number of electrons involved in the reaction. Ψ is derived from ΔE_P by the equation:[117]

$$\Psi = \frac{(-0.6288 + 0.0021n \quad _P)}{(1 - 0.017n\Delta E_P)}$$

Performing such a characterisation of a standard redox couple, $[Fe(CN)_6]^{3-/4-}$ for example, establishes a method of comparison of the electrochemical performance of different LIG electrodes and with other electrode materials.

For a diffusion-controlled reversible reaction, the response of the peak current in CV with changing ν is defined by the Randles-Ševčík equation:[118, 119]

$$I_P = 0.4463nFAC\left(\frac{nF\nu D}{RT}\right)^{1/2}$$

where A is the active electrode area (cm^2) and all other symbols retain their previous definition. Our first inference from this equation is that $I_P \propto \nu^{1/2}$. Such linear plots readily confirm reversible behaviour of electrode reactions, in agreement with theory. Additionally, the equation allows for a calculation of the electroactive surface area of the electrode. Due to the surface microstructure of LIG, analyte has access to a larger area than the apparent 2D area of an electrode. Examination of I_P informs us of the interaction of the analyte and the peaked/valleyed and porous structure.

CV is an excellent method for determining qualitative behaviour at an electrode. Once CV has been used for such characterisation purposes, other voltammetric or amperometric methods are more suited for quantitative analysis. This is because peak current measurements in CV are not precise enough for such evaluations. Peaks are superimposed on a background charging current, and there is uncertainty involved in correcting for this. Choronoamperometry, electrochemical impedance spectroscopy, differential pulse voltammetry, and square wave voltammetry are some of the most

commonly used techniques, with both voltammetric techniques having the advantage of no influence of charging phenomena.[115]

1.7 Conclusions

We have seen that LIG is versatile material. With a desired application in mind, the fabrication process is readily altered to produce an optimal form of LIG. The field is expanding, with research driven by use of new laser systems, exploration of new applications, and the use of sustainable precursor materials.

1.8 Thesis outline

In this thesis, LIG is produced by a low-power and inexpensive 'hobbyist' laser cutter.

In chapter two, polyimide is used as precursor material. The LIG produced is characterised extensively. The exceptional electrochemical properties of this LIG are revealed. Dopamine sensing in the presence of interfering species is used as a showcase of the capabilities of this material as electrochemical sensor.

The work of chapter three is built off the raw-LIG as produced in chapter one. With changing electrode design for a new purpose, a brief characterisation is again performed. This raw LIG is bio-functionalised for the sensitive detection of IL-6. This is the first example of IL6 detection by a LIG electrochemical sensor.

In chapter four, an investigation of sustainable precursor materials begins. Graphitisation of films, based on the bio-polymer chitosan, is performed. The recipes for the films is varied in content, and the resulting LIG features are characterised to find the optimal recipe and conditions.

In chapter five, the remarkable electrochemical properties of LIG from natural cork are revealed. Firstly an optimisation of laser settings is performed, followed by an extensive material characterisation. Sensitive detection of tyrosine in the presence of

interfering species is used to showcase the remarkable prospects for this material as an electrochemical sensor. This is the first example of such a sensitive LIG device produced from entirely renewable sources without chemical pre-treatment.

1.9 References

1. Kroto, H.W., J.R. Heath, S.C. O'Brien, R.F. Curl, and R.E. Smalley, *C60: Buckminsterfullerene.* Nature, 1985. **318**(6042): p. 162-163.
2. Bhakta, P. and B. Barthunia, *Fullerene and its applications: A review.* Journal of Indian Academy of Oral Medicine and Radiology, 2020. **32**(2): p. 159-163.
3. Iijima, S., *Helical microtubules of graphitic carbon.* Nature, 1991. **354**(6348): p. 56-58.
4. Rathinavel, S., K. Priyadharshini, and D. Panda, *A review on carbon nanotube: An overview of synthesis, properties, functionalization, characterization, and the application.* Materials Science and Engineering: B, 2021. **268**: p. 115095.
5. Novoselov, K.S., A.K. Geim, S.V. Morozov, D. Jiang, Y. Zhang, S.V. Dubonos, I.V. Grigorieva, and A.A. Firsov, *Electric field effect in atomically thin carbon films.* Science, 2004. **306**(5696): p. 666-9.
6. Mayorov, A.S., R.V. Gorbachev, S.V. Morozov, L. Britnell, R. Jalil, L.A. Ponomarenko, P. Blake, K.S. Novoselov, K. Watanabe, T. Taniguchi, and A.K. Geim, *Micrometer-Scale Ballistic Transport in Encapsulated Graphene at Room Temperature.* Nano Letters, 2011. **11**(6): p. 2396-2399.
7. Liu, F., P. Ming, and J. Li, *Ab initio calculation of ideal strength and phonon instability of graphene under tension.* Physical Review B, 2007. **76**(6): p. 064120.
8. Lee, C., X. Wei, J.W. Kysar, and J. Hone, *Measurement of the Elastic Properties and Intrinsic Strength of Monolayer Graphene.* Science, 2008. **321**(5887): p. 385-388.
9. Morozov, S.V., K.S. Novoselov, M.I. Katsnelson, F. Schedin, D.C. Elias, J.A. Jaszczak, and A.K. Geim, *Giant Intrinsic Carrier Mobilities in Graphene and Its Bilayer.* Physical Review Letters, 2008. **100**(1): p. 016602.
10. Balandin, A.A., *Thermal properties of graphene and nanostructured carbon materials.* Nature Materials, 2011. **10**(8): p. 569-581.
11. Bunch, J.S., S.S. Verbridge, J.S. Alden, A.M. van der Zande, J.M. Parpia, H.G. Craighead, and P.L. McEuen, *Impermeable Atomic Membranes from Graphene Sheets.* Nano Letters, 2008. **8**(8): p. 2458-2462.
12. Moser, J., A. Barreiro, and A. Bachtold, *Current-induced cleaning of graphene.* Applied Physics Letters, 2007. **91**(16): p. 163513.
13. Ye, R., Z. Peng, T. Wang, Y. Xu, J. Zhang, Y. Li, L.G. Nilewski, J. Lin, and J.M. Tour, *In Situ Formation of Metal Oxide Nanocrystals Embedded in Laser-Induced Graphene.* ACS Nano, 2015. **9**(9): p. 9244-9251.
14. Bae, S.-H., Y. Lee, B.K. Sharma, H.-J. Lee, J.-H. Kim, and J.-H. Ahn, *Graphene-based transparent strain sensor.* Carbon, 2013. **51**: p. 236-242.

15. Olabi, A.G., M.A. Abdelkareem, T. Wilberforce, and E.T. Sayed, *Application of graphene in energy storage device – A review.* Renewable and Sustainable Energy Reviews, 2021. **135**: p. 110026.
16. Nag, A., A. Mitra, and S.C. Mukhopadhyay, *Graphene and its sensor-based applications: A review.* Sensors and Actuators A: Physical, 2018. **270**: p. 177-194.
17. Yam, K.M., N. Guo, Z. Jiang, S. Li, and C. Zhang *Graphene-Based Heterogeneous Catalysis: Role of Graphene*. Catalysts, 2020. **10**, DOI: 10.3390/catal10010053.
18. Zhu, J., D. Yang, Z. Yin, Q. Yan, and H. Zhang, *Graphene and Graphene-Based Materials for Energy Storage Applications.* Small, 2014. **10**(17): p. 3480-3498.
19. Pal, K., A. Si, G.S. El-Sayyad, M.A. Elkodous, R. Kumar, A.I. El-Batal, S. Kralj, and S. Thomas, *Cutting edge development on graphene derivatives modified by liquid crystal and CdS/TiO2 hybrid matrix: optoelectronics and biotechnological aspects.* Critical Reviews in Solid State and Materials Sciences, 2021. **46**(5): p. 385-449.
20. Aïssa, B., N.K. Memon, A. Ali, and M.K. Khraisheh, *Recent Progress in the Growth and Applications of Graphene as a Smart Material: A Review.* Frontiers in Materials, 2015. **2**.
21. Geim, A.K. and K.S. Novoselov, *The rise of graphene.* Nature Materials, 2007. **6**(3): p. 183-191.
22. Cui, X., C. Zhang, R. Hao, and Y. Hou, *Liquid-phase exfoliation, functionalization and applications of graphene.* Nanoscale, 2011. **3**(5): p. 2118-2126.
23. Mattevi, C., H. Kim, and M. Chhowalla, *A review of chemical vapour deposition of graphene on copper.* Journal of Materials Chemistry, 2011. **21**(10): p. 3324-3334.
24. Chen, Z., W. Ren, L. Gao, B. Liu, S. Pei, and H.-M. Cheng, *Three-dimensional flexible and conductive interconnected graphene networks grown by chemical vapour deposition.* Nature Materials, 2011. **10**(6): p. 424-428.
25. Tite, T., C. Donnet, A.S. Loir, S. Reynaud, J.Y. Michalon, F. Vocanson, and F. Garrelie, *Graphene-based textured surface by pulsed laser deposition as a robust platform for surface enhanced Raman scattering applications.* Applied Physics Letters, 2014. **104**(4): p. 041912.
26. Ramesh, R., *Graphene: Fabrication Methods, Properties, and Applications in Modern Industries*, in *Graphene Production and Application*, A. Sadia, M.S. Akhtar, and S. Hyung-Shik, Editors. 2020, IntechOpen: Rijeka. p. Ch. 2.
27. Soldano, C., A. Mahmood, and E. Dujardin, *Production, properties and potential of graphene.* Carbon, 2010. **48**(8): p. 2127-2150.
28. Huet, B., J.-P. Raskin, D.W. Snyder, and J.M. Redwing, *Fundamental limitations in transferred CVD graphene caused by Cu catalyst surface morphology.* Carbon, 2020. **163**: p. 95-104.
29. Wang, C.-C., J. Liang, Y.-H. Liao, and S.-Y. Lu, *3D Porous Graphene Nanostructure from a Simple, Fast, Scalable Process for High Performance Flexible Gel-Type Supercapacitors.* ACS Sustainable Chemistry & Engineering, 2017. **5**(5): p. 4457-4467.

30. Yuan, B., X. Zeng, C. Xu, L. Liu, Y. Ma, D. Zhang, and Y. Fan, *Electrochemical modification of graphene oxide bearing different types of oxygen functional species for the electro-catalytic oxidation of reduced glutathione.* Sensors and Actuators B: Chemical, 2013. **184**: p. 15-20.
31. Stergiou, D.V., E.K. Diamanti, D. Gournis, and M.I. Prodromidis, *Comparative study of different types of graphenes as electrocatalysts for ascorbic acid.* Electrochemistry Communications, 2010. **12**(10): p. 1307-1309.
32. Velický, M., P.S. Toth, C.R. Woods, K.S. Novoselov, and R.A.W. Dryfe, *Electrochemistry of the Basal Plane versus Edge Plane of Graphite Revisited.* The Journal of Physical Chemistry C, 2019. **123**(18): p. 11677-11685.
33. Banks, C.E., T.J. Davies, G.G. Wildgoose, and R.G. Compton, *Electrocatalysis at graphite and carbon nanotube modified electrodes: edge-plane sites and tube ends are the reactive sites.* Chemical Communications, 2005(7): p. 829-841.
34. Xu, Y., K. Sheng, C. Li, and G. Shi, *Self-Assembled Graphene Hydrogel via a One-Step Hydrothermal Process.* ACS Nano, 2010. **4**(7): p. 4324-4330.
35. Sui, Z., X. Zhang, Y. Lei, and Y. Luo, *Easy and green synthesis of reduced graphite oxide-based hydrogels.* Carbon, 2011. **49**(13): p. 4314-4321.
36. Bai, H., C. Li, X. Wang, and G. Shi, *On the Gelation of Graphene Oxide.* The Journal of Physical Chemistry C, 2011. **115**(13): p. 5545-5551.
37. Ouyang, W., J. Sun, J. Memon, C. Wang, J. Geng, and Y. Huang, *Scalable preparation of three-dimensional porous structures of reduced graphene oxide/cellulose composites and their application in supercapacitors.* Carbon, 2013. **62**: p. 501-509.
38. Worsley, M.A., P.J. Pauzauskie, T.Y. Olson, J. Biener, J.H. Satcher, Jr., and T.F. Baumann, *Synthesis of Graphene Aerogel with High Electrical Conductivity.* Journal of the American Chemical Society, 2010. **132**(40): p. 14067-14069.
39. Worsley, M.A., T.Y. Olson, J.R.I. Lee, T.M. Willey, M.H. Nielsen, S.K. Roberts, P.J. Pauzauskie, J. Biener, J.H. Satcher, Jr., and T.F. Baumann, *High Surface Area, sp2-Cross-Linked Three-Dimensional Graphene Monoliths.* The Journal of Physical Chemistry Letters, 2011. **2**(8): p. 921-925.
40. Wang, C.-C., H.-C. Chen, and S.-Y. Lu, *Manganese Oxide/Graphene Aerogel Composites as an Outstanding Supercapacitor Electrode Material.* Chemistry – A European Journal, 2014. **20**(2): p. 517-523.
41. Qin, Z., G.S. Jung, M.J. Kang, and M.J. Buehler, *The mechanics and design of a lightweight three-dimensional graphene assembly.* Science Advances, 2017. **3**(1): p. e1601536.
42. Lin, J., Z. Peng, Y. Liu, F. Ruiz-Zepeda, R. Ye, E.L.G. Samuel, M.J. Yacaman, B.I. Yakobson, and J.M. Tour, *Laser-induced porous graphene films from commercial polymers.* Nature Communications, 2014. **5**(1): p. 5714.
43. Cote, L.J., R. Cruz-Silva, and J. Huang, *Flash Reduction and Patterning of Graphite Oxide and Its Polymer Composite.* Journal of the American Chemical Society, 2009. **131**(31): p. 11027-11032.
44. Mukherjee, R., A.V. Thomas, A. Krishnamurthy, and N. Koratkar, *Photothermally Reduced Graphene as High-Power Anodes for Lithium-Ion Batteries.* ACS Nano, 2012. **6**(9): p. 7867-7878.
45. Chen, K.-S., C. Reinshagen, T.A. Van Schaik, F. Rossignoli, P. Borges, N.C. Mendonca, R. Abdi, B. Simon, D.A. Reardon, H. Wakimoto, and K. Shah,

Bifunctional cancer cell–based vaccine concomitantly drives direct tumor killing and antitumor immunity. Science Translational Medicine, 2023. **15**(677): p. eabo4778.

46. Ye, R., D.K. James, and J.M. Tour, *Laser-Induced Graphene: From Discovery to Translation.* Advanced Materials, 2019. **31**(1): p. 1803621.
47. Dong, Y., S.C. Rismiller, and J. Lin, *Molecular dynamic simulation of layered graphene clusters formation from polyimides under extreme conditions.* Carbon, 2016. **104**: p. 47-55.
48. Vashisth, A., M. Kowalik, J.C. Gerringer, C. Ashraf, A.C.T. van Duin, and M.J. Green, *ReaxFF Simulations of Laser-Induced Graphene (LIG) Formation for Multifunctional Polymer Nanocomposites.* ACS Applied Nano Materials, 2020. **3**(2): p. 1881-1890.
49. Vaughan, E., C. Larrigy, M. Burke, L. Sygellou, A.J. Quinn, C. Galiotis, and D. Iacopino, *Visible Laser Scribing Fabrication of Porous Graphitic Carbon Electrodes: Morphologies, Electrochemical Properties, and Applications as Disposable Sensor Platforms.* ACS Applied Electronic Materials, 2020. **2**(10): p. 3279-3288.
50. Bhattacharya, G., S.J. Fishlock, S. Hussain, S. Choudhury, A. Xiang, B. Kandola, A. Pritam, N. Soin, S.S. Roy, and J.A. McLaughlin, *Disposable Paper-Based Biosensors: Optimizing the Electrochemical Properties of Laser-Induced Graphene.* ACS Appl Mater Interfaces, 2022. **14**(27): p. 31109-31120.
51. Tan, K.W., B. Jung, J.G. Werner, E.R. Rhoades, M.O. Thompson, and U. Wiesner, *POROUS MATERIALS. Transient laser heating induced hierarchical porous structures from block copolymer-directed self-assembly.* Science, 2015. **349**(6243): p. 54-8.
52. Strauss, V., K. Marsh, M.D. Kowal, M. El-Kady, and R.B. Kaner, *A Simple Route to Porous Graphene from Carbon Nanodots for Supercapacitor Applications.* Advanced Materials, 2018. **30**(8): p. 1704449.
53. Bereciartua, P.J., Á. Cantín, A. Corma, J.L. Jordá, M. Palomino, F. Rey, S. Valencia, E.W. Corcoran, Jr., P. Kortunov, P.I. Ravikovitch, A. Burton, C. Yoon, Y. Wang, C. Paur, J. Guzman, A.R. Bishop, and G.L. Casty, *Control of zeolite framework flexibility and pore topology for separation of ethane and ethylene.* Science, 2017. **358**(6366): p. 1068-1071.
54. Imbrogno, A., J. Islam, C. Santillo, R. Castaldo, L. Sygellou, C. Larrigy, R. Murray, E. Vaughan, M.K. Hoque, A.J. Quinn, and D. Iacopino, *Laser-Induced Graphene Supercapacitors by Direct Laser Writing of Cork Natural Substrates.* ACS Applied Electronic Materials, 2022. **4**(4): p. 1541-1551.
55. Rathinam, K., S.P. Singh, Y. Li, R. Kasher, J.M. Tour, and C.J. Arnusch, *Polyimide derived laser-induced graphene as adsorbent for cationic and anionic dyes.* Carbon, 2017. **124**: p. 515-524.
56. Tseng, S.-F. and Y.-S. Tsai, *Laser-induced graphene via the far-infrared irradiation of polyimide films for flexible electric heater applications.* The International Journal of Advanced Manufacturing Technology, 2022. **120**(7): p. 5351-5362.
57. Silvestre, S.L., T. Pinheiro, A.C. Marques, J. Deuermeier, J. Coelho, R. Martins, L. Pereira, and E. Fortunato, *Cork derived laser-induced graphene for*

sustainable green electronics. Flexible and Printed Electronics, 2022. **7**(3): p. 035021.

58. Burke, M., C. Larrigy, E. Vaughan, G. Paterakis, L. Sygellou, A.J. Quinn, G. Herzog, C. Galiotis, and D. Iacopino, *Fabrication and Electrochemical Properties of Three-Dimensional (3D) Porous Graphitic and Graphenelike Electrodes Obtained by Low-Cost Direct Laser Writing Methods.* ACS Omega, 2020. **5**(3): p. 1540-1548.
59. Li, Y., D.X. Luong, J. Zhang, Y.R. Tarkunde, C. Kittrell, F. Sargunaraj, Y. Ji, C.J. Arnusch, and J.M. Tour, *Laser-Induced Graphene in Controlled Atmospheres: From Superhydrophilic to Superhydrophobic Surfaces.* Advanced Materials, 2017. **29**(27): p. 1700496.
60. Lamberti, A., F. Perrucci, M. Caprioli, M. Serrapede, M. Fontana, S. Bianco, S. Ferrero, and E. Tresso, *New insights on laser-induced graphene electrodes for flexible supercapacitors: tunable morphology and physical properties.* Nanotechnology, 2017. **28**(17): p. 174002.
61. Cai, J., C. Lv, and A. Watanabe, *Cost-effective fabrication of high-performance flexible all-solid-state carbon micro-supercapacitors by blue-violet laser direct writing and further surface treatment.* Journal of Materials Chemistry A, 2016. **4**(5): p. 1671-1679.
62. Murray, R., M. Burke, D. Iacopino, and A.J. Quinn, *Design of Experiments and Optimization of Laser-Induced Graphene.* ACS Omega, 2021. **6**(26): p. 16736-16743.
63. Dallinger, A., K. Keller, H. Fitzek, and F. Greco, *Stretchable and Skin-Conformable Conductors Based on Polyurethane/Laser-Induced Graphene.* ACS Applied Materials & Interfaces, 2020. **12**(17): p. 19855-19865.
64. Singh, S.P., S. Ramanan, Y. Kaufman, and C.J. Arnusch, *Laser-Induced Graphene Biofilm Inhibition: Texture Does Matter.* ACS Applied Nano Materials, 2018. **1**(4): p. 1713-1720.
65. Vivaldi, F., A. Dallinger, N. Poma, A. Bonini, D. Biagini, P. Salvo, F. Borghi, A. Tavanti, F. Greco, and F. Di Francesco, *Sweat analysis with a wearable sensing platform based on laser-induced graphene.* APL Bioengineering, 2022. **6**(3): p. 036104.
66. Stanford, M.G., C. Zhang, J.D. Fowlkes, A. Hoffman, I.N. Ivanov, P.D. Rack, and J.M. Tour, *High-Resolution Laser-Induced Graphene. Flexible Electronics beyond the Visible Limit.* ACS Applied Materials & Interfaces, 2020. **12**(9): p. 10902-10907.
67. Zhang, Z., M. Song, J. Hao, K. Wu, C. Li, and C. Hu, *Visible light laser-induced graphene from phenolic resin: A new approach for directly writing graphene-based electrochemical devices on various substrates.* Carbon, 2018. **127**: p. 287-296.
68. Carvalho, A.F., A.J.S. Fernandes, C. Leitão, J. Deuermeier, A.C. Marques, R. Martins, E. Fortunato, and F.M. Costa, *Laser-Induced Graphene Strain Sensors Produced by Ultraviolet Irradiation of Polyimide.* Advanced Functional Materials, 2018. **28**(52): p. 1805271.
69. Garland, N.T., E.S. McLamore, N.D. Cavallaro, D. Mendivelso-Perez, E.A. Smith, D. Jing, and J.C. Claussen, *Flexible Laser-Induced Graphene for Nitrogen*

Sensing in Soil. ACS Applied Materials & Interfaces, 2018. **10**(45): p. 39124-39133.

70. Wang, L., Z. Wang, A.N. Bakhtiyari, and H. Zheng *A Comparative Study of Laser-Induced Graphene by CO2 Infrared Laser and 355 nm Ultraviolet (UV) Laser*. Micromachines, 2020. **11**, DOI: 10.3390/mi11121094.
71. Santos, N.F., S.O. Pereira, A. Moreira, A.V. Girão, A.F. Carvalho, A.J.S. Fernandes, and F.M. Costa, *IR and UV Laser-Induced Graphene: Application as Dopamine Electrochemical Sensors.* Advanced Materials Technologies, 2021. **6**(6): p. 2100007.
72. Wildgoose, G.G., P. Abiman, and R.G. Compton, *Characterising chemical functionality on carbon surfaces.* Journal of Materials Chemistry, 2009. **19**(28): p. 4875-4886.
73. Yang, R.T. and C. Wong, *Mechanism of Single-Layer Graphite Oxidation: Evaluation by Electron Microscopy.* Science, 1981. **214**(4519): p. 437-438.
74. Chyan, Y., R. Ye, Y. Li, S.P. Singh, C.J. Arnusch, and J.M. Tour, *Laser-Induced Graphene by Multiple Lasing: Toward Electronics on Cloth, Paper, and Food.* ACS Nano, 2018. **12**(3): p. 2176-2183.
75. Zhu, Y., H. Cai, H. Ding, N. Pan, and X. Wang, *Fabrication of Low-Cost and Highly Sensitive Graphene-Based Pressure Sensors by Direct Laser Scribing Polydimethylsiloxane.* ACS Applied Materials & Interfaces, 2019. **11**(6): p. 6195-6200.
76. Lei, Y., A.H. Alshareef, W. Zhao, and S. Inal, *Laser-Scribed Graphene Electrodes Derived from Lignin for Biochemical Sensing.* ACS Applied Nano Materials, 2020. **3**(2): p. 1166-1174.
77. Larrigy, C., M. Burke, A. Imbrogno, E. Vaughan, C. Santillo, M. Lavorgna, L. Sygellou, G. Paterakis, C. Galiotis, D. Iacopino, and A.J. Quinn, *Porous 3D Graphene from Sustainable Materials: Laser Graphitization of Chitosan.* Advanced Materials Technologies, 2022. **n/a**(n/a): p. 2201228.
78. Ye, R., Y. Chyan, J. Zhang, Y. Li, X. Han, C. Kittrell, and J.M. Tour, *Laser-Induced Graphene Formation on Wood.* Advanced Materials, 2017. **29**(37): p. 1702211.
79. de Araujo, W.R., C.M.R. Frasson, W.A. Ameku, J.R. Silva, L. Angnes, and T.R.L.C. Paixão, *Single-Step Reagentless Laser Scribing Fabrication of Electrochemical Paper-Based Analytical Devices.* Angewandte Chemie International Edition, 2017. **56**(47): p. 15113-15117.
80. Le, T.-S.D., S. Park, J. An, P.S. Lee, and Y.-J. Kim, *Ultrafast Laser Pulses Enable One-Step Graphene Patterning on Woods and Leaves for Green Electronics.* Advanced Functional Materials, 2019. **29**(33): p. 1902771.
81. Zhang, C., Y. Xie, C. Zhang, and J. Lin, *Upgrading coal to multifunctional graphene-based materials by direct laser scribing.* Carbon, 2019. **153**: p. 585-591.
82. Kulyk, B., B.F.R. Silva, A.F. Carvalho, P. Barbosa, A.V. Girão, J. Deuermeier, A.J.S. Fernandes, F.M.L. Figueiredo, E. Fortunato, and F.M. Costa, *Laser-Induced Graphene from Paper by Ultraviolet Irradiation: Humidity and Temperature Sensors.* Advanced Materials Technologies, 2022. **7**(7): p. 2101311.

83. White, R.H., *Effect of Lignin Content and Extractives on the Higher Heating Value of Wood.* Wood and Fiber Science, 1987. **19**(4): p. 446 - 452.
84. Silva, S.P., M.A. Sabino, E.M. Fernandes, V.M. Correlo, L.F. Boesel, and R.L. Reis, *Cork: properties, capabilities and applications.* International Materials Reviews, 2005. **50**(6): p. 345-365.
85. Stanford, M.G., J.T. Li, Y. Chyan, Z. Wang, W. Wang, and J.M. Tour, *Laser-Induced Graphene Triboelectric Nanogenerators.* ACS Nano, 2019. **13**(6): p. 7166-7174.
86. Carvalho, A.F., A.J.S. Fernandes, R. Martins, E. Fortunato, and F.M. Costa, *Laser-Induced Graphene Piezoresistive Sensors Synthesized Directly on Cork Insoles for Gait Analysis.* Advanced Materials Technologies, 2020. **5**(12): p. 2000630.
87. Smith, M., L. Scudiero, J. Espinal, J.-S. McEwen, and M. Garcia-Perez, *Improving the deconvolution and interpretation of XPS spectra from chars by ab initio calculations.* Carbon, 2016. **110**: p. 155-171.
88. Yumitori, S., *Correlation of C1s chemical state intensities with the O1s intensity in the XPS analysis of anodically oxidized glass-like carbon samples.* Journal of Materials Science, 2000. **35**(1): p. 139-146.
89. Shchukarev, A. and D. Korolkov, *XPS Study of group IA carbonates.* 2004. **2**(2): p. 347-362.
90. Takahagi, T. and A. Ishitani, *XPS studies by use of the digital difference spectrum technique of functional groups on the surface of carbon fiber.* Carbon, 1984. **22**(1): p. 43-46.
91. Lesiak, B., L. Kövér, J. Tóth, J. Zemek, P. Jiricek, A. Kromka, and N. Rangam, *C sp2/sp3 hybridisations in carbon nanomaterials – XPS and (X)AES study.* Applied Surface Science, 2018. **452**: p. 223-231.
92. Kaciulis, S., A. Mezzi, S.K. Balijepalli, M. Lavorgna, and H.S. Xia, *Electron spectroscopy of rubber and resin-based composites containing 2D carbon.* Thin Solid Films, 2015. **581**: p. 80-85.
93. Jabari, E. and E. Toyserkani, *Laser heat treatment of aerosol-jet additive manufactured graphene patterns.* Journal of Physics D: Applied Physics, 2015. **48**(37): p. 375503.
94. Ferrari, A.C. and D.M. Basko, *Raman spectroscopy as a versatile tool for studying the properties of graphene.* Nature Nanotechnology, 2013. **8**(4): p. 235-246.
95. Ferrari, A.C., J.C. Meyer, V. Scardaci, C. Casiraghi, M. Lazzeri, F. Mauri, S. Piscanec, D. Jiang, K.S. Novoselov, S. Roth, and A.K. Geim, *Raman Spectrum of Graphene and Graphene Layers.* Physical Review Letters, 2006. **97**(18): p. 187401.
96. Ferrari, A.C. and J. Robertson, *Interpretation of Raman spectra of disordered and amorphous carbon.* Physical Review B, 2000. **61**(20): p. 14095-14107.
97. Kulyk, B., S.O. Pereira, A.J.S. Fernandes, E. Fortunato, F.M. Costa, and N.F. Santos, *Laser-induced graphene from paper for non-enzymatic uric acid electrochemical sensing in urine.* Carbon, 2022. **197**: p. 253-263.
98. Soares, R.R.A., R.G. Hjort, C.C. Pola, K. Parate, E.L. Reis, N.F.F. Soares, E.S. McLamore, J.C. Claussen, and C.L. Gomes, *Laser-Induced Graphene*

Electrochemical Immunosensors for Rapid and Label-Free Monitoring of Salmonella enterica in Chicken Broth. ACS Sensors, 2020. **5**(7): p. 1900-1911.
99. Silva, N.F.D., J.M.C.S. Magalhães, C. Freire, and C. Delerue-Matos, *Electrochemical biosensors for Salmonella: State of the art and challenges in food safety assessment.* Biosensors and Bioelectronics, 2018. **99**: p. 667-682.
100. Cinti, S., G. Volpe, S. Piermarini, E. Delibato, and G. Palleschi *Electrochemical Biosensors for Rapid Detection of Foodborne Salmonella: A Critical Overview*. Sensors, 2017. **17**, DOI: 10.3390/s17081910.
101. Yang, Y., Y. Song, X. Bo, J. Min, O.S. Pak, L. Zhu, M. Wang, J. Tu, A. Kogan, H. Zhang, T.K. Hsiai, Z. Li, and W. Gao, *A laser-engraved wearable sensor for sensitive detection of uric acid and tyrosine in sweat.* Nature Biotechnology, 2020. **38**(2): p. 217-224.
102. Zhang, C., J. Ping, and Y. Ying, *Evaluation of trans-resveratrol level in grape wine using laser-induced porous graphene-based electrochemical sensor.* Science of The Total Environment, 2020. **714**: p. 136687.
103. Sharma, S., S.K. Ganeshan, P.K. Pattnaik, S. Kanungo, and K.N. Chappanda, *Laser induced flexible graphene electrodes for electrochemical sensing of hydrazine.* Materials Letters, 2020. **262**: p. 127150.
104. Vivaldi, F.M., A. Dallinger, A. Bonini, N. Poma, L. Sembranti, D. Biagini, P. Salvo, F. Greco, and F. Di Francesco, *Three-Dimensional (3D) Laser-Induced Graphene: Structure, Properties, and Application to Chemical Sensing.* ACS Applied Materials & Interfaces, 2021. **13**(26): p. 30245-30260.
105. Oliveira, M.E., B.V. Lopes, J.H. Rossato, G.K. Maron, B.B. Gallo, A.B. La Rosa, R.D. Balboni, M.L. Alves, M.R. Ferreira, L. da Silva Pinto, F.R. Conceição, E. Piva, C.M. de Pereira, M.T. Escote, and N.L. Carreño *Electrochemical Biosensor Based on Laser-Induced Graphene for COVID-19 Diagnosing: Rapid and Low-Cost Detection of SARS-CoV-2 Biomarker Antibodies*. Surfaces, 2022. **5**, 187-201 DOI: 10.3390/surfaces5010012.
106. Pereira, S.O., N.F. Santos, A.F. Carvalho, A.J.S. Fernandes, and F.M. Costa *Electrochemical Response of Glucose Oxidase Adsorbed on Laser-Induced Graphene*. Nanomaterials, 2021. **11**, DOI: 10.3390/nano11081893.
107. Settu, K., P.T. Chiu, and Y.M. Huang, *Laser-Induced Graphene-Based Enzymatic Biosensor for Glucose Detection.* Polymers (Basel), 2021. **13**(16).
108. Madden, J., E. Vaughan, M. Thompson, A. O' Riordan, P. Galvin, D. Iacopino, and S. Rodrigues Teixeira, *Electrochemical sensor for enzymatic lactate detection based on laser-scribed graphitic carbon modified with platinum, chitosan and lactate oxidase.* Talanta, 2022. **246**: p. 123492.
109. Vanegas, D.C., L. Patiño, C. Mendez, D.A. Oliveira, A.M. Torres, C.L. Gomes, and E.S. McLamore *Laser Scribed Graphene Biosensor for Detection of Biogenic Amines in Food Samples Using Locally Sourced Materials*. Biosensors, 2018. **8**, DOI: 10.3390/bios8020042.
110. Mamleyev, E.R., S. Heissler, A. Nefedov, P.G. Weidler, N. Nordin, V.V. Kudryashov, K. Länge, N. MacKinnon, and S. Sharma, *Laser-induced hierarchical carbon patterns on polyimide substrates for flexible urea sensors.* npj Flexible Electronics, 2019. **3**(1): p. 2.

111. Fenzl, C., P. Nayak, T. Hirsch, O.S. Wolfbeis, H.N. Alshareef, and A.J. Baeumner, *Laser-Scribed Graphene Electrodes for Aptamer-Based Biosensing.* ACS Sensors, 2017. **2**(5): p. 616-620.
112. Beduk, T., J.I. de Oliveira Filho, A. Ait Lahcen, V. Mani, and K.N. Salama, *Inherent Surface Activation of Laser-Scribed Graphene Decorated with Au and Ag Nanoparticles: Simultaneous Electrochemical Behavior toward Uric Acid and Dopamine.* Langmuir, 2021. **37**(47): p. 13890-13902.
113. Tehrani, F. and B. Bavarian, *Facile and scalable disposable sensor based on laser engraved graphene for electrochemical detection of glucose.* Scientific Reports, 2016. **6**(1): p. 27975.
114. Hui, X., X. Xuan, J. Kim, and J.Y. Park, *A highly flexible and selective dopamine sensor based on Pt-Au nanoparticle-modified laser-induced graphene.* Electrochimica Acta, 2019. **328**: p. 135066.
115. Allen J. Bard, L.R.F., *Electrochemical Methods: Fundamentals and Applications*. 2 ed. 2001: Wiley.
116. Nicholson, R.S., *Theory and Application of Cyclic Voltammetry for Measurement of Electrode Reaction Kinetics.* Analytical Chemistry, 1965. **37**(11): p. 1351-1355.
117. Lavagnini, I., R. Antiochia, and F. Magno, *An Extended Method for the Practical Evaluation of the Standard Rate Constant from Cyclic Voltammetric Data.* Electroanalysis, 2004. **16**(6): p. 505-506.
118. Randles, J.E.B., *A cathode ray polarograph. Part II.—The current-voltage curves.* Transactions of the Faraday Society, 1948. **44**(0): p. 327-338.
119. Ševčík, A., *Oscillographic polarography with periodical triangular voltage.* Collect. Czech. Chem. Commun. , 1948. **13**: p. 349-377.
120. S. Tougaard, SURFACE ANALYSIS | X-Ray Photoelectron Spectroscopy, Editor(s): Paul Worsfold, Alan Townshend, Colin Poole, Encyclopedia of Analytical Science (Second Edition), Elsevier, 2005, Pages 446-456.
121. Liu, Z., Zhao, Z., Wang, Y., Dou, S., Yan, D., Liu, D., Xia, Z., Wang, S., *Adv. Mater.* 2017, 29, 1606207.
122. Lu, Z., Chen, G., Siahrostami, S. et al. High-efficiency oxygen reduction to hydrogen peroxide catalysed by oxidized carbon materials. Nat Catal 1, 156–162 (2018). https://doi.org/10.1038/s41929-017-0017-x
123. Daniela V. Lopes, Nuno F. Santos, Jorge P. Moura, António J.S. Fernandes, Florinda M. Costa, Andrei V. Kovalevsky, *Design of laser-induced graphene electrodes for water splitting*, International Journal of Hydrogen Energy, Volume 48, Issue 11, 2023, https://doi.org/10.1016/j.ijhydene.2022.11.005
124. Marta d'Amora et al, *Toxicity assessment of laser-induced graphene by zebrafish during development,* 2020 J. Phys. Mater. 3 034008, https://doi.org/10.1088/2515-7639/ab9522

Chapter 2: Visible Laser Scribing Fabrication of Laser-Induced Graphene Electrodes: Morphology, Electrochemical Properties and Applications as Disposable Sensor Platform

2.1 Abstract

Laser-Induced Graphene (LIG) electrodes were fabricated by direct laser writing of commercial polyimide sheets using a visible wavelength laser from a low-cost hobbyist laser engraver. Extensive electrochemical characterisation performed with $[Ru(NH_3)_6]^{3+}$, $[Fe(CN)_6]^{4-}$, $Fe^{2+/3+}$ and dopamine showed quasi-reversible electron transfer. Fast heterogeneous electron-transfer rates, higher than similar carbon-based materials and higher than other LIG electrodes produced by either visible or infrared laser irradiation, were obtained for these electrodes. The parasitic effects of working with a highly resistive electrode material were explored, and design solutions found for decoupling the electrode material from the external circuit. Thin-layer transport mechanisms occurring in parallel to the main diffusion-limited mechanism were investigated. The performance of the electrodes allowed distinction between the biomarkers ascorbic acid, dopamine and uric acid in solution by cyclic voltammetry and differential pulse voltammetry. The compatibility of these electrodes with light-weight, portable, handheld instrumentation makes such electrodes highly promising for the realisation of low-cost disposable sensing platforms for point-of-care applications.

Published: ACS Appl. Electron. Mater. 2020, 2, 10, 3279–3288. https://doi.org/10.1021/acsaelm.0c00612

2.2 Introduction

The application of graphene and graphitic materials for use as electrochemical sensors has been extensively investigated due to their remarkable physical and chemical properties. Such materials possess a wide electrochemical window and exhibit electrocatalytic activity for many redox reactions.[1,2] Moreover, they possess a rich surface chemistry, amenable to surface modification towards the realisation of selective and sensitive biosensing platforms.[3,4] The electrochemical performance of graphitic materials is highly dependent on their morphology. For example, it has been reported that the exposure of edge-planes facilitates rapid electron-transfer (ET), surface functional groups act as electrocatalytic sites, and the formation of extended 3D porous networks provide high-surface area electrodes and allows access for the electrolyte ions into the carbon material.[2, 5-8] Therefore, the ability to control the fabrication process and the resulting morphology of graphitic materials is of key importance to tune, enhance and widen their performance as electrochemical sensors and biosensors. Standard fabrication processes of graphene-like materials such as chemical vapour deposition or self-assembly of reduced graphene oxide are often expensive and time-consuming.[9, 10] Other less cumbersome methods such as screen printing or inkjet printing require the use of binders or additives that might affect the electrochemical sensitivity of the resulting electrodes whereas solution processing of graphene often results in aggregation and reduced surface area electrodes.[11-14]

Recently, direct laser writing techniques have been proposed as an alternative method for the fabrication of disposable electrochemical sensors. In the first example of this technique, a light scribe-enabled disk drive is used for the patterning of graphene oxide on PET films pre-deposited on DVD surfaces.[15,16] Electrochemical sensors were fabricated displaying a fast heterogeneous electron transfer (HET) rate

compared to commercial edge plane pyrolytic graphite (EPPG). However, the DVD scribing method required multistep chemical processing, each laser irradiation took 20 min to complete and had to be repeated 10 times to ensure reduction of graphene oxide, optimal expansion and acceptable conductivity.[15] A further simplified technique was later proposed by Tour *et al.*[17, 18] In this method simple computer-aided laser-scribing techniques were used for the fabrication of graphitic carbon structures on commercial polyimide sheets (Kapton tape). The technique was based on the use of hobbyist-laser cutters and allowed fast patterning of a variety of electrode designs onto flexible Kapton tape by a simple one-step CO_2 laser irradiation under ambient conditions. The obtained LIG structures were characterised by high porosity and excellent electrical conductivity, displayed spectral features associated to crystalline graphitic carbon structures.[18] The graphitisation of polyimide was ascribed to the high local temperature (> 2500 °C) induced by a resonance effect between the laser wavelength and the polyimide.[18,19] Nayak *et al.* investigated in detail the capability of such LIG electrodes for on-chip electrochemical sensing. They found that the morphology of the LIG, rich in defects, edge planes and surface functional groups, was particularly suitable to electrochemical sensing applications.[19] Furthermore, a detailed study was recently performed by our group whereby the morphology of LIG electrodes fabricated with a low cost visible laser cutter (405 nm wavelength) was investigated at different laser dwell time.[20] Optimum experimental conditions led to formation of structures displaying electrical and spectral characteristics comparable to LIG structures obtained with high cost CO_2 lasers. The electrodes displayed quasi-reversible behaviour, with low ΔE_P values at of 74.5 mV and 85.6 mV for $[Ru(NH_3)_6]^{3+/2+}$ and $[Fe(CN)_6]^{4-/3-}$ redox mediators, respectively, confirming fast electron transfer rates (k^0).

The biosensing performance of unmodified carbon-based electrodes is often tested by investigation of their capability to differentiate between ascorbic acid (AA), dopamine (DA), and uric acid (UA) by voltammetric methods. AA plays a key role in biological metabolism, whereas DA and UA are important biomarkers for detection of neurological disorders and kidney diseases, respectively.[21-23] AA, DA and UA coexist in the central nervous system. However, their detection by electrochemical techniques is hindered at electrodes by the overlapping of their oxidation potentials. Therefore, the simultaneous detection of AA, DA and UA in solution is an insightful experiment to determine the sensitivity of a graphene-like biosensor. LIG-based electrochemical sensors have shown high electro-catalytic activity, high sensitivity and individual component detection capabilities in AA/DA/UA mixtures.[19,24] However, such sensitivity has been achieved by enhancement of the electrocatalytic performance of the LIG electrodes by Pt deposition or conductive polymer PEDOT electrodeposition.[19,24]

In this chapter, the formation of 3D LIG electrodes obtained by direct laser writing of polyimide substrates is presented. The graphitisation of polyimide occurred under ambient conditions by irradiation with a low-cost laser cutter tool equipped with a 450 nm wavelength laser. Conductive, porous structures displaying nanocrystalline graphitic carbon spectral signatures, evidenced by Raman and X-ray photoelectron spectroscopy (XPS) data, were formed by simple one-step laser irradiation. Obtained electrodes were tested with inner-sphere and outer-sphere redox mediators and showed extremely fast HET rates, higher than other LIG structures obtained with visible and infrared laser engraving machines. The electrochemistry process was mainly diffusion limited. However, the occurrence of thin-layer voltammetric processes within the porous electrode was also investigated. The electrochemical performance of the

fabricated electrodes allowed for the simultaneous detection of AA, DA and UA mixtures, without any further modification of the electrode surface. The superior electrocatalytic properties were ascribed to the porous and extended 3D morphology of the LIG electrodes, rich in defects and edge planes.

2.3 Experimental Section

2.3.1 Materials

Polyimide films with thickness of 80 μm were purchased from Radionics and used without further treatment. DA, UA and AA were purchased from Sigma Aldrich and used without further purification. The redox systems used were the following: $[Ru(NH_3)_6]^{3+}$ (5 mM) in KCl (1 M) from $[Ru(NH_3)_6]Cl_3$ (Sigma-Aldrich); $[Fe(CN)_6]^{4-}$ (5 mM) in KCl (1 M) from $K_4Fe(CN)_6$ (Sigma-Aldrich); $Fe^{2+/3+}$ (3 mM) in $HClO_4$ (0.1 M) made from $Fe(NH_4)_2(SO_4).12H_2O$ and $HClO_4$ (0.1 M); DA (1 mM) in $HClO_4$ (0.1 M). All solutions were prepared using deionised Milli-Q water (resistivity 18.2 MΩ.cm) and deoxygenated with N_2.

2.3.2 Electrode Fabrication

LIG electrodes were fabricated by raster scanning of designed electrode structures on polyimide by a KKmoon Compact Automatic Desktop Laser Engraving Machine equipped with a laser with 3 W power and illumination wavelength of 450 nm. Polyimide tape fixed on glass microscope slides for support were irradiated at 30% laser power. Fabricated electrodes were washed with acetone and isopropanol and dried with an N_2 gun before use.

2.3.3 Characterisation

The morphology of the LIG electrodes was characterised by a cold-cathode field-emission Scanning Electron Microscope (SEM, JSM- 7500F, JEOL UK Ltd.)

operating at 5 kV acceleration voltage. White light optical microscopy images of fabricated LIG electrodes were acquired with an Axioskop II, Carl Zeiss Ltd. Microscope interfaced to a charge-coupled detector camera (Coolsnap CF, Photometrics). Surface wettability was measured by a Dataphysics OCA 20 Wetting angle system in air at ambient temperature by dropping distilled water droplets (1 mm diameter) on the LIG surfaces. The average contact angle value was acquired by measuring at six different positions of the same sample. Raman measurements were performed with a Renishaw inVia Raman system equipped with a 514 nm helium–neon laser. The laser beam was focused onto the sample through a Leica 20X objective with 0.4 N.A. Acquisition time was usually 10 s and measured power was 3 mW. X-ray photoelectron spectroscopy (XPS) measurements were carried out in an ultrahigh vacuum (UHV) chamber, with a base pressure ~$5x10^{-10}$ mbar, equipped with a SPECS LHS-10 hemispherical electron analyser and a dual anode Al/Mg x-ray gun. All XPS measurements were acquired using the un-monochromatised Mg Kα line at 1253.6 eV and an analyser pass energy of 36 eV, giving a full width at half maximum (FWHM) of 0.9 eV for the Au 4f7/2 peak. The XPS core level spectra were analysed by fitting each total spectrum to a series of individual mixed Gaussian-Lorentzian peaks following a Shirley background subtraction.

2.3.4 Electrochemical Analysis

Cyclic voltammetry (CV) and Differential Pulse Voltammetry (DPV) electrochemical measurements were performed with a CHI760 bi-potentiostat and handheld EmStatblue (PalmSens) electrochemical systems using a Pt wire as counter electrode, Ag/AgCl as reference electrode and LIG as working electrode. The parameters for the DPV measurements were: 0.004 V increment; 0.05 V amplitude; 0.1 s pulse width; 0.01 s sample width; 0.5 s pulse period. The three electrodes were assembled in a

Teflon cell with a circular area of 8 mm diameter exposed to the electrolyte. The electrochemical cell setup is shown in Figure 2.13a and b. Electrolyte solutions were purged with N_2 for 30 min prior to measurements. Heterogeneous electron transfer (HET) rate constants were determined from the anodic/cathodic peak separation using the method of Nicholson[25] by assuming transfer coefficient $\alpha = 0.5$ and using the following diffusion coefficients: $[Ru(NH3)_6]^{3+/2+}$ $D_0 = 6.5 \times 10^{-6}$ cm^2 s^{-1}; $[Fe(CN)_6]^{4-/3-}$ $D_0 = 7.63 \times 10^{-6}$ cm^2 s^{-1}, $D_R = 6.32 \times 10^{-6}$ cm^2 s^{-1}, $Fe^{2+/3+}$ $D_0 = 7.9 \times 10^{-6}$ cm^2 s^{-1}; dopamine $D_0 = 6.0 \times 10^{-6}$ cm^2 s^{-1}. In all cases except for $[Fe(CN)_6]^{4-/3-}$ it was assumed that $D_0 = D_R$.

2.4 Results and Discussion

2.4.1 Morphological Characterisation

Figure 2.1a shows a scheme of the direct laser writing method used to fabricate LIG electrodes in this work. Figure 2.1b shows a white light optical image of a representative single electrode (18 mm in length) obtained by back and forth raster scanning of the visible laser on the polyimide surface. The electrode width measured at different points along the length was homogeneous, with a mean value of 215 μm.

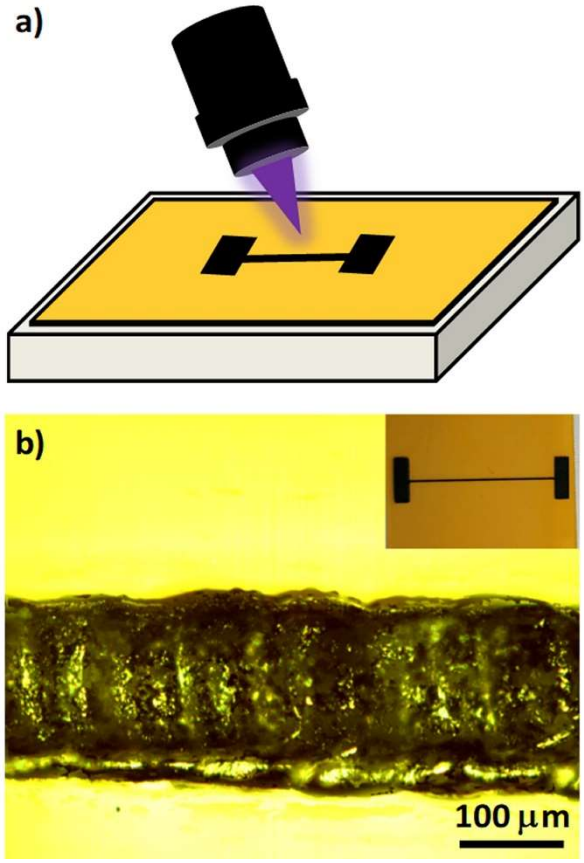


Figure 2.1 a) Schematic of the laser-scribing method used for fabrication of LIG electrodes; **b)** representative white light optical image of a fabricated LIG electrode. Inset photograph showing the entire structure of a typical LIG working electrode.

Observation of the LIG line microstructure by scanning electron microscopy (SEM) (Figure 2.2a) showed that the morphology was characterised by an irregular and flaky structure, displaying porosity and high surface area. This is similar to the morphology of graphene-like carbon electrodes obtained with other laser wavelengths.[18, 20, 26-27] An extended 3D network of overlapped graphitic carbon sheets with a high density of accessible edges constituted by kinked and wrinkled areas was also observable from the SEM images. The exposure of edges is due to the random orientation of nanocrystalline graphitic domains. The occurrence of a morphology displaying high density of 'exploded' pores has already been reported for graphitic structures written either with visible or infrared laser illumination. This phenomenon is consistent with the occurrence of a laser-assisted high-temperature, high-pressure process which causes release of the N and O of polyimide. The atoms recombine to form gas pockets

which ‘explode’.[18,20] This process contributed largely to the observed porous structure. Such a porous 3D morphology is expected to offer highly accessible electrochemical surface area. The high density of edge planes is expected to enhance electrochemical transfer behaviour, making these structures promising for electrochemical sensing applications.

The characterisation of the electrode surface by contact angle measurements (Figure 2.2b) revealed its hydrophilic nature. An average contact angle of 65.5° was measured. This is an attractive feature for electrochemical sensing purposes, as the electrode material should facilitate efficient circulation of analytes into the porous surface.

The Raman spectrum of the LIG electrode (Figure 2.2c) was characterised by three main peaks centred at 1351, 1584 and 2699 cm^{-1}, corresponding to the so called D peak (induced by bent sp^2 carbon bonds and associated with the presence of defects), G peak (corresponding to the E2g vibration mode of graphitic carbon) and 2D peak, respectively. Also, a minor peak at 2937 cm^{-1} was observed in this high wavelength part of the spectrum, corresponding to the D + D” peak. The presence of the above peaks clearly indicated the formation of a graphite-like carbon morphology. More specifically, the maximum in the *D* region could be fit with a single, sharp Lorentzian with full-width at half-maximum intensity, $FWHM(D) \sim 52$ cm^{-1}, consistent with low disorder. The other first-order peak represented a convolution of the *G* peak centred at 1575 cm^{-1} and a weaker *D*’ peak centred at 1610 cm^{-1}.[28] In early Raman studies of graphite, *D*’ peak signatures were observed in high-quality polycrystalline graphite and also by creating defects in natural graphite single crystals.[29,30] Casiraghi and co-workers established empirical relationships between the intensity ratio of the *D* and *D*’ peaks, and the nature of the defects in natural graphite or deliberately created in

exfoliated monolayer graphene.[31] They reported $I_D/I_{D'} \sim 7$ for vacancy defects, close to the $I_D/I_{D'} \sim 6$ reported in Figure 2.2c. The ratio $I_D/I_G \approx 1$ confirmed the crystalline nature of the ablated surface and was in agreement with formation of highly ordered graphite and nanocrystalline graphitic domains in a disordered carbon matrix;[20] the high I_{2D}/I_G ratio indicated a low number of graphene layers.[18, 20] Moreover, the 2D peak could be fitted by a single Lorentzian peak centred at 2699 cm^{-1}, with a FWHM of 71 cm^{-1}. This profile was consistent with 2D graphitic structures consisting of randomly stacked graphene layers along the c-axis, already reported by illumination of polyimide with high power infrared laser sources.[18]

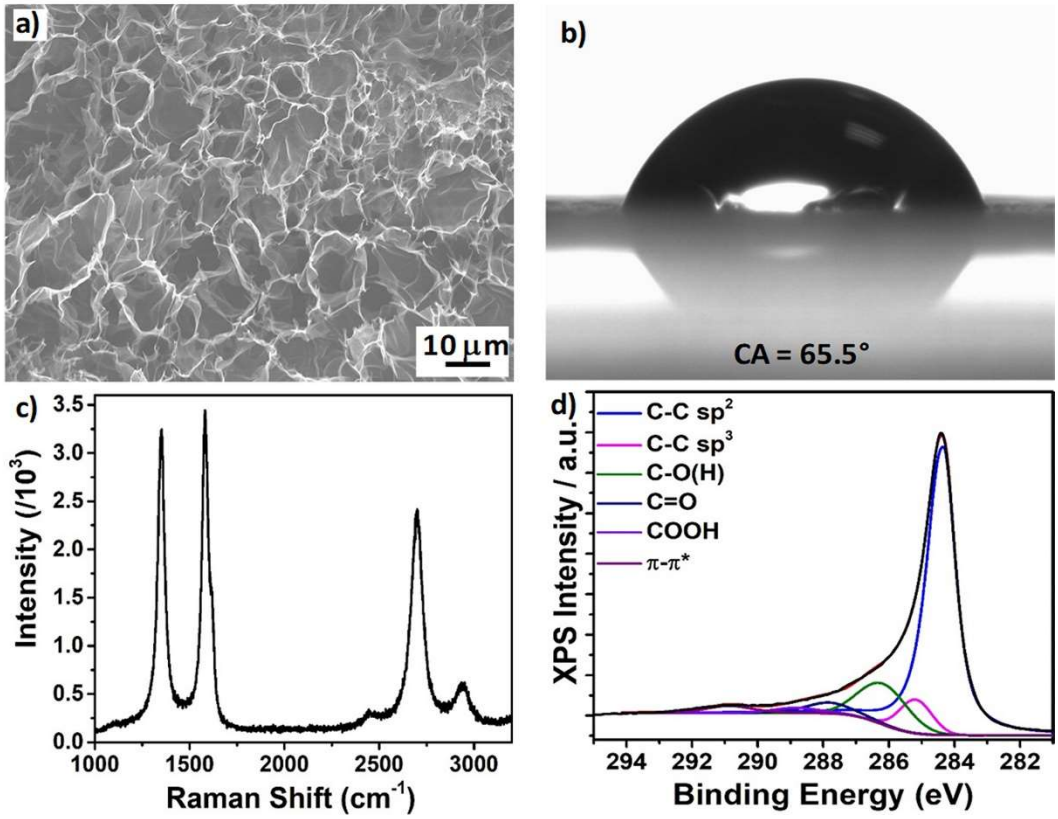


Figure 2.2 a) SEM image of a typical LIG electrode; **b)** contact angle measurement at the LIG surface; **c)** Raman spectrum and **d)** XPS spectrum of LIG electrodes.

Figure 2.2d shows the deconvoluted C1s XPS of the LIG material. The peak was analysed into six components (the main C-C sp^2, C-C sp^3, C-O(H) epoxides and hydroxides, C=O carbonyl groups, and COOH carboxyl groups and the π–π* transition

loss). Peak assignments and percentage component concentrations are shown in Table 2.1. XPS data showed that the majority of the polyimide film was converted into sp^2 carbon (71.07%), further confirming the graphene-like nature of the obtained structure. Moreover, the XPS N1s peak revealed a low percentage atomic concentration for nitrogen (2.45%; see Table 2.2, Figure 2.3), again in line with the conversion of polyimide into graphitic carbon. Also confirmed was the presence of surface carboxyl and carbonyl groups, with C-O peak more dominant than C=O peak (13.08 vs 4.03 %, respectively). It has been reported that the presence of oxygen functional groups at the surface of graphene electrodes promotes increased electrocatalytic activity for some reactions, an increase in the HET rate.[32,33]

Table 2.1 Percentage carbon component concentration derived from the XPS C1s peak deconvolution

Binding energy (eV)	Atomic percentage (%)	Assignments
284.33	71.07 ± 0.14	C-C sp^2
285.18	7.16 ± 0.12	C-C sp^3
286.18	13.08 ± 0.08	C-O(H)
287.83	4.03 ± 0.06	C=O
288.83	1.96 ± 0.06	COOH
290.88	2.70 ± 0.05	π-π^* transition

Table 2.2 % atomic concentration derived from the XPS C1s, O1s, Si2p and C1s peak areas.

Peak	Binding energy (eV)	% atomic concentration	assignments
N1s	399.76	2.45 ±0.03	Amines
O1s	532.39	9.15±0.02	C-O bonds
C1s	284.42	87.89±0.04	C-C mainly sp^2
Si2p	102.89	0.51±0.02	SiO_2

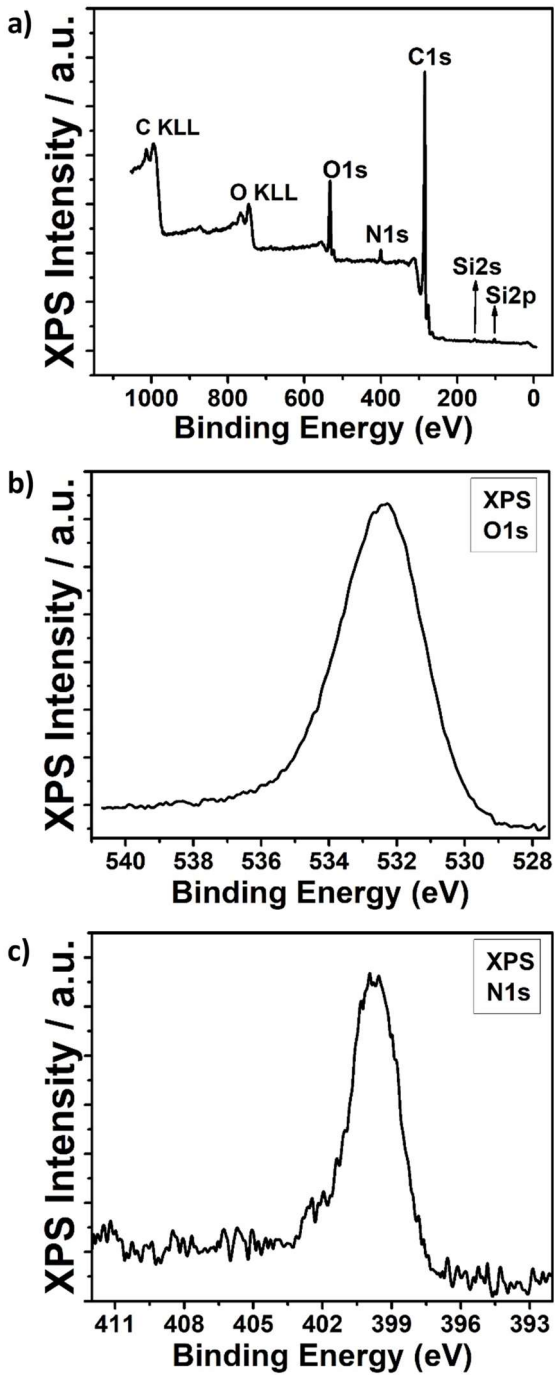


Figure 2.3 a) XPS survey scan of a representative LIG electrode; **b)** core level peak areas of O1s; **c)** core level peak areas of N1s.

2.4.2 Electrochemical Characterisation

To fully investigate the electrochemical behaviour of the fabricated LIG electrodes, the following redox systems were selected: $[Ru(NH3)_6]^{3+/2+}$, $[Fe(CN)_6]^{3-/4-}$, $Fe^{3+/2+}$ and DA. These analytes' surface reactions inform us of the material electronic properties, surface microstructure and surface chemistry. For each system, the heterogeneous

electron transfer (HET) rate constant, k^0, was calculated using the Nicholson method.[25]

Figure 2.4a shows CVs of the outer sphere redox mediator $[Ru(NH3)_6]^{3+/2+}$ recorded in the 100 -1000 mV/s scan rate range. The formal potential for this couple ($E_{1/2}$) was -0.175 V. As the $[Ru(NH3)_6]^{3+/2+}$ redox couple is insensitive to the surface microstructure, surface oxides and adsorbed monolayers on sp^2 carbon electrodes, the main factor affecting the reaction rate was the availability of electronic states (density of electronic states, DoS) near the formal potential of the redox system.[1,34-35] The average ΔE_P calculated at 100 mV/s scan rate over three electrodes was found 57 mV (σ = 4.2 mV), below the theoretical minimum peak separation of 59 mV for a one-electron reversible reaction. Using the Nicholson method, a value of k^0 of 6.9×10^{-2} cm/s was determined for this redox system.[25] This k^0 value was 5 times higher than the value previously obtained by our group for LIG electrodes obtained with a 405 nm laser system.[20] The extremely low peak separation and rapid electron transfer rate suggested a high DoS for the system near the formal potential of $[Ru(NH3)_6]^{3+/2+}$. It should be pointed out that the ΔE_P value found for this system was 1.3 and 1.5 times lower than the value previously published for porous LIG electrodes obtained with 405 nm and 10.6 μm irradiation wavelengths.[19,20] Further exploration of the nature of this low value for the peak-to-peak separation will be discussed later. The electrochemical behaviour measured in the 100-1000 mV/s scan rate range showed quasi-reversible behaviour, evidenced by the monotonic increase/decrease of the oxidation/reduction peak current with the square root of scan rate (inset of Figure 2.4a) and indicating a semi-infinite linear diffusion reaction process (R^2 for oxidation and reduction currents 0.996 and 0.995, respectively).

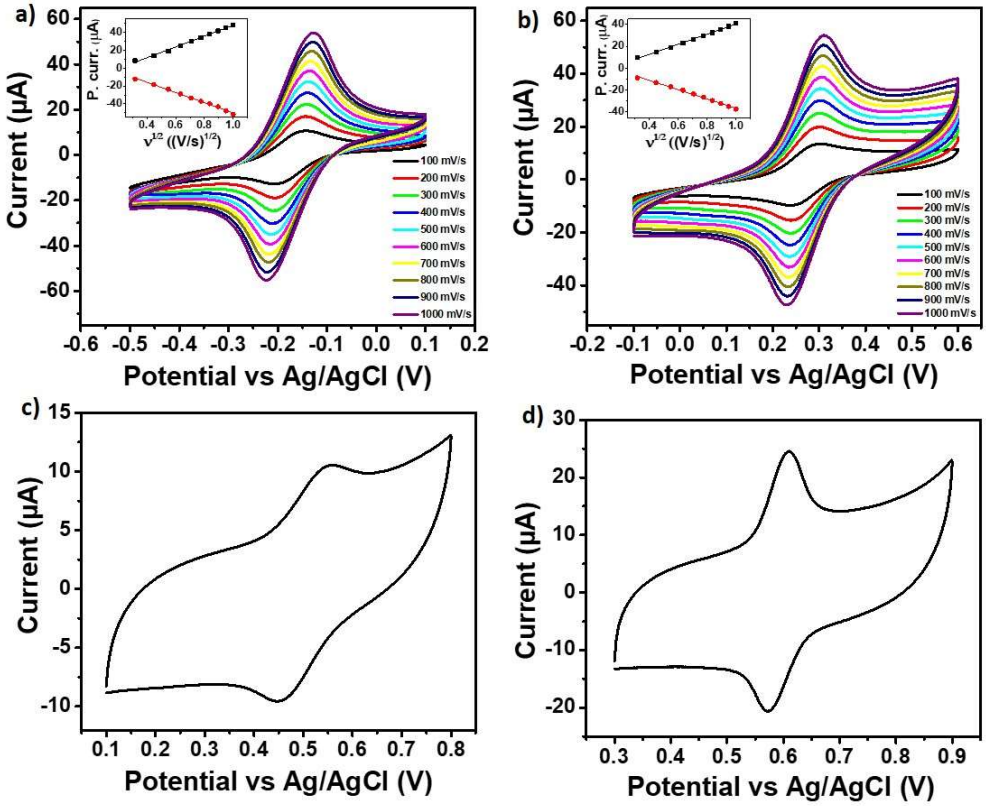


Figure 2.4 Cyclic voltammograms for four redox systems at LIG electrodes: **a)** 5 mM $[Ru(NH3)_6]^{3+/2+}$ in 1 M KCl. Inset: peak oxidation and reduction values *vs* square root of potential scan rate; **b)** 5 mM $[Fe(CN)_6]^{3-/4-}$ in 1 M KCl. Inset: peak oxidation and reduction values *vs* square root of potential scan rate; **c)** 1 mM $Fe^{2+/3+}$ in 0.1 M $HClO_4$; **d)** 1 mM DA in 0.1 M $HClO_4$.

Further characterisation was performed with the inner sphere $[Fe(CN)_6]^{3-/4-}$, a redox couple sensitive to the electrode microstructure and for which the HET process is known to depend strongly on the density of exposed edge plane sites.[1] Figure 2.4b shows that electrodes display rapid electron transfer rates for $[Fe(CN)_6]^{3-/4-}$. The formal potential for this couple was 0.271 V. The average ΔE_P calculated over three samples at 100 mV/s scan rate was 61 mV (σ = 5.1 mV). The value of k^0 was calculated as 1.3 × 10^{-1} cm/s, as determined by the Nicholson method.[25] This k^0 value was 10 times higher than the value previously obtained by our group for LIG electrodes obtained with 405 nm laser systems. In comparison with this previous work, by examining the SEMs of both we see that the morphology of the two LIGs differs vastly: the same folding and wrinkling we have shown with this 450 nm LIG was not evident with the

405 nm LIG; a greater exposure of graphitic edge defects is hypothesised as the explanation for the enhanced electrochemical kinetic rates.[20] For this system, the effect of scan rate on the peak current was also determined. A monotonic increase/decrease of the oxidation/reduction peak current with square root of scan rate (inset of Figure 2.4b) was observed. This indicates a diffusion controlled reaction, in line with the Randles-Ševčík equation. The data recorded with this system indicate that the electrodes possess a surface structure capable of supporting rapid electron transfer. The data correlates well with the morphology displayed in the SEM images (Figure 2.2a) suggesting a high density of exposed edge defects at the electrode surface.

Figure 2.4c shows a CV recorded for $Fe^{3+/2+}$, another inner sphere redox system sensitive to surface carbon-oxygen functionalities, especially surface carbonyl groups, on sp^2 carbon electrodes.[1] ΔE_p for $Fe^{2+/3+}$ was 113 mV at a scan rate of 100 mV/s – giving a k^0 value of 6.5×10^{-3} cm/s. This value is of the same order of magnitude as values reported for reduced graphene sheet films, and fast in comparison with glassy carbon electrodes.[36] The rapid electron-transfer in the $Fe^{2+/3+}$ reaction, correlated to the presence of carboxyl and carbonyl surface groups, is consistent with the findings of the XPS data (Figure 2.2d). Finally, Figure 2.4d shows CV of DA, a redox system which requires adsorption and is sensitive to the presence of oxides.[1, 36] At a scan rate of 100 mV/s the ΔE_p was 37 mV, much lower than values previously reported for glassy carbon electrodes and lower than the 60 mV value reported for reduced graphene sheets.[36]

In order to evaluate contribution of the high porosity/high surface area to the excellent electrochemical results, a comparison between the electrode geometric and electrochemical areas was carried out. An initial comparison between the estimated geometric area of the electrode (1.72 mm^2) and the electrochemically active area (1.5

± 0.3 mm^2; calculated by the Randles-Ševčík equation) suggested no contribution arising from the porous morphology of the electrode.[37] Considering the SEM imaging, it is expected that the active area would be larger than the geometric area, and certainly not less. Further investigation of the electrochemical behaviour of the electrodes showed that the surface area exposed to the analyte solution was not entirely electrochemically active. The cause of this was the electrical properties of the sensor. A large resistance (2.1 kΩ ± 0.08) was measured across these electrodes, from end-to-end. This caused a potential drop across the electrode upon current passage, by Ohm's law. This means that the entire electrode was not equipotential, and that much of the area furthest away from the potentiostat connection did not reach a potential allowing it to contribute to the electrochemical reaction. This is similar to behaviour previously reported in the use of Au nanowire electrodes.[38] Further investigation showed that this potential-drop became insignificant at electrode lengths of between ¼ and ½ of the 8 mm electrochemical cell diameter. For such electrodes, as shown in Figure 2.5, the ratio between calculated geometric area and electrochemically active area raised to between 1.23 and 1.63, compared to 0.87 for the full sized electrode. This data confirmed that the expected contribution of the increased surface area arising from the porous morphology did have significant effect for shortened electrodes, where the entire electrode surface was electrochemically active.

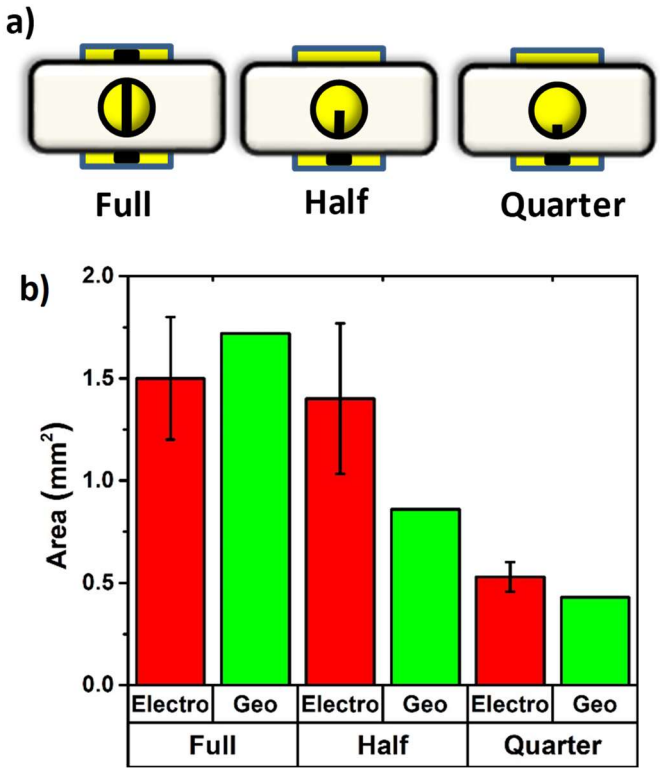


Figure 2.5 a) Schematic of the Full, Half, and Quarter electrodes; **b)** Comparison between the geometric area and electrochemically active area of electrodes calculated at 100 mV/s.

Further investigation of the effect of the potential-drop across the electrode was conducted by connecting the potentiostat to both ends of the electrode. The electrode was split in the middle, thus shortening the length and reducing the area with respect to the 'full' electrode we have been using (see schematic inset of Figure 2.6a). Conductive silver paint was used to create a contact for the potentiostat at a single point for both electrode halves, making both sides of the electrode equipotential (resistance of the Ag paint track < 5 Ω). Despite the smaller area, the CV performed in $[Fe(CN)_6]^{3-/4-}$ resulted in a much higher peak current for the split electrode – 2.7 times that of the full electrode as – seen clearly in Figure 2.6a. Given the problems posed by the large electrical resistance of the single line (~200 µm thick) electrode, a wider electrode (3 mm) was produced with considerably lower resistance across its 18 mm length (96 Ω ± 4). An experiment similar to that with the full and split electrode was conducted to investigate if the lower resistance of such a design would render the

effect of the potential-drop negligible. Conductive silver paint was used to create a single contact for both ends of the electrode ("short-circuit" design). The electrochemical responses of this setup were compared with those of the single connection and are shown in Figure 2.6b. The short-circuit setup did not result in an enhanced current response. The same area was active in both cases. Hence, the smaller resistance allowed the entire electrode to contribute to the electrochemical reaction.

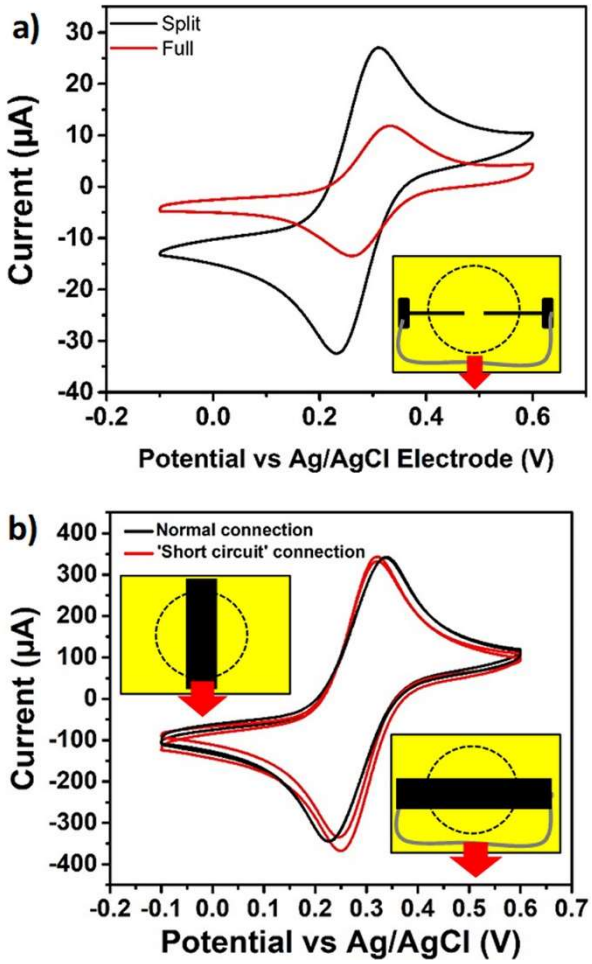


Figure 2.6 a) Cyclic voltammograms of Split electrode (red curve) and Full electrode (black curve) for 1 mM $[Fe(CN)_6]^{3-/4-}$ in 1 M KCl redox system, scan rate 100 mV/s. Inset: LIG of the Split electrode connection; **b)** cyclic voltammograms of 3 mm wide LIG electrodes for 1 mM $[Fe(CN)_6]^{3-/4-}$ in 1 M KCl redox system, scan rate 100 mV/s. Normal connection (black curves) and short circuit connection (red curves) at LIG electrodes: Inset: graphic description of the two connections. Red arrows indicate potentiostat connections, broken circle indicates o-ring position in electrochemical cell.

The difference that should be noted is in the ΔE_P values of the two setups: for the "normal mode", the values were 111 mV and 113 mV for two experiments, whereas

for the short-circuit mode the values were 69 mV and 75 mV. While in the normal setup the entire electrode became active and contributed to the reaction, a small potential gradient across the electrode as the potential was scanned by the potentiostat led to a lag in the response, and a larger peak separation. Figure 2.7 displays the behaviour of both setups with increasing scan rate. While the short-circuit mode maintained perfect linearity between peak current and square root of scan rate (Figure 2.7b inset) the normal setup lost linearity at scan rates higher than 0.5 V/s, as the potential gradient across the electrode became a significant factor (Figure 2.7a inset).

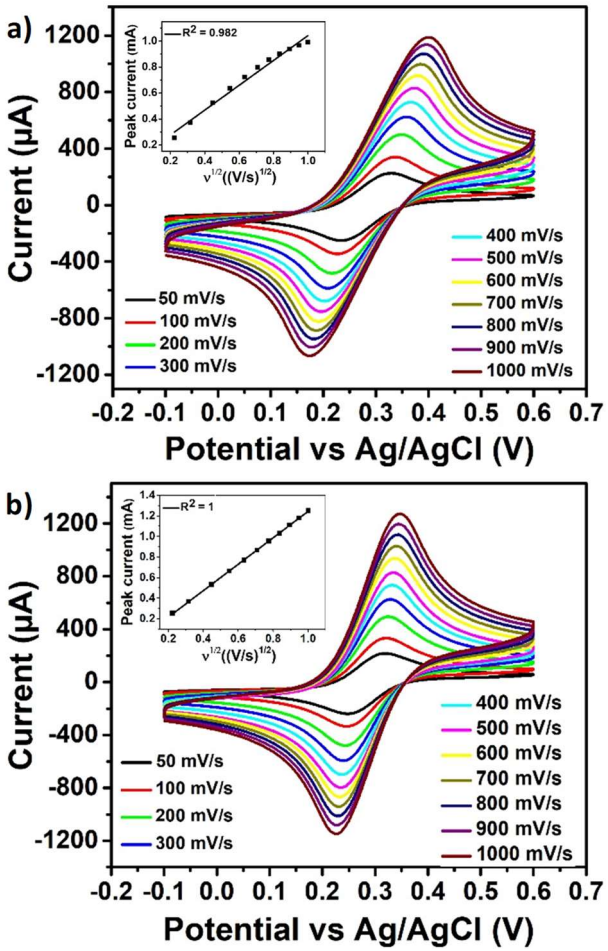


Figure 2.7 Cyclic voltammograms of 1 mM $[Fe(CN)_6]^{3-/4-}$ in 1 M KCl for **a)** 3 mm wide electrode normal connection and **b)** 3 mm wide short-circuit connection. Insets: peak oxidation values vs square root of potential scan rate.

The results of the ET reactions of the above-mentioned redox couples investigated by CV are summarised in Table 2.3. The electrochemical performance of this LIG

electrodes against other carbon-based electrodes reported in literature is shown in Table 2.4. In each case, the electron-transfer kinetics were favourable in comparison with glassy carbon electrode values in literature, and comparable with values obtained at graphene electrodes fabricated via multi-step processes.[1, 36, 39] The fast HET kinetics were ascribed to the abundance of edge-planes and surface defects of the LIG electrodes, as revealed by SEM images and in the Raman spectra of the electrodes.

Table 2.3 Summary of electrode performance. k^o values were calculated using v ranging from 100 mV/s to 1000 mV/s for $[Ru(NH3)_6]^{3+/2+}$ and $[Fe(CN)_6]^{3-/4}$; values for $Fe^{2+/3+}$ and DA were calculated at 100 mV/s. ΔE_P reported for v = 100 mV/s.

Analyte	ΔE_p (mV)	k^0 (cm s^{-1})
$[Fe(CN)_6]^{3-/4-}$	60.7	1.26×10^{-1}
$[Ru(NH_3)_6]^{2+/3+}$	57.3	6.93×10^{-2}
$Fe^{2+/3+}$	113	6.53×10^{-3}
Dopamine	37	2.26×10^{-2}

Table 2.4 Summary of electrochemical performance for carbon-based electrodes obtained with $[Ru(NH3)_6]^{3+/2+}$ and $[Fe(CN)_6]^{3-/4-}$ mediators.

Material	ΔE_p (mV) $[Fe(CN)_6]^{3-/4-}$	ΔE_p (mV) $[Ru(NH_3)_6]^{2+/3+}$	k^0 (cm s^{-1}) $[Fe(CN)_6]^{3-/4-}$	k^0 (cm s^{-1}) $[Ru(NH_3)_6]^{2+/3+}$	Ref.
405 nm LIG	85.6	74.5	1.3×10^{-2}	1.46×10^{-2}	[20]
Glassy Carbon	68	64	2.9×10^{-2}	5.5×10^{-2}	[32]
Reduced Graphene Films	65	61	4.9×10^{-2}	1.8×10^{-1}	[32]
HOPG basal			$< 10^{-7}$	1.4×10^{-3}	[1]
HOPG edge			$6 \times 10^{-2} - 1 \times 10^{-1}$	8.8×10^{-3}	[1]
CO_2 LIG	85.6	95	$*1.15 \times 10^{-1}$	$*8.7 \times 10^{-2}$	[19]
Pt/LIG	70.8	74.5	$*2.8 \times 10^{-1}$	$*2.3 \times 10^{-1}$	[19]
450 nm LIG	60.7	57.3	1.26×10^{-1}	6.93×10^{-2}	This work

*Suspected erroneously large k^0 calculation.

As reported above, LIG electrodes exhibited low peak to peak separations (<59 mV/n) for CV scans of standard redox couples $[Ru(NH_3)_6]^{2+/3+}$ and $[Fe(CN)_6]^{3-/4}$. Although it is common practice to define the electron transfer mechanism as diffusion limited process (following the semi-infinite planar diffusion model) and to attribute small voltammetric peak separations to enhanced electron transfer rates of the

electrode material, other contributing factors could be at play in highly porous 3D systems. For example, it was reported in glassy carbon-modified single wall carbon nanotube (GC/SWCNT) electrodes that the contribution from thin layer mass transport within the porous 3D networks was significant.[40] In such systems, the analyte penetrated the porous structures, becoming trapped within the electrode pores. In such a scenario, the resultant CVs were a combination of the expected semi-infinite planar diffusion model from the surface contribution, and a thin layer contribution. Lower peak separations were observed than would have been from the surface alone. Care must be taken with such systems to not attribute these lower separations to kinetics alone, without accounting for the thin-layer contribution.

In order to examine the extent of such a contribution in our system, an electrode was cycled in supporting electrolyte (KCl 1 M, 100 mV/s). After immersion in $[Fe(CN)_6]^{3-/4}$ (5 mM, 5 min, in 1 M KCl) followed by thorough rinsing cycles in deionised water, the electrode was cycled again in supporting electrolyte. Data shown in Figure 2.8 demonstrate that the electrode was modified by simple immersion in the $[Fe(CN)_6]^{3-/4}$ solution. An oxidation/reduction peak formed as result of $[Fe(CN)_6]^{3-/4}$ being adsorbed on the electrode surface or trapped with the electrode porous network. We speculate that pockets of analyte solutions became trapped in the porous electrode structure, a process similar to that reported by Streeter *et al.* for GC electrodes surface modified with single-walled carbon nanotubes (SWCNTs).[40] However, as shown in the insets of Figure 2.4a and b, i_P for $[Ru(NH_3)_6]$ and $[Fe(CN)_6]$ was found to be proportional to the square root of the scan rate, as predicted by the Randles-Ševčík equation for reversible reactions at electrodes governed by semi-infinite linear diffusion. Instead, for processes governed by thin layer diffusional processes, i_P would be proportional to the scan rate.[41] Evidently for the LIG electrodes in this study there

is a contribution from immobilised solution within the porous electrode, but not significant enough to perturb the response from being interpreted as semi-linear diffusion. Hence, the lower peak separations can indeed be attributed to the excellent electron-transfer properties of the LIG electrode.

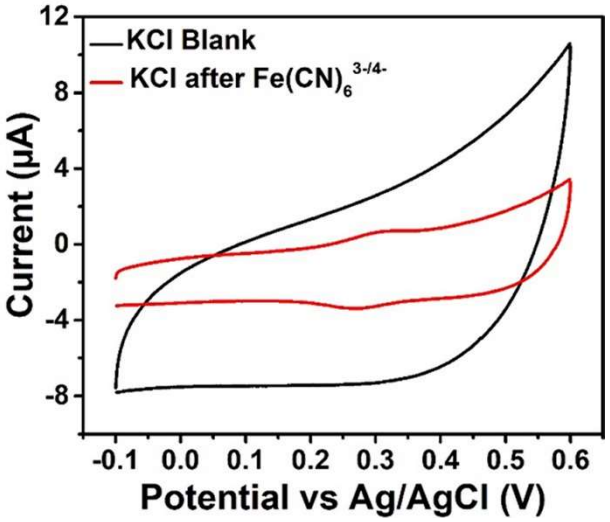


Figure 2.8 CV of supporting electrolyte KCl 0.1 M in PBS 0.1 M (pH = 7.4) (back curve) and CV of KCl obtained after cycling the electrode in $Fe(CN)_6^{3-/4-}$ 0.1 M (red curve). Scan rate 100 mV/s.

2.4.3 Biosensor Performance

Given the excellent electron transfer properties of the LIG electrode, its performance as biosensor was investigated. In order to evaluate the sensitivity and selectivity of the LIG electrodes it was decided to study a DA, UA and AA system. As well as the specific importance of each specie as biomarker for human health monitoring, DA, UA and AA coexist in the central nervous system and their electrochemical oxidation peaks overlap in conventional solid electrodes, making difficult to perform individual sensing. Therefore, the purpose of the investigation was to demonstrate the importance of the rapid electrode kinetics of these LIG electrodes, by their ability to differentiate DA, UA and AA species by providing enhanced separation of oxidation potentials. Individual DA (1 mM), UA (1 mM) and AA (1 mM) in 0.1 M PBS CVs are shown in Figure 2.9.

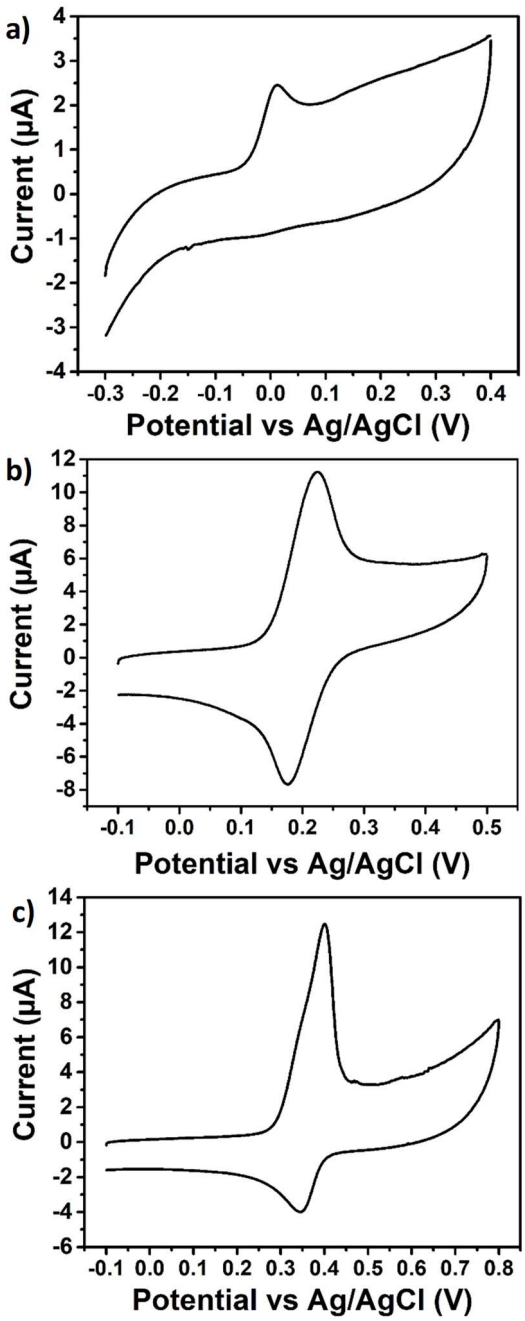


Figure 2.9 Individual CV scans for **a)** ascorbic acid, **b)** dopamine and **c)** uric acid 1 mM in 0.1 M PBS (pH = 7.4). Scan rate 100 mV/s.

Figure 2.10a shows a CV scan of a solution containing a mixture of DA, UA and AA (all 1 mM) in 0.1 M PBS recorded at 100 mV/s. The curve shows well defined and well separated oxidation peaks at 0.044 V, 0.218 V, and 0.389 V corresponding to the oxidation of AA, DA and UA, respectively. The resulting oxidation peak separations were: $\Delta E_{AA\text{-}DA}$ = 0.174 V, $\Delta E_{DA\text{-}UA}$ = 0.171 V and $\Delta E_{AA\text{-}UA}$ = 0.345 V; showcasing

LIG's capability for selective determinations of individual species. Figure 2.10b shows a DPV scan for the same system, displaying excellent resolution of the three peaks for AA, DA and UA. The peak separation values are as follows: $\Delta E_{AA-DA} = 0.184$ V, $\Delta E_{DA-UA} = 0.160$ V and $\Delta E_{AA-UA} = 0.344$ V; allowing simple identification of concomitant species. These values are lower than those reported in literature for graphene-based electrodes and comparable to values reported for LIG electrodes with enhanced catalytic activity obtained by post-fabrication Pt or PEDOT electrodeposition steps (see Table 2.5 for further details).[19, 24] The LIG electrode displayed high selectivity due to a combination of enhanced electron transfer associated to the exposure of edge defects through its porous morphology, the enhanced catalytic activity due to the presence of surface functional groups, and the large available surface area providing reaction sites for biomolecules. The exact nature of the electrocatalytic effect of surface groups on carbon electrodes for the dopamine reaction is not entirely clear: studies have suggested that oxide moieties catalyse dopamine charge transfer, while at the same time inhibiting adsorption of dopamine.[43, 44] These results are encouraging for the potential of LIG fabricated with low-cost, low-powered laser systems to be used as a cheap and easily-fabricated biosensing material.

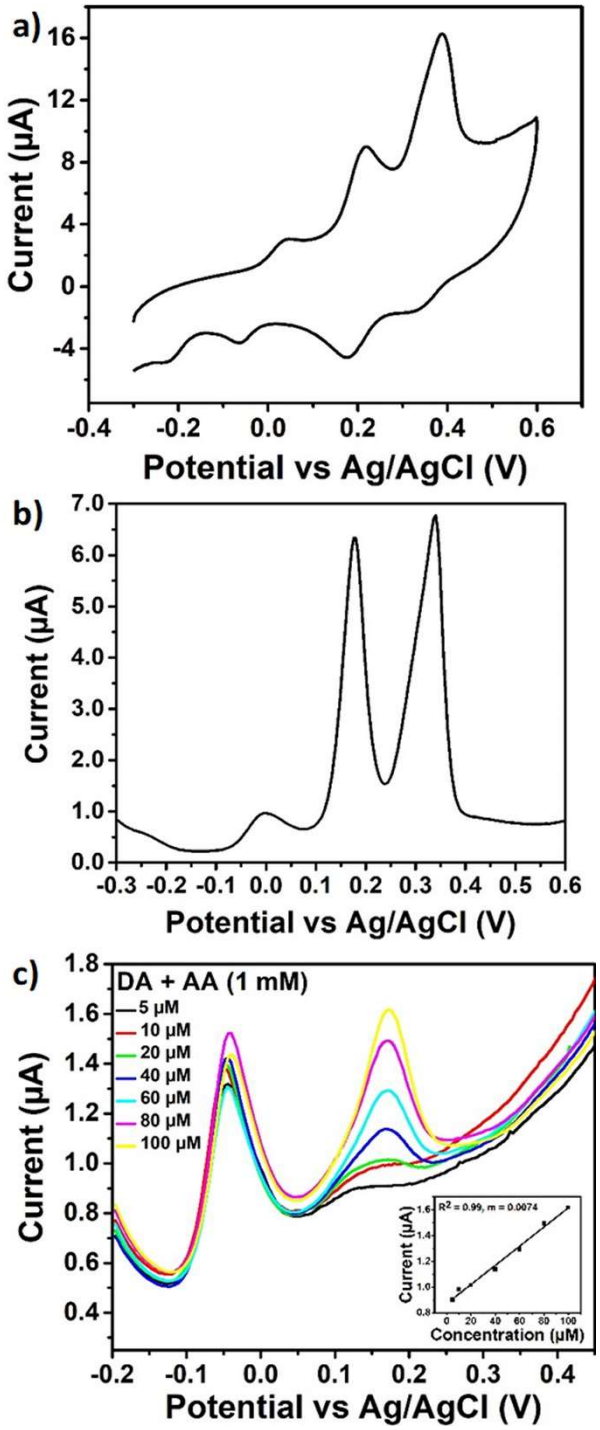


Figure 2.10 a) CV (scan rate 100 mV/s) and **b)** DPV curves for AA, DA and UA 1 mM in 0.1 M PBS (pH = 7.4); **c)** DPV response of different concentrations of DA in presence of AA 1 mM in PBS 0.1 M (pH = 7.4). Inset: concentration vs current linear response for DA calculated from DPV curves shown.

Figure 2.10c shows the DPV response of varying concentrations of DA (5 μM – 100 μM) in the presence of a constant concentration of AA (1 mM). The oxidation peak current at 0.172 V associated to DA increased as its concentration was increased from 5 μM to 100 μM. In contrast the oxidation peak current at -0.44 V associated to

AA remained almost constant, showing again the electrode good speciation ability between potentially interfering species. As shown in the inset of Figure 2.10c, the current response to DA concentration was linear in the range of 5-100 μM, with a sensitivity of 7.4 x 10^{-3} A/M. The sensitivity parameter was calculated from the slope of the calibration plot. A comparison of the presented LIG electrode with similar graphitic carbon structures is reported in Table 2.5. However, the limit of detection for DA concentration was equal to only 300 μM. This unexpectedly high value was attributed to a high standard deviation, caused by a large variation in active area due to the potential profile across the resistive material. However, with the previously discussed low resistance 3 mm wide electrodes a substantial improvement in the biosensor performance was observed, resulting in calculated LODs of 5.5 μM for dopamine (see Figure 2.11).

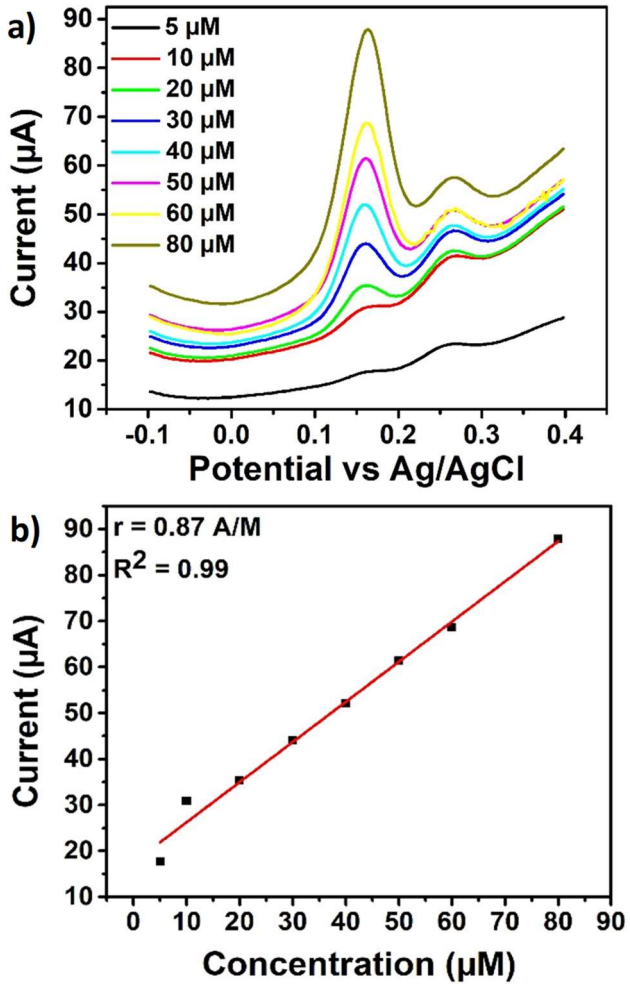


Figure 2.11 a) Differential pulse voltammetry (DPV) curves for DA in 0.1 M PBS (pH = 7.4) at scan rate 100 mV/s; **b)** Concentration vs current linear response for DA calculated from DPV curves shown in a.

Table 2.5 Comparison of experimental data with literature values of peak separation reported for AA, DA and UR systems by CV and DPV

Material	Method	ΔE_{AA-DA}	ΔE_{AA-DA}	ΔE_{AA-DA}	Ref.
LIG	DPV	174	160	334	This work
LIG	CV	174	170	344	This work
LIG-modified GC	DPV	208	124	332	[42]
PEDOT-LIG	DPV	216	120	336	[24]
PEDOT-LIG	CV	250	150	400	[24]
R-GO-modified GC	DPV	207	129	336	[39]
LIG	DPV	234	134	368	[19]
Pt-LIG	DPV	236	143	379	[19]

The performance of these electrode was comparable to that of LIG electrodes fabricated with high power CO_2 lasers and with surfaces modified and enhanced by post-fabrication treatments such as Pt or PEDOT deposition. In contrast, the presented electrodes were fabricated with low cost/low power visible hobbyist lasers and were used without any post-fabrication enhancement step. Furthermore, comparison of performance with previously reported electrodes fabricated by 405 nm laser irradiation[20] showed superior sensitivity for DA and superior speciation capabilities for DA, AA and UA mixtures (see Figure 2.12).

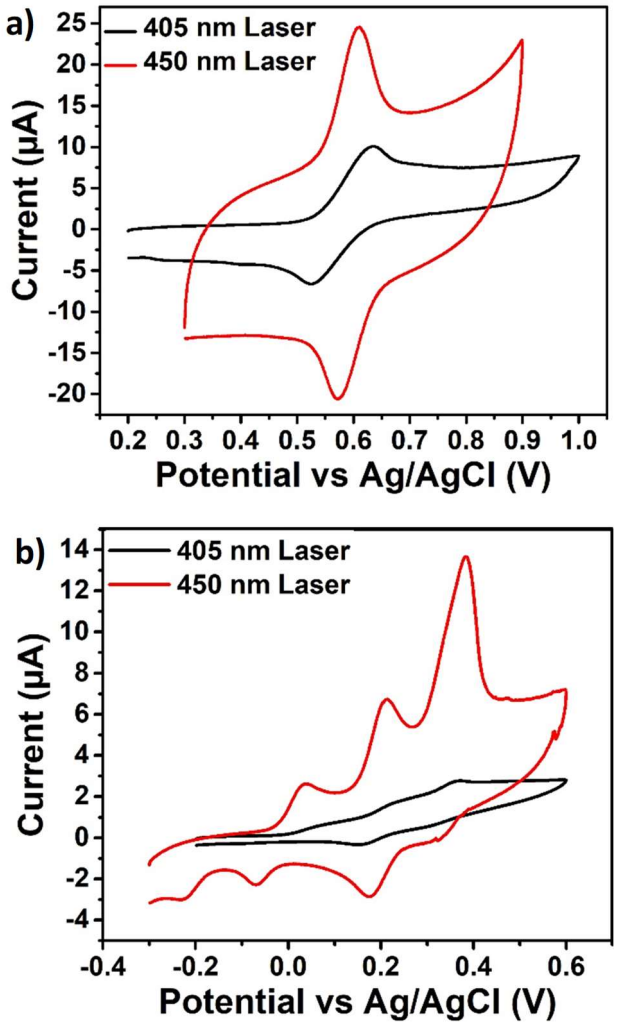


Figure 2.12 a) Cyclic voltammograms of 1 mM DA in 0.1 M $HClO_4$.at scan rate 100 mV/s recorded using a LIG working electrodes obtained by 405 nm laser irradiation (black line) and 450 nm laser irradiation (red line); **b)** Cyclic voltammograms of 1 mM DA, AA, UA in 0.1 M PBS at scan rate 100 mV/s obtained with a 405 nm laser LIG electrode (black line) and a 450 nm laser LIG working electrode (red line).

The developed electrochemical setup was also compatible with light weight portable instrumentation. This setup is shown in Figure 2.13. Also shown is a CV of $[Fe(CN)]^{3-/4-}$ recorded with a handheld potentiostat. The peak separation and peak current is in agreement with the results obtained using the bench bi-potentiostat. Therefore, these results are very encouraging for the development of low cost routes for fabrication of disposable and sensitive biosensors.

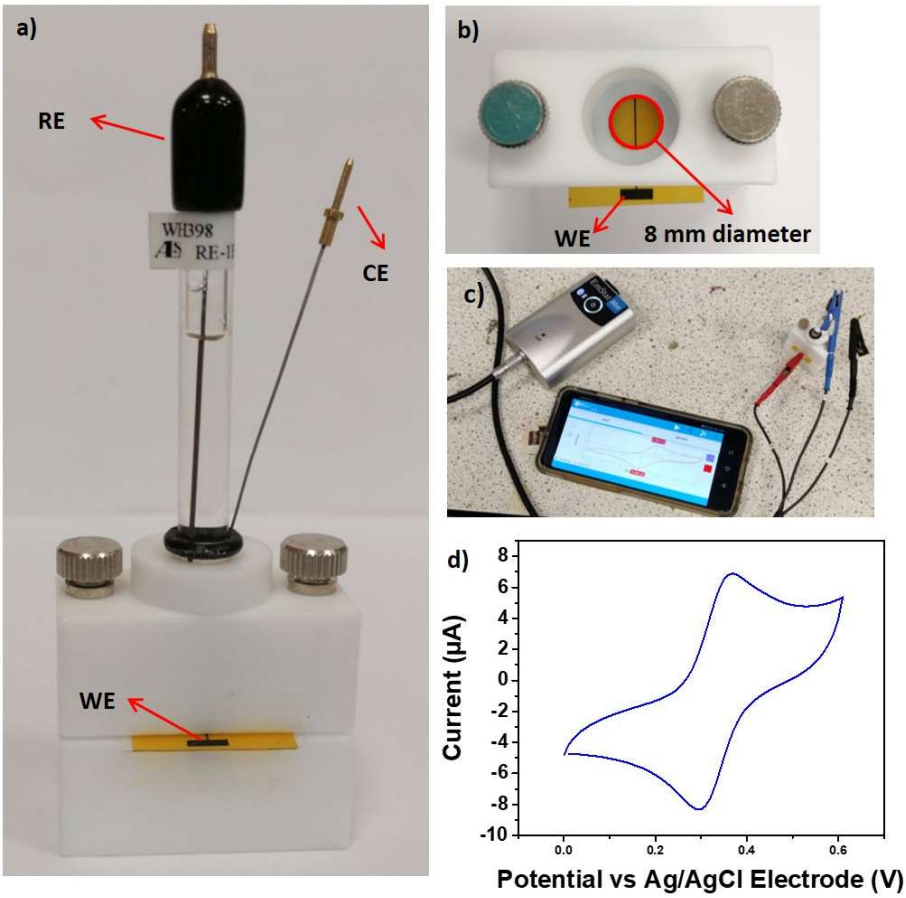


Figure 2.13 a) Photograph of a typical electrochemical cell comprising LIG working electrodes (WE), Pt counter electrode (CE) and Ag/AgCl reference electrode (RE); **b)** Top view photograph of the LIG WE in the teflon cell; **c)** photograph of handheld potentiostat controlled by Bluetooth connection to smartphone application for *in situ* measurements; **d)** CV scan of $[Fe(CN)_6]^{3-/4-}$ in 1 M KCl recorded using handheld potentiostat shown in c.

2.5 Conclusions

LIG electrodes were readily fabricated by a direct laser writing method by using a low-cost hobbyist laser with 450 nm laser illumination. The electrodes displayed a highly porous and 3D structure, rich in defects and edge planes which was conducive to

excellent electrochemical sensing capabilities. The HET kinetics were characterised by the $[Ru(NH3)_6]^{3+/2+}$, $[Fe(CN)_6]^{3-/4-}$, $Fe^{2+/3+}$ and DA, revealing rapid, diffusion-controlled quasi-reversible electron transfer at the electrode surface. Peak separation values achieving the reversible limit were achieved at the high scan rate of 100 mV/s. Overall, better electrochemical performance was obtained compared to other LIG electrodes fabricated either by visible or infrared laser illumination. The superior electrode performance was ascribed to the formation of highly porous and 3D structures, characterised by high surface area, large networks and abundance of defect and edge planes and facilitating analyte adsorption and circulation. The effect of porosity on the ET kinetics was assessed by comparison between geometric area and electrochemically active area. Important discoveries relating the electrode design of a resistive LIG system were made, whereby the destructive contribution of a potential gradient across the electrode surface can be minimised. The contribution of other mechanisms such thin layer diffusion mechanisms was taken in consideration in order to clarify the origin of the enhanced electron-transfer kinetics observed in these electrodes. However, such a contribution was considered to be too small to perturb the dominant diffusion limited process. Finally, the fabricated LIG electrodes showed excellent biosensing performance and were able to perform electrochemical detection of AA, DA and UA in solution without further electrode modification by both CV and DPV methods. This in-depth study shows that direct laser writing techniques constitute a viable route for the fabrication of low-cost disposable electrochemical biosensing platforms for in-field, point-of-care and lab-on-a-chip applications, as well as in other integrated bioelectronics applications.

2.6 References

1. McCreery, R. L. Advanced Carbon Electrode Materials for Molecular Electrochemistry. *Chem. Rev.* **2008**, 108, 2646-2687.
2. Wang, J. *Analytical Electrochemistry*, 2nd *ed.* Wiley, New York, NJ, **2000**
3. Szuneritis, S.; Boukherroub, R. Graphene-based Biosensors, *Interface Focus*, **2018,** 8, 20160132.
4. Shao, Y; Wang, J.; Wu, J.; Aksay, I. A.; Lin, Y. Graphene Based Electrochemical Sensors and Biosensors: A review. *Electroanalysis*, **2010,** 22 (10), 1027-1036.
5. Unwin, P. R.; Güell, A. G.; Zhang, G. Nanoscale Electrochemistry of sp2 Carbon Materials: from Graphite and Graphene to Carbon Nanotubes. *Acc. Chem. Res*. **2016**, 49, 2041−2048.
6. Chen, D.; Feng, H.; Li, J. Graphene Oxide: Preparation, Functionalization, and Electrochemical Applications. *Chem. Rev*. **2012**, 112, 6027−6053.
7. Wu, Z.-S.; Sun, Y.; Tan, Y.-Z.; Yang, S.; Feng, X.; Müllen, K. Three-Dimensional Graphene-Based Macro- and Mesoporous Frameworks for High-Performance Electrochemical Capacitive Energy Storage. *J. Am. Chem. Soc.* **2012**, 134, 19532−19535.
8. Wu, M.; Meng, S.; Wang, Q.; Si, W.; Huang, W.; Dong, X. Nickel−Cobalt Oxide Decorated Three-Dimensional Graphene as an Enzyme Mimic for Glucose and Calcium Detection. *ACS Appl. Mater. Interfaces*, **2015**, 7, 21089−21094.
9. Chen, Z.; Ren, W.; Gao, L.; Liu, B.; Pei, S.; Cheng, H.-M. Three-Dimensional Flexible and Conductive Interconnected Graphene Networks Grown by Chemical Vapour Deposition. *Nat. Mater.* **2011**, 10, 424−428.
10. Amal Raj, M.; Abraham John, S. Fabrication of Electrochemically Reduced Graphene Oxide Films on Glassy Carbon Electrode by Self-Assembly Method and Their Electrocatalytic Application. *J. Phys. Chem. C* **2013**, 117, 4326−4335.
11. Lawes, S.; Riese, A.; Sun, Q.; Cheng, N.; Sun. X. Printing nanostructured carbon for energy storage and conversion applications. *Carbon* **2015**, 92, 150-176.
12. Korhonen, H.; Sinh, L. H..; Luog, N. D.; Lehtinen, P.; Verho, T.; Partanen, J.; Seppälä, J. Fabrication of graphene-based 3D structures by stereolithography. *Phys. Status Solidi A* **2015**, 213, 982-985.
13. Da Costa, T. H., Song, E.; Tortorich, R. P.; Choi, J. W. A paper-based electrochemical sensor using inkjet-printed carbon nanotube electrodes, *ECS J Sol State Sci technol*. **2015,** 4 (10) S3044-S3047.
14. Das, S. R.; Nian, Q.; Cargill, A. A.; Saei, M.; Cheng, G. J.; Calussen, J. C. 3D nanostructured inkjet printed graphene via UV-pulsed laser irradiation enables paper-based electronics and electrochemical devices. *Nanoscale*, **2016**, 8, 15870—15879
15. Griffiths, K.; Dale, C. Hedley, J.; Kowal, M. D.; Kaner, R. B.; Keegan, N. Laser-scribed graphene presents an opportunity to print a new generation of disposable electrochemical sensors. *Nanoscale*, **2014**, 6, 13613—13622
16. Strong, V.; Dubin, S.; El-Kady, M. F.; Lech, A.; Wang, Y.; Weiller, B. H.; Kaner, R. B. Patterning and electronic tuning of laser scribed graphene for flexible all-carbon devices. *ACS Nano*, **2012** 6(2), 1395-1403.
17. Ye, R. James, D. K.; Tour, J. M. Laser-Induced Graphene. *Acc chem res*, **2018**, 51, 1609-1920

18. Lin, J.; Peng, Z.; Liu, Y.; Zepeda, F.; Ye, R.; Samuel, E. L. G.; Yacamn, M. J.; Yakobson, B. I.; Tour, J. M. Laser-induced graphene films from commercial polymers. *Nature Commun.* **2014,** 5, 5714.
19. Nayak, P.; Kurra, N.; Xia, C; Alshareef, H. Highly efficient laser scribed graphene electrodes for on-chip electrochemical sensing applications. *Adv. Electron. Mater*. **2016**, 2, 1600185.
20. Burke, M.; Larrigy, C.; Vaughan, E.; Paterakis, G.; Sygellou, L.; Quinn, A. J.; Herzog, G.; Galiotis, C., Iacopino D. Fabrication and electrochemical properties of three dimensional porous graphitic electrodes obtained by low-cost laser induced graphene (LIG). *ACS Omega*, **2020**, 5, 1540−1548.
21. Yen, G. C.; Duh, P. D.; Tsai, H. L. Antioxidant and pro-oxidant properties of ascorbic acid and gallic acid. *Food Chem.* **2002**, 79, 307-313.
22. Liu, Q.; Zhu, X.; Huo, Z.; He, X.; Liang, Y.; Xu, M. Electrochemical detection of dopamine in the presence of ascorbic acid using PVP/graphene modified electrodes. *Talanta*, **2012**, 97, 557-562.
23. Hou, T.; Gai, P.; Song, M.; Zhang, S.; Li, F.; Synthesis of three-layered SiO2@Au nanoparticles@polyaniline nanocomposite and its application in simultaneous electrochemical detection of uric acid and ascorbic acid. *J Mater. Chem. B.* **2016**, 13, 2314-2321.
24. Xu, G.; Jarjes, Z; Desprez, V; Kilmartin, P; Travas-Sejdic, J. Sensitive, selective, disposable electrochemical dopamine sensor based on PEDOT-modified laser scribed graphene. *Biosens. Bioelectr.* **2018**,107 184-191.
25. Nicholson, R. S. Theory and Application of Cyclic Voltammetry for Measurement of Electrode Kinetics. *Anal. Chem.* **1965**, 37, 1351-1355.
26. Romero, F. J.; Salinas-Castillo, A.; Rivadeneyra, A.; Albrecht, A.; Godoy, A.; Morales, D. P.; Rodriguez, N. In-Depth Study of Laser Diode Ablation of Kapton Polyimide for Flexible Conductive Substrates. *Nanomaterials*. **2018**, 8, 517-528.
27. Zhang, Z.; Song, M.; Hao, J.; Wu, K.; Li, C.; Hu, C; Visible light laser-induced graphene from phenolic resin: A new approach for directly writing graphene-based electrochemical devices on various substrates*. Carbon* **2018**, 127, 287-296.
28. Ferrari, A. C.; Basko, D. M. Raman spectroscopy as a versatile tool for studying the properties of graphene. *Nat. Nanotechnol*. **2013**, 8, 235-246.
29. Lespade, P.; Al-Jishi, R.; Dresselhaus, M. S. Model for Raman scattering from incompletely graphitized carbons. *Carbon* **1982**, 20, 427-431. 27
30. Nemanich, R. J.; Glass, J. T.; Lucovsky, G.; Shroder, R. E. Raman scattering characterization of carbon bonding in diamond and diamondlike thin films. *J. Vac. Sci. Technol. A: Vacuum, Surfaces, Film.* **1988**, 6, 1783-1787.
31. Eckmann, A.; Felten, A.; Mishchenko, A.; Britnell, L.; Krupke, R.; Novoselov, K. S.; Casiraghi, C. Probing the nature of defects in graphene by Raman Spectroscopy. *Nano Lett.* **2012**, 12, 3925-3930.
32. Yuan, B.; Zeng, X.; Xu, C.; Liu, L.; Zhang, D.; Fan, Y. Electrochemical modification of graphene oxide bearing different types of oxygen functional species for the electro-catalytic oxidation of reduced glutathione*. Sens. Act. B: Chemical.* **2013,** 184, 15-20.

33. Stergiu. D. V.; Diamanti, E. K.; Gournis, D.; Prodomis, M. I. Comparative study of the different types of graphenes as electrocatalysts for ascorbic acid. *Electrochem. Comm*. **2010,** 12 (10), 1307-1309.
34. Fisher, A. E.; Show. F.; Swain, M. Electrochemical Performance of Diamond Thin-Film Electrodes from Different Commercial Sources. *Anal Chem*. **2004**, 74, 2553-2560.
35. Chen, P.; McCreery, R. L. Control of Electron Transfer Kinetics at Glassy Carbon Electrodes by Specific Surface Modification. *Anal Chem.* **1996**, 68, 3958-3965.
36. Tang, L.; Wang, Y.; Li, Y.; Feng, H.; Li, L.; Li, J. Preparation, structure, and electrochemical properties of reduced graphene sheet films. *Adv Funct. Mater*. **2009**, 19, 2782-2789
37. Bard, A. J.; Faulkner, L. R.; Electrochemical Methods, 2nd ed. John Wiley &sons, New York, **2010**.
38. Muratova, I. S.; Mikhelson, K. N.; Ermolenko, Yu.; Offenhäusser, A.; Mourzina, Yu. On "resistance overpotential" caused by a potential drop along the ultrathin high aspect ratio gold nanowire electrodes in cyclic voltammetry. *J Solid State Electrochem,* **2016**, 20, 3359-3365.
39. Yu, B.; Kuang, D.; Liu, S.; Liu, C.; Zhang, T. Template-assisted self-assembly method to prepare three-dimensional reduced graphene oxide for dopamine sensing. *Sensors and Actuators B,* **2015**, 205, 120-126.
40. Streeter, I.; Wildgoose, G. G.; Shao, L.; Compton, R. G. Cyclic voltammetry on electrode surfaces covered with porous layers: An analysis of electron transfer kinetics at single-walled carbon nanotubes modified electrodes. *Sens. Act. B: Chemical*,**2008,** 133, 462-466
41. Bard, A. J.; Faulkner, L. R. Electrochemical methods: Fundamentals and Applications, 2nd ed, Wiley: New York, **2001**, chapter 11, sect 7.
42. Wang, Y.; Huang, Y.; Wang, B.; Fang, T.; Chen, J.; Liang, C. Three-dimensional porous graphene for simultaneous detection of dopamine and uric acid in the presence of ascorbic acid. *Journal of Electroanalytical Chemistry,* **2016**, 782, 76-83.
43. Swinya DL, Martín-Yerga D, Walker M, Unwin PR. Surface Nanostructure Effects on Dopamine Adsorption and Electrochemistry on Glassy Carbon Electrodes. *J Phys Chem C Nanomater Interfaces*. **2022**; 126(31):13399-13408. doi: 10.1021/acs.jpcc.2c02801.
44. James A. Behan, Filip Grajkowski, Dilushan R. Jayasundara, Laia Vilella-Arribas, Max García-Melchor, Paula E. Colavita, Influence of carbon nanostructure and oxygen moieties on dopamine adsorption and charge transfer kinetics at glassy carbon surfaces, *Electrochimica Acta*, Volume 304, **2019**, Pages 221-230, ISSN 0013-4686, https://doi.org/10.1016/j.electacta.2019.02.103.

Chapter 3: Laser-Induced Graphene Biosensors for Label-Free Detection of IL-6

3.1 Abstract

Interleukin-6 (IL-6) is an important immuno-modulating cytokine playing a pivotal role in inflammatory processes in disease induction and progression. As IL-6 serves as an important indicator of disease state, it is of paramount importance to develop low cost, fast and sensitive improved methods of detection. In this chapter an electrochemical immunosensor platform is presented, based on the use of highly porous laser-induced graphene (LIG) electrodes fabricated by direct laser writing of commercial polyimide tapes and chemically modified with capture IL-6 antibodies. The unique porous and 3D morphology, as well as the high density of edge planes of the LIG electrodes, resulted in a fast heterogeneous electron transfer (HET) rate, k^0 = 0.13 cm/s. The resulting immunosensor showed a linear response to log of concentration in the working range of 10 to 500 pg/mL, and low limit of detection (LOD) of 5.1 pg/mL IL-6 in phosphate buffer saline. The total test time was approximately 90 min, faster than the time required for ELISA testing. Moreover, the assay did not require additional sample pre-concentration or labelling steps. The immunosensor shelf-life was long, with stable results obtained after 6 weeks of storage at 4 °C, and the selectivity was high, as no response was obtained in the presence of another inflammatory cytokine, Interlukin-4. These results show that laser-fabricated LIG electrodes can be used as selective and sensitive electrochemical immunosensors and offer a viable option for rapid and low-cost biomarker detection for point-of-care analysis.

Published: Nanomaterials 2021, 11, 2110. https://doi.org/10.3390/nano11082110

3.2 Introduction

Interleukin-6 (IL-6) is a soluble protein secreted from a variety of innate and adaptive immune and non-immune cell types and involved in the modulation of many cellular reactions including sensitisation, chemically-induced tissue damage, control of cell replication and apoptosis[1,2]. IL-6 is best known for its perilous role in generating a variety of inflammatory responses underpinning psoriasis, rheumatoid arthritis, cardiovascular disease, and inflammatory bowel disease[3,4]. IL-6 is relevant to the early diagnosis of many diseases such as diabetes and Alzheimer's as well as being a biomarker over-expressed by several types of cancer, including head and neck squamous cell carcinoma, breast, oral, cervical and colorectal cancer[5–9]. Recently, IL-6 has been chosen as a potential target for COVID-19 therapy[10]. Due to its potential as an early diagnostic indicator of inflammatory events, sensitive detection of IL-6 is of the utmost importance. However, detection is challenging in situ owing to low IL-6 serum concentrations, lower than 6 pg/mL in healthy humans and reaching elevated values of >80 pg/mL in cases of cancer or abnormal inflammation[11,12].

Traditionally, IL-6 is quantitatively detected in blood by enzyme-linked immunosorbent assays (ELISA). In spite of their extensive use for clinical protein determination and low detection limits (as low as 3 pg/mL for protein biomarkers) such assays suffer limitations in analysis time, sample size, and real-time measurements[13,14]. Other quantitative methods, such as antibody array assays and bead-based assays suffer similar limitations and require costly, high-maintenance instrumentation, specialised infrastructure and highly skilled personnel[15]. As an alternative, a number of electrochemical sensors have been recently developed, showing high sensitivity, strong selectivity and good detection limits[16–19]. For example, Wang et al. developed a carbon nanotubes (CNTs)-based electrochemical

impedance sensor able to detect IL-6 antigen in serum at a low limit of 0.01 fg mL^{-1}. The sensor exhibited high stability and selectivity and its sensitivity did not change upon storage at 4 °C, over one month[20]. Tertis et al. developed a label-free electrochemical aptasensor based on gold and polypyrrole nanoparticles able to detect IL-6 over a wide linear range from 1 pg mL^{-1} to 15 mg mL^{-1} with a detection limit of 0.33 pg mL^{-1}[18]. Jensen et al., fabricated gold nanoparticle arrays by inkjet-printing, and demonstrated low cost detection of IL-6 with detection limit of 20 pg mL^{-1} in bovine serum, sensitivity of 11.4 nA pg^{-1} cm^{-2}, and a linear dynamic range of 20–400 pg/mL[17]. As well as the direct immunoassays described, a variety of indirect competitive electrochemical, sandwich nanoparticle labelled electrochemical and sandwich enzyme linked electrochemical immunoassays have been developed. A general overview of all recent advances in electrochemical sensing of IL-6 has been recently compiled in a comprehensive review by Khan et al.[21]

Graphene and graphitic materials possess remarkable physical and chemical properties such as a wide electrochemical window and electrocatalytic activity for many redox reactions, which make them particularly suitable for use as electrochemical sensors[22–24]. However, standard fabrication techniques of graphene-like electrode materials, including chemical vapour deposition (CVD)[25] and laser ablation[26] are usually costly, time consuming and non-environmentally friendly. Other alternative methods such as screen printing or inkjet printing require the use of binders, additives or post print processes such as laser, thermal or photonic annealing, that affect the electrochemical sensitivity and increase the overall cost of production of the resulting electrodes[27–29]. Recently, direct laser writing techniques have been proposed as an alternative for the fabrication of disposable graphene-like electrochemical sensors. In this method, pioneered by the group of Tour et al., a simple

computer-aided laser-scribing process enabled fast patterning of a variety of electrode designs on flexible polyimide (Kapton tape) under ambient conditions[30,31]. The capability of laser-fabricated LIG electrodes to act as electrochemical sensors has been investigated recently by our group and others[32,33]. Specifically, it was found that electrodes fabricated by 450 nm laser diode irradiation exhibited fast heterogeneous electron transfer rates (HET) ascribed to the highly porous and 3D morphology of the resulting structures, characterised by high surface area, large conductive networks and abundance of defect and edge plane, facilitating analyte adsorption and circulation[33]. As a result of their superior electrocatalytic properties, such electrodes enabled label-free concomitant detection of the biomarkers dopamine, ascorbic and uric acid, usually disabled in bulk electrodes by the overlapping of their oxidation potentials[33]. Moreover, various routes for the biomodification of LIG electrodes for biosensing applications have been developed recently. For example, Nayak et al. fabricated wearable biosensors and demonstrated detection of glucose in buffer, serum and blood[34]. Laser-scribed electrodes have been employed in food safety applications, showing an ability to detect biogenic amines in food samples[35], low levels of chloramphenicol antibiotic[36], and salmonella in chicken broth[37]. Importantly for diagnostic applications, the ability of LIG electrodes to detect thrombin via aptamer electrode modification, was recently demonstrated by Fenzl et al.[38]. The electrodes allowed fast (<1 h), sensitive and selective responses in buffer and serum, comparable and/or superior to other electrochemical detection methods available in literature. A new class of laser scribed nanostructured gold modified electrochemical sensor was recently realised by Rauf et al. The system was used as electrochemical aptasensor for detection of human epidermal growth factor receptor 2 (Her-2) and displayed ~2-fold

enhancement in sensitivity and electrocatalytic activity compared to bare laser scribed electrodes and commercially available screen-printed gold electrodes[39].

In this chapter, we present the use of LIG electrodes for the detection of the inflammatory cytokine IL-6. Electrodes were fabricated by a low-cost laser cutter tool equipped with a 450 nm wavelength laser, which led to formation of conductive porous structures with a high density of edge planes displaying spectral signatures of nanocrystalline graphitic carbon. The 3 W 450 nm laser cutting system offered significant cost reductions vs. high-powered CO_2 systems, while retaining the high quality of graphitic material produced. The surface of the obtained electrodes was modified with anti-IL-6 recombinant antibodies selective for the inflammatory IL-6 cytokine. The assay was performed by monitoring the decreased electrochemical response (differential pulse voltammetry, DPV) to the redox probe $[Fe(CN)_6]^{3-/4-}$, associated to the reduced access of the probe to the anti-IL-6 recombinant antibodies-modified electrode following successful IL-6 binding. The resulting immunosensor response was linearly calibrated with log of concentration values between 10–500 pg/mL IL-6 concentration range and a low LOD in phosphate-buffered saline (PBS). The shelf-life stability was good, as detection responses were recorded for devices stored at 4 °C for six weeks. The faster time of analysis and lower cost compared to traditional ELISA methods make these immunosensors attractive for future diagnostic and point-of care applications.

3.3 Materials and Methods

3.3.1 Materials

Polyimide films (80 μm thickness) were purchased from Radionics, Ireland. Chemical reagents of 1-pyrenebutyric acid (PBA), potassium chloride, potassium ferrocyanide

($K_4[Fe(CN)_6]$), N-hydroxysuccinimide (NHS), 1-ethyl-3-(3-dimethylaminopropyl) carbodiimide (EDC) and bovine serum albumin (BSA), were purchased from Sigma-Aldrich, Ireland. Dulbecco's phosphate saline (PBS) pH 7.4 and fetal bovine serum (FBS) were purchased from Gibco, Biosciences Limited, Ireland. Purified Rat Anti-IL-6, Recombinant Human IL-6 were purchased from BD Biosciences, UK. The IL-6 ELISA was sourced from R&D Systems, Bio-Techne, UK. All solutions were of analytical grade and were prepared using deionised Milli-Q water (resistivity 18.2 MΩ-cm) and deoxygenated with N_2 prior to electrochemical analysis.

3.3.2 Electrode Fabrication

LIG electrodes were fabricated as previously reported by raster scanning of designed electrode structures on polyimide by a KKmoon Compact Automatic Desktop Laser Engraving Machine equipped with a 3 W laser and illumination wavelength of 450 nm. The laser was operated at 30% power and 40% depth adjustment. After fabrication, electrodes were rinsed with acetone, isopropanol and deionised water to remove any residues from the laser engraving process.

3.3.3 Characterisation

The morphology of LIG electrodes was characterised by a cold-cathode field-emission scanning electron microscope (JEOL SEM, JSM- 7500F, Jeol, UK) operating at 5 kV acceleration voltage. Raman measurements were performed with a Renishaw inVia Raman system (Renishaw, UK) equipped with a 514 nm helium–neon laser. The laser beam was focused onto the sample through a Leica 20× objective with 0.4 N.A. Acquisition time was 10 s and measured power was 3 mW.

3.3.4 Electrode Modification

The surface of LIG electrodes was modified by immersion of the electrode in 1-PBA solution (DMSO, 250 mM) for 60 min. After rinsing with PBS, the electrode was immersed in an aqueous solution of 75 mM EDC:50 mM NHS for 90 min, followed by immersion in PBS for 15 min. Next, the LIG electrode was exposed to 200 µL of a 2.5 µg/mL PBS solution of Purified Rat Anti-Human IL-6 for 90 min followed by extensive washing with PBS. The unreacted electrode surface was blocked with BSA to reduce non-specific binding and subsequently rinsed with PBS, prior to IL-6 binding.

3.3.5 Electrochemical Analysis

Cyclic voltammetry (CV) and differential pulse voltammetry (DPV) electrochemical measurements were performed with an Autolab PGSTAT 302N potentiostat (Metrohm, UK) and hand-held EmStatblue (PalmSens, UK) electrochemical using a Pt wire as counter electrode, Ag/AgCl as reference electrode and LIG as working electrode. The three electrodes were assembled in a Teflon cell with a circular area of 8 mm diameter exposed to the electrolyte. CV experiments were carried out in 1 M KCl supporting electrolyte, 5 mM $[Fe(CN)_6]^{4-/3-}$ redox probe. The scan rates used for CV measurements were 10, 25, 50, 100 and 200 mV/s, in a potential range from −0.1 to 0.6 V. N_2 was purged in the electrolyte solutions for 30 min prior to measurements.

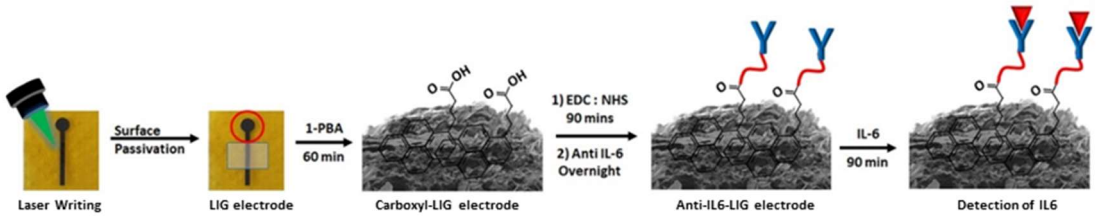
3.3.6 Electrochemical Interleukin-6 (IL-6) Detection

Recombinant human IL-6 in 200 µL aliquots across a concentration range of 10–500 pg/mL in PBS was dispensed onto the antibody-modified LIG electrode for 90 min. After rinsing with PBS, DPV measurements were performed using $[Fe(CN)_6]^{3-/4-}$ (0.01 V/s scan rate, 0.025 V modulation amplitude, 0.005 V step potential, 0.5 s

interval time and 0.05 s sample width). Interference studies were performed in 10 % BSA solution (PBS) in the presence of 5 mM $[Fe(CN)_6]^{4-/3-}$ redox probe, as well as a selectivity test by examining the sensor's response to IL-4 as a model interferent. To mimic clinical testing conditions, samples were examined in 10% FBS (10% w:w in PBS). For both testing scenarios, the electrode was immersed in solutions containing IL-6 at concentrations from 0 (blank) to 500 pg/mL for 90 min. After rinsing with PBS, DPV measurements were performed as described.

3.4 Results and Discussion

The fabrication and surface modification of LIG electrodes, and the detection mechanism of IL-6 cytokine, are shown in Scheme 3.1. Briefly, LIG electrodes of a "lollipop" shape were fabricated by laser irradiation of commercial polyimide tapes, as described previously[33]. Prior to chemical modification, the "lollipop" leg was passivated with nail varnish to ensure selective modification of the surface. The circular part of the electrode was then functionalised with 1-PBA, followed by anti-IL-6 attachment via EDC:NHS coupling. Finally, the electrode was incubated in the targeted IL-6 cytokine solution for 90 min prior to electrochemical detection.



Scheme 3.1 Schematic of LIG electrode fabrication, surface modification and interleukin-6 (IL-6) capture.

Figure 3.1a shows a SEM image of the LIG surface, which was characterised as a flaky structure displaying high porosity and high surface area. Importantly for electrochemical analysis, the electrode surface showed the formation of an extended 3D network of LIG sheets with a high density of accessible edges constituted by kinked

and wrinkled areas. The Raman spectrum of the LIG electrode (Figure 3.1b) was characterised by three main peaks cantered at 1349, 1581 and 2696 cm^{-1} corresponding to the D peak (associated to bent sp^2 carbon bonds and with the presence of defects), G peak (E2g vibration mode of graphitic carbon) and 2D peak, respectively. More specifically, the maximum in the *D* region could be fit with a single, sharp Lorentzian with full-width at half-maximum intensity, *FWHM*(*D*)~47 cm^{-1}, consistent with low disorder. The ratio $I_D/I_G \approx 1$ confirmed the crystalline nature of the graphitised surface and was consistent with the formation of nanocrystalline graphitic domains in a disordered carbon matrix[40]; the high I_{2D}/I_G ratio (0.78) indicated a low number of graphene layers[31,40]. Moreover, the 2D peak could be fitted by a single Lorentzian peak centered at 2696 cm^{-1}, with *FWHM*(*2D*) of 81 cm^{-1}. This profile was consistent with 2D graphene-like carbon structures consisting of randomly stacked graphene layers along the c-axis[31].

The electrochemical response of the LIG electrodes to inner sphere redox mediator $[Fe(CN)_6]^{3-/4-}$ was investigated in detail, key for future biosensor performance. Figure 3.1c shows the cyclic voltammograms recorded in 5 mM $[Fe(CN)_6]^{3-/4-}$ in a 1 M KCl supporting electrolyte in the interval 50–500 mV/s scan rates. The electrodes displayed a quasi-reversible behaviour, shown by the linear relationship between the peak oxidation/reduction current and the square root of the scan rate (inset Figure 3.1c) and indicated a semi-infinite linear diffusion reaction process with correlation coefficients for oxidation and reduction processes greater than 0.99. The average peak separation, ΔE_p, calculated over four electrodes at 100 mV/s scan rate, was 112 mV (σ = 5.8 mV). The HET constant k^0 was calculated as 1.3×10^{-1} cm/s ($\sigma = 1.8 \times 10^{-2}$ cm/s; n = 4), as determined by the Nicholson method.[41] This k^0 value was over one order of magnitude higher than values reported for other graphitic carbon electrodes obtained

by direct laser writing.[32,33,37] In order to determine the contribution of the high porosity/surface area of the laser scribed material, a comparison between the electrode geometric area and the electrochemically active area (calculated using the Randles–Sevcik equation) was carried out.[42] The electroactive surface area (ESA, 11 mm^2) was approximately 22% higher than the estimated geometric area (9 mm^2), indicating the significance of the porous nature of the electrode material. The electrochemical behaviour was also tested over four electrodes (Figure 3.1d), which showed high reproducibility of electrochemical performance, key for the development of future reliable and stable biosensors.

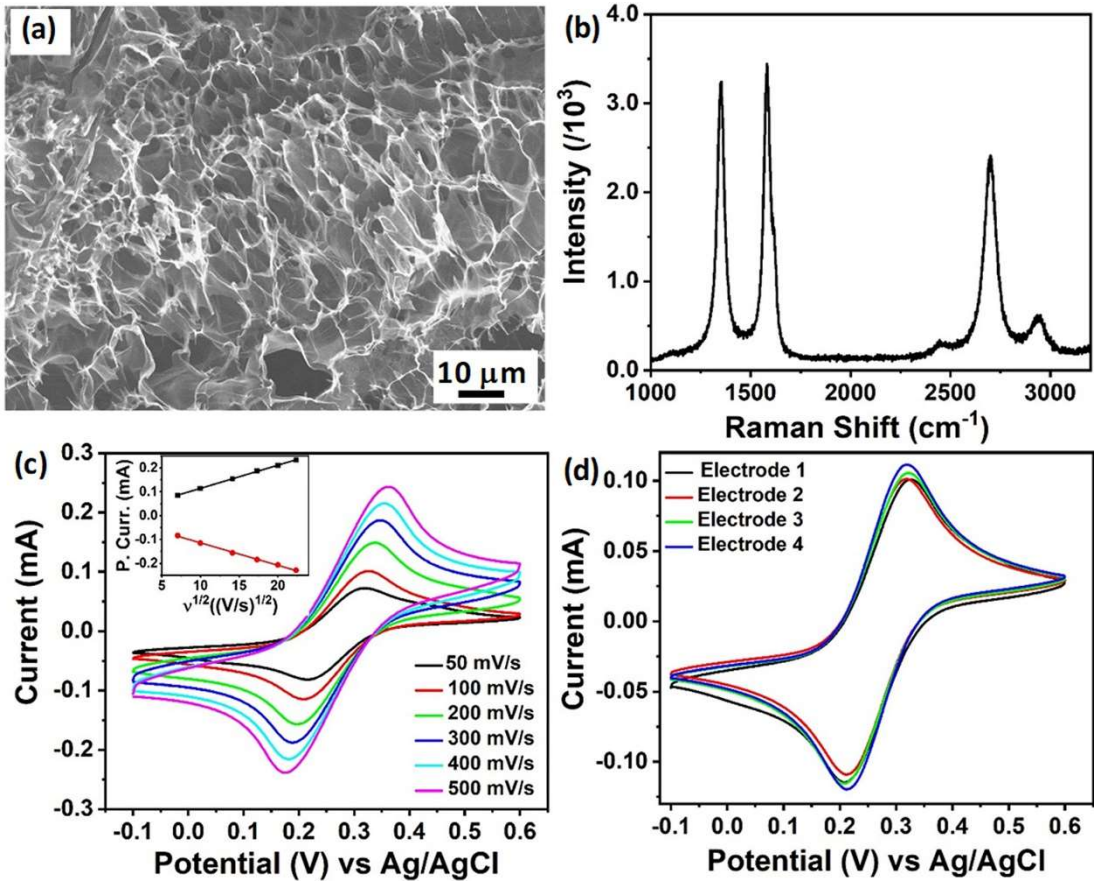


Figure 3.1 a) Scanning electron microscope (SEM) image of a typical LIG electrode; **b)** Raman spectrum of LIG electrodes; **c)** cyclic voltammograms of LIG electrodes of 5 mM $[Fe(CN)_6]^{3-/4-}$ in 1 M KCl; Inset: peak oxidation and reduction current values vs. square root of potential scan rate; **d)** cyclic voltammograms of LIG electrodes of 5 mM $[Fe(CN)_6]^{3-/4-}$ in 1 M KCl for four different electrodes.

Prior to the investigation of biosensing performance, preliminary studies were carried out in order to assess the capabilities of the unmodified LIG surface to work

effectively as a biosensor. The DPV signal in response to $[Fe(CN)_6]^{3-/4-}$ in 0.1 M PBS supporting electrolyte was used to gauge the effect of surface modification. Figure 3.2a compares the DPV signals recorded at a bare LIG electrode and an electrode deposited with anti-IL-6. No significant change in peak current was observed. Figure 3.2b compares the DPV responses at two LIG surfaces functionalised with EDC:NHS, one of them with anti-IL-6 deposited on it. A slight increase in maximum current was observed at the electrode with anti-IL-6 deposited, contrary to the expected decrease. These data suggest that the electrodes are not suitable for direct anti-IL-6 modification, and that the concentration of −COOH groups at the electrode surface was too low to support anti-IL-6 modification via EDC:NHS coupling. This result is consistent with XPS data previously reported for this material which showed an atomic percentage of −COOH equal to 1.96%.[33] In order to introduce more −COOH surface groups, electrodes were treated with 1-PBA. After 1-PBA treatment, EDC:NHS modification was re-attempted. Figure 3.2c shows the DPV results for a bare electrode and a PBA/EDC:NHS-modified electrode with anti-IL-6 deposited. In this instance the anti-IL-6 deposition led to a large drop in peak current (14.61 μA). This indicates the successful EDC:NHS-mediated attachment of anti-IL-6 to the electrode surface—the lower DPV response being attributed to lower accessibility of analyte to the modified electrode surface.

The optimal concentration of 1-PBA (250 mM) was determined by monitoring the access of the redox marker $[Fe(CN)_6]^{3-/4-}$ to the electrode surface for 1-PBA concentrations ranging from 10 to 500 mM in comparison to the response to the bare electrode. 1-PBA treatment of the electrode surface should introduce negatively charged −COOH groups by π–π interaction, resulting in electrostatic repulsion of $[Fe(CN)_6]^{3-/4-}$.[43] This would cause a reduction of peak currents, and a retardation of

the reaction (larger peak separations). Cyclic voltammograms (see Figure 3.2d) showed that the initial peak current associated to the bare LIG electrode was as high as 104 μA, due to the unhindered response of $[Fe(CN)_6]^{3-/4-}$. Progressive increases in 1-PBA concentrations on the LIG electrode resulted in decreased maximum current to 32.52 μA and an overall spreading of the peaks was additionally observed, consistent with the increase in −COOH surface coverage.

The EDC:NHS ratio was optimised by varying the concentrations, as reported in Figure 3.2e, f. Only after exposure to 75 mM EDC:50 mM NHS did the LIG electrode show a decrease of the peak current upon binding of IL-6, proving that successful binding of anti-IL-6 via EDC:NHS coupling had occurred.

The concentration of anti-IL-6 was chosen by monitoring the change of current intensity of various electrodes upon binding of different anti-IL-6 concentrations. Figure 3.2g showed that the highest differential current in DPV was obtained with 2.5 μg/mL anti-IL-6 concentration, which was then the concentration employed throughout this work.

Figure 3.2h shows CV curves for $[Fe(CN)_6]^{3-/4-}$ with optimised conditions. Progressive blocking of the electrode surface, first by the attachment of anti-IL-6 and then by IL-6 to the LIG electrodes, leads to a progressive dropping of the peak current, as seen in the histogram inset of Figure 3.2h displaying the trend of peak current progression (background subtracted—a much larger capacitive current is observed for the modified electrodes, obscuring the fact that the peak current has indeed dropped).

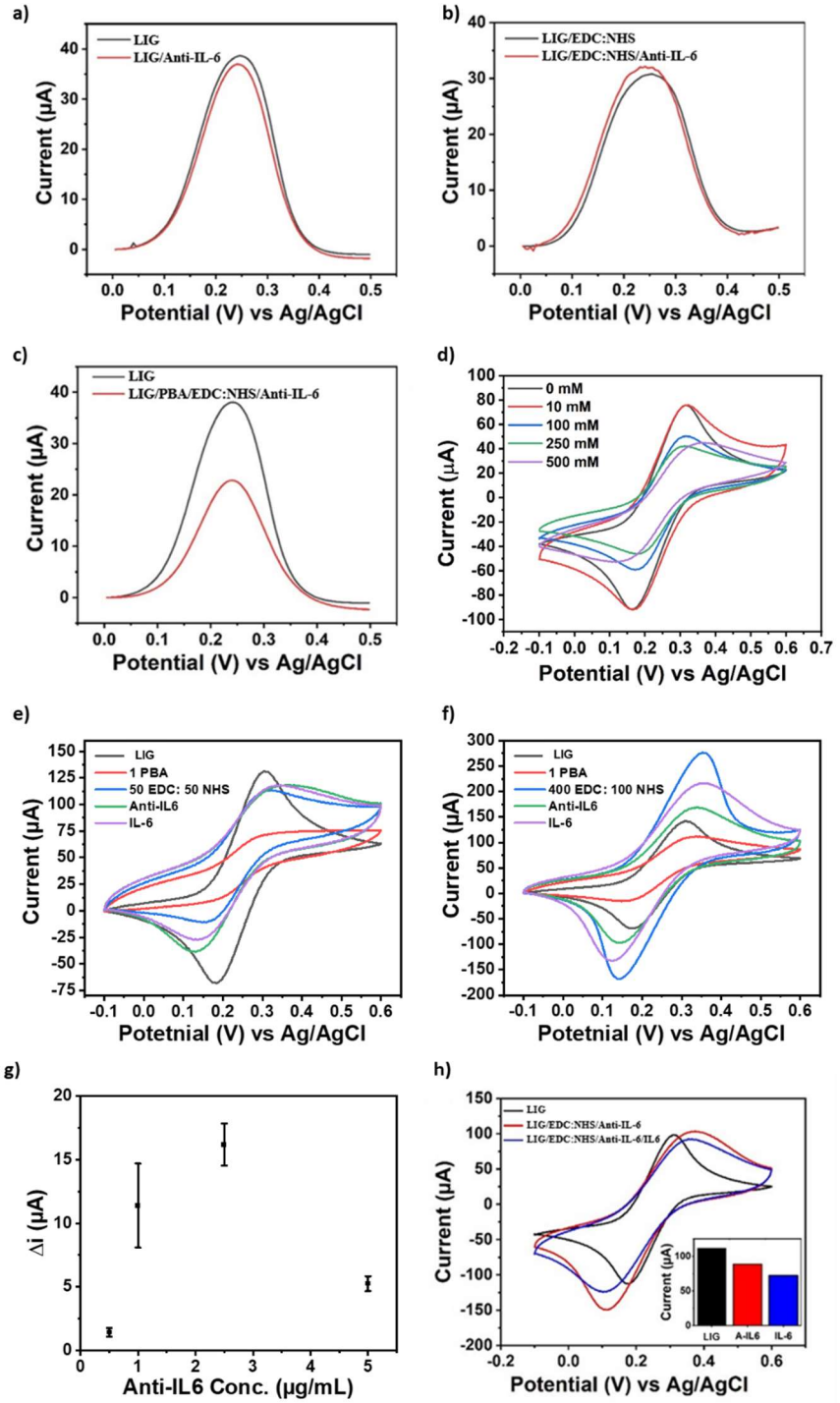


Figure 3.2 a) DPV curves before and after attachment of anti-IL-6 antibody; **b)** LIG electrodes modified with EDC:NHS before and after anti-IL-6 attachment; ; **c)** DPV curves of LIG electrode with 1-PBA and EDC:NHS modification before and after attachment of anti-IL-6 via EDC:NHS coupling; **d)** CVs for electrodes exposed to different concentrations of 1-PBA; **e)** CVs for electrodes exposed to 50 mM EDC: 50 mM NHS and **f)** 400 mM EDC: 100 mM NHS; **g)** Differential current values obtained from CVs for varying concentrations of anti-IL6 **h)** CVs showing all different stages of LIG electrode modification for. All voltammetric experiments using 5 mM $[Fe(CN)_6]^{3-/4-}$ in 0.1 M PBS at pH 7.4.

In order to test the capability of the fabricated biosensor for IL-6 detection, LIG working electrodes were bio-modified as described above, assembled in a Teflon electrochemical cell and exposed to various IL-6 concentrations ranging from 0 to 500 pg/mL. Following an incubation time of 90 min, the electrochemical response of the electrode to $[Fe(CN)_6]^{3-/4-}$ was measured by DPV. Figure 3.3a shows the progressive decrease of DPV signal with the increase of IL-6 concentration, in agreement with the reduction of electrode surface available for the redox marker. Measurements were made in triplicate, and results showing the mean standard deviation are displayed in Figure 3.3b. The DPV peak currents decreased linearly with the log of the concentration according to the equation $y = -75.4 - 6.5x$, where y is current in μA and x is the log of IL-6 concentration in g/mL ($R^2 = 0.9738$). From the data, it was calculated that the current drop was equal to −3.9 μA at 10 pg/mL IL-6 concentration and estimated as −1.95 μA at 5 pg/mL IL-6, a concentration value equivalent to the range found in healthy subjects. The LOD was calculated using the 3σ method. This form of calculation is generally applied to a linear calibration curve, where the formula is simply

$$LOD = 3\sigma/m \qquad \text{(eq. 3.1)}$$

where *m* is the slope of the calibration curve. The calibration curve presented in this chapter is linear with respect to the Log of the concentration. The current values are differential and are negative. This means that the above formula must be modified: the y-intercept will be non-zero and must be considered, as the origin no longer represents a point of zero concentration and zero signal; *LOD* must be replaced by *Log(LOD)*, adding an extra calculation step; we must consider the negative value of σ:

$$Log(LOD) = (-3\sigma - c)/m \qquad \text{(eq. 3.2)}$$

$$LOD = 10^{(-3\sigma - c)/m} \qquad \text{(eq. 3.3)}$$

where *c* is the y-intercept of the calibration line. Equation 3.3 was used to calculate the value of the LOD for these sensors. The result was 5.1 pg mL^{-1}. Normal levels of IL-6 in humans are ~ 6 pg mL^{-1}, with levels exceeding 80 pg mL^{-1} in the case of inflammatory events.[51, 52] This LOD and linear range prove the viability of this immunosensor.

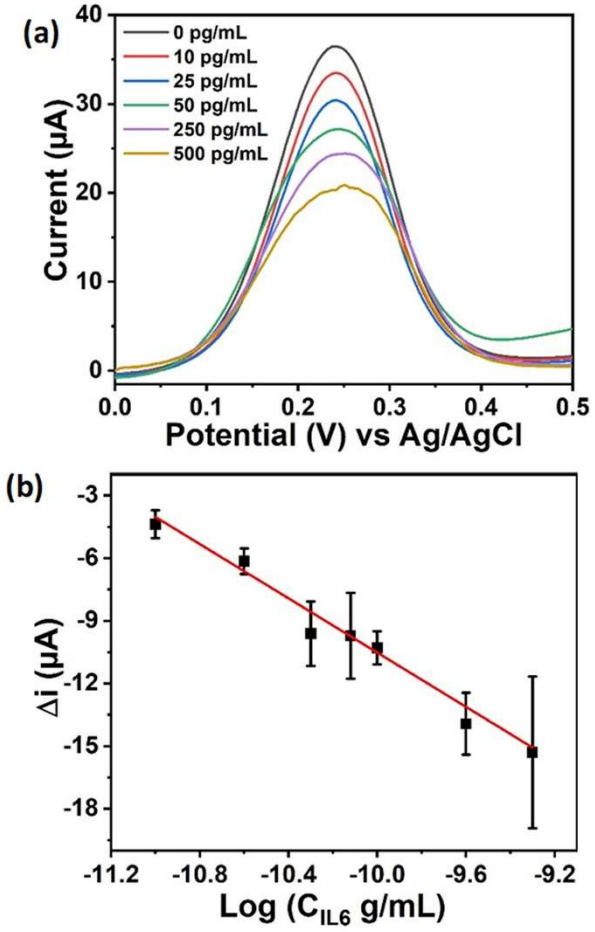


Figure 3.3 a) DPV curves of LIG biosensor at varying concentrations of IL-6 conducted in PBS at pH 7.4 containing 5 mM $Fe(CN)_6]^{3-/4-}$; **b)** Change of the DPV peak current of LIG biosensor vs Ag/AgCl at varying IL-6 concentration, n = 3.

The performance of the developed electrochemical assay was benchmarked against ELISA, the traditional method commonly used to assess the concentration of IL-6. Results of the ELISA test are reported in Figure 3.4 and displayed comparable LOD to the immunosensor. However, the time required for the performing of the ELISA test as per the manufacturer's instructions was 2 hours, followed by a further 2 hours of

labelling/substrate incubation, substantially longer than the sub-90 min demonstrated by the present method.

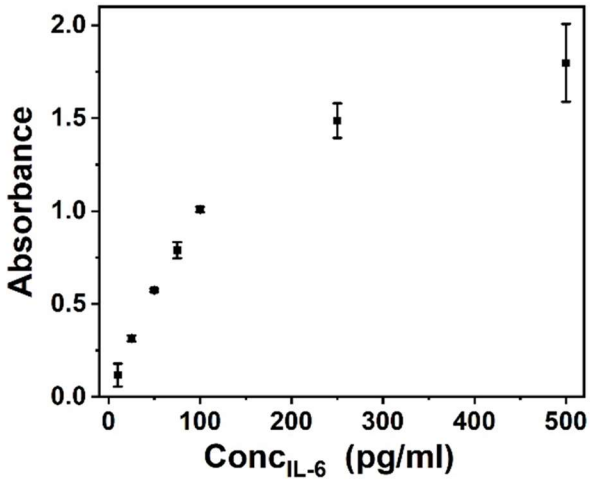


Figure 3.4 ELISA detection of IL6

The performance of the developed sensor was also compared with other electrochemical sensors reported in literature as shown in Table 3.1. The developed LIG sensor displayed a comparable LOD to most IL-6 sensors and at the same time offered the advantage of low-cost materials and fabrication methods. In fact, the sensor demonstrated low cost (estimated cost ca. €2 per test based on cost of chemicals and electricity used) and the technology presented offers easy routes for upscaling of production and development of on-chip and personalised healthcare solutions.

Table 3.1 Comparison of different electrochemical biosensors for IL-6 detection *.

Material	Transducer	Technique	Measured Range (pg/mL)	Limit (pg/mL)	Medium	Ref.
SWNT/ GSH-AuNPs	PG	CA	20-4,000	10	Serum	45
FC-PPN	GC	SWV	2-20,000	1	PBS	46
Au NP	Gold	SWV	5-50,000	2	PBS	19
Ppy/Au NPs	SPGEs	EIS	1-15	0.3	PBS	18
SWCNTs	PG	CA	50-500	30	Human serum	46
Au NP ink	Inkjet electrodes	CA	20-40	20	Calf serum	17
(Au NP)-graphene-SiO_2	ITO	CA	1 -40	0.3	PBS	16
Au NPs/ SWCNTs	SiO_2/Si	EIS	10 -10^7	10	Serum	6
Ag NPs	ERGO-AuPdNPs	EIS	10^2 -10^9	59	PBS	48
SWNTs	BPPG	CA	-	0.5	Calf serum	49
SWCNTs	FET	I-V	1- 100	1.37	PBS	50
LIG	Multilayer graphene	DPV	10 -500	5	PBS	This work

*SWNT = single wall carbon nanotubes; GSH-AuNP = Glutathione-protected gold nanoparticles; Ppy = polypyrrole; FC-PPN = ferrocene loaded porous polyelectrolyte; PG = pyrolytic graphite; SPGEs = screen printed graphite electrodes; ERGO-AuPdNPs = reduced graphene oxide and gold–palladium bimetallic nanoparticles; BPPG Basal plane pyrolytic graphene; FET field effect transistor; CA = chronoamperometry; SWV = square wave voltammetry; LSV = linear sweep voltammetry.

In order to further investigate the performance of our biosensor platform towards real world analysis, DPV measurements were performed in PBS containing 10% serum (FBS) and 10% interferent BSA, respectively. The FBS study was carried out because cells grow in vitro in protein media with 10% serum. Besides, FBS contains other nutrients and supplement facilitating cell growth which can potentially affect the binding of IL-6. The BSA interference study was performed as albumin makes up 60% of the total protein found in blood. Figure 3.5a shows a linear decrease in differential current with the log of IL-6 concentration (Log[C]) in the range 10–500 pg/mL. A linear decrease of DPV peak currents with Log[C] was observed, described by the equation $y = -105.0 - 9.2x$ was obtained (y is current in μA; x is log[C], C in g/mL; $R^2 = 0.9738$, Figure 3.4c). Figure 3.5b shows the DPV response of the LIG electrode exposed to 10% BSA interferent concentration. Upon addition of IL-6, decrease of the DPV signal was observed, proving that the sensor maintained its selectivity to IL-6. The linear decrease of DPV peak currents with Log[C] followed the equation $y = -57.10 - 4.6x$ ($R^2 = 0.9745$, Figure 3.5d). In the presence of interferents the modified electrode maintains a characteristic current-Log[C] response. This data demonstrate the high robustness of the IL-6 antibody-modified LIG as a biosensor platform. The calibration of the response is variable and medium-sensitive. This variability is best captured by the changing sensitivity parameter (slope of calibration curve): −6.5 in PBS; −9.2 in 10% serum; −4.6 in 10% BSA. Interestingly, the sensitivity increased in the 10% serum matrix. The usable concentration range has decreased in both cases vs.

PBS—the peak current at 500 pg/mL IL-6 in PBS is higher than at 100 pg/mL in serum and BSA (compare Figure 3.5a, b with Figure 3.3a).

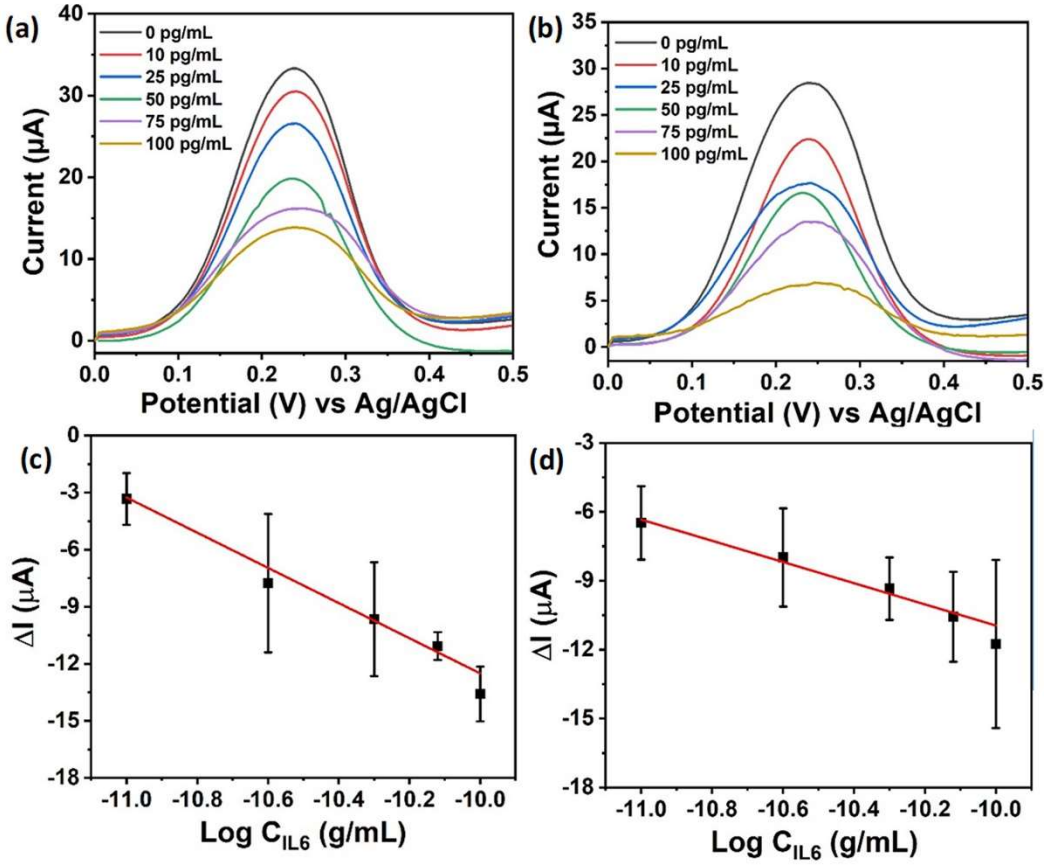


Figure 3.5 DPV curves of LIG biosensor at varying concentrations of IL-6 conducted in 0.1 M PBS at pH 7.4 containing 5 mM $Fe(CN)_6]^{3-/4-}$ in **a)** 10% serum and **b)** 10% BSA; calibration pf DPV peak current with IL-6 concentration in **c)** 10% serum and **d)** 10% BSA, n = 3.

The selectivity of the immunosensor was examined by measuring its electrochemical response (DPV) to interleukin-4 (IL-4), produced mainly by mast cells and involved in immune regulation and wound repair.[44] As the surface of the electrode was modified with antibodies specific for IL-6, no current decrease was detected by DPV upon incubation of the biosensor in PBS containing IL-4 (Figure 3.6).

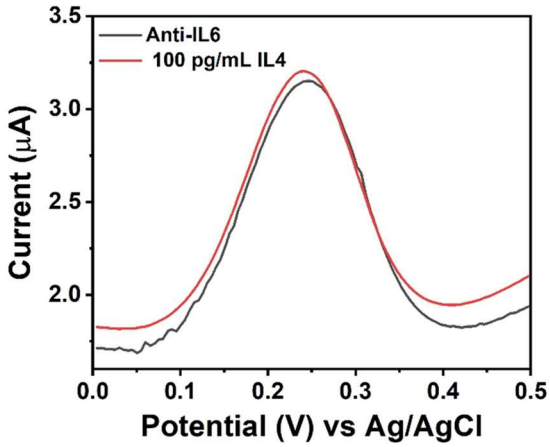


Figure 3.6 DPV curves of LIG biosensor (black curve) and biosensor exposed to 100 pg/mL of IL4 (red curve). DPV conducted in PBS at pH 7.4 containing 5 mM $Fe(CN)_6]^{3-/4-}$.

The stability of shelf life of the developed immunosensors was tested by measuring its current response by DPV after storage in PBS at 4 °C for 6 weeks. The mean change in current calculated for three sensors at IL-6 concentrations of 100 pg/mL was 9.61 μA, very close to the average time zero value of 10.3 μA (Figure 3.7).

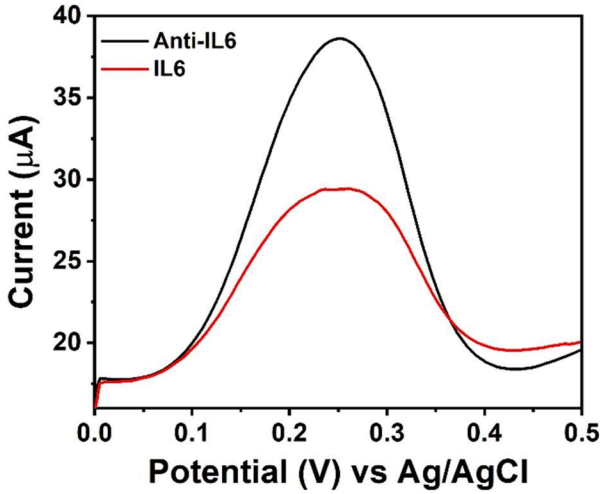


Figure 3.7 DPV curves of bare LIG biosensor (black curve) and biosensor exposed to IL6 10 pg/mL following storage at 4 °C for six weeks (red curve). DPV conducted in PBS at pH 7.4 containing 5 mM $Fe(CN)_6]^{3-/4-}$.

Finally, the immunosensor response was tested with hand-held instrumentation, in order to test the capability of miniaturisation for future point-of-care applications. Figure 3.8a shows the setup used with Bluetooth-operated mobile phone interface. Figure 3.8b shows the DPV curves for the LIG electrode with capture anti-IL-6 and the same electrode exposed to IL-6. Upon exposure to 10 pg/mL IL-6 a decrease in

current, ΔI, equal to −1.6 μA was measured, showing the usability of hand-held instrumentation for point-of-care diagnostic analyses.

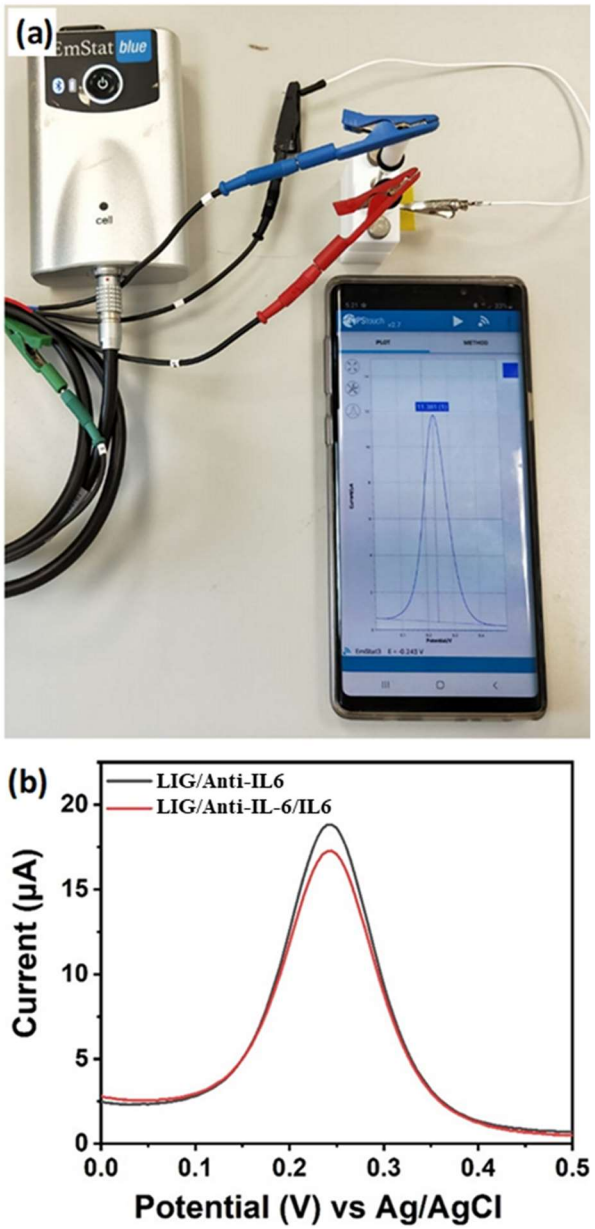


Figure 3.8 a) Photograph of setup used for detection of IL-6 with handheld instrumentation; **b)** DPV curves recorded with handheld instrumentation of 10 pg/mL IL-6 conducted in PBS at pH 7.4 containing 5 mM $Fe(CN)_6]^{3-/4-}$.

3.5 Conclusions

In conclusion, an electrochemical immunosensor for fast and selective detection of inflammatory IL-6 was developed based on the use of bio-modified electrodes. The electrochemical performances were associated with the unique morphology of the electrode, displaying a highly porous, 3D and highly defective structure rich in edge

planes. The immunosensor was able to detect IL-6 in the linear range 10–500 pg/mL with an LOD (n = 3) of 5.1 pg/mL in PBS. The modified electrodes maintained a linear current-Log[C] response in varying media. The high stability over time, selective response, relative fast analysis times, low cost and potential fabrication scalability make this immunosensor suitable for future lab-on-chip diagnostic applications. The compatibility with hand-held commercial instrumentation suggests suitability for point-of-care applications.

Author Contributions: The chapter was a collaborative work with IT Tralee. Pei Shee Tan and I contributed equally to the work presented. I designed and fabricated the electrodes, and performed the electrochemical and Raman characterisation. The electrodes were sent to Pei Shee who performed the bio-modification optimisation steps. Pei Shee performed the experimental immune cell culture and IL6 ELISA. The electrochemical measurements were performed by Pei Shee under guidance (Covid lockdown did not allow for travel). I performed the analysis of the electrochemical results.

3.6 References

1. Stenken, J.A.; Poschenrieder, A.J. Bioanalytical chemistry of cytokines-A review. *Anal. Chim. Acta* **2015**, *53*, 95–115.
2. Liu, G.; Qi, M.; Hutchinson, M.R.; Yang, G.; Goldys, E.M. Recent advances in cytokine detection by immunosensing. *Biosens. Bioelectron.* **2016**, *79*, 810–821.
3. Hénaut, L.; Massy, Z.A. New insights into the key role of interleukin 6 in vascular calcification of chronic kidney disease. *Nephrol. Dial. Transplant.* **2018**, *33*, 543–548.
4. Yoshida, Y.; Tanaka, T. Interleukin 6 and rheumatoid arthritis. *Biomed. Res. Int.* **2014**, *4*, 698313.
5. Kishimoto, T. Interleukin-6: From basic science to medicine—40 years in immunology. *Annu. Rev. Immunol.* **2005**, *23*, 1–21.
6. Yang, T.; Wang, S.; Jin, H.; Bao, W.; Huang, S.M.; Wang, J.C. An electrochemical impedance sensor for the label-free ultrasensitive detection of interleukin-6 antigen. *Sens. Actuat. B* **2013**, *178*, 310–315.

7. Swardfager, W.; Lanctôt, K.; Rothenburg, L.; Wong, A.; Cappell, J.; Herrmann, N. A meta-analysis of cytokines in Alzheimer's disease. *Biol. Psychiatry* **2010**, *68*, 930–941.
8. Smith, P.C.; Hobisch, A.; Lin, D.L.; Culig, Z.; Keller, E.T. Interleukin-6 and prostate cancer progression. *Cytokine Growth Factor Rev.* **2001**, *12*, 33–40.
9. Rusling, J.F.; Kumar, C.V.; Gutkind, J.S.; Patel, V. Measurement of biomarker proteins for point-of-care early detection and monitoring of cancer. *Analyst* **2010**, *135*, 2496–2511.
10. Coomes, E.A.; Haghbayan, H. Interleukin-6 in Covid-19: A systematic review and meta-analysis. *Rev. Med. Virol.* **2020**, *30*, 1–9.
11. Chung, Y.C.; Chaen, Y.L.; Hsu, C.P. Clinical significance of tissue expression of interleukin-6 in colorectal carcinoma. *Anticancer Res*. **2006**, *26*, 3905–3911.
12. Riedel, F.; Zaiss, I.; Herzog, D.; Gotte, K.; Naim, R.; Horman, K. Serum levels of interleukin-6 in 17 patients with primary head and neck squamous cell carcinoma. *Anticancer Res*. **2005**, *25*, 2761–2765.
13. Williams, T.I.; Toups, K.L.; Saggese, D.A.; Kalli, K.R.; Cliby, W.A.; Muddiman, D.C.J. Epithelial ovarian cancer: Disease etiology, treatment, detection, and investigational gene, metabolite, and protein biomarkers. *Proteome Res*. **2007**, *6*, 2936–2962.
14. Kingsmore, F.S. Multiplexed protein measurement: Technologies and applications of protein and antibody arrays. *Nat. Rev. Drug Discov.* **2006**, *5*, 310–320.
15. Yurkovetsky, Z.R.; Kirkwood, J.M.; Edington, H.D.; Marrangoni, A.M.; Velikokhatnaya, L.; Winans, M.T.; Gorelik, E.; Lokshin, A.E. Multiplex Analysis of Serum Cytokines in Melanoma Patients Treated with Interferon-α2b. *Clin. Cancer Res.* **2007**, *13*, 2422–2428.
16. Wang, G.; Hea, X.; Chena, L.; Zhua, Y.; Zhang, X. Ultrasensitive IL-6 electrochemical immunosensor based on Au nanoparticles-graphene-silica biointerface. *Coll. Surf. B Biointerf.* **2014**, *116*, 714–719.
17. Jensen, G.C.; Krause, C.E.; Sotzing, G.A.; Rusling, J.F. Inkjet-printed gold nanoparticle electrochemical arrays on plastic. Application to immunodetection of a cancer biomarker protein. *Phys. Chem. Chem. Phys.* **2011**, *13*, 4888–4894.
18. Tertis, M.; Ciui, B.; Suciu, M.; Sandulescu, R.; Cristea, C. Label-free electrochemical aptasensor based on gold and polypyrrole nanoparticles for interleukin 6 detection. *Electrochim. Acta* **2017**, *258*, 1208–121.
19. Denga, C.; Qub, F.; Sunb, H.; Yang, M. Sensitive electrochemical immunosensor based on enlarged and surface charged gold nanoparticles mediated electron transfer. *Sens. Actuat. B* **2011**, *160*, 471–474.
20. Wang, G.F.; Huang, H.; Zhang, G.; Zhang, X.J.; Fang, B.; Wang, L. Dual amplifica-tion strategy for the fabrication of highly sensitive interleukin-6 amperometric immunosensor based on poly-dopamine. *Langmuir* **2011**, *27*, 1224–123.
21. Khan, M.A.; Mujahid, M. Recent advances in electrochemical and optical biosensors designed for detection of Interleukin 6. *Sensors* **2020**, *20*, 646–673.

22. Tang, L.H.; Wang, Y.; Li, Y.M.; Feng, H.B.; Lu, J.; Li, J.H. Preparation, Structure, and Electrochemical Properties of Reduced Graphene Sheet Films. *Adv. Funct. Mater*. **2009**, *19*, 2782.
23. Zhou, M.; Zhai, Y.; Dong, S. Electrochemical sensing and biosensing platform based on chemically reduced graphene oxide. *Anal. Chem.* **2009**, *81*, 5603.
24. Kang, X.J.; Wang, J.; Wu, H.; Aksay, I.A.; Liu, J.; Lin, Y.H. Glucose Oxidase–graphene–chitosan modified electrode for direct electrochemistry and glucose sensing. *Biosens. Bioelectron*. **2009**, *25*, 901–905.
25. Chen, Z.; Ren, W.; Gao, L.; Liu, B.; Pei, S.; Cheng, H.-M. Three-dimensional flexible and conductive interconnected graphene networks grown by Chemical Vapour Deposition. *Nat. Mater.* **2011**, *10*, 424–428.
26. El-Kady, M.F.; Strong, V.; Dubin, S.; Kaner, R.B. Laser scribing of high-performance and flexible graphene-based electrochemical capacitors. *Science* **2012**, *335*, 1326–1330.
27. Das, S.R.; Nian, Q.; Cargill, A.A.; Hondred, J.A.; Ding, S.; Saei, M.; Cheng, G.J.; Claussen, J.C. 3D Nanostructured inkjet printed graphene: Via UV-pulsed laser irradiation enables paper based electronics and electrochemical devices. *Nanoscale* **2016**, *8*, 15870–15879.
28. Parate, K.; Rangnekar, S.V.; Jing, D.; Mendivelso-Perez, D.L.; Ding, S.; Secor, E.B.; Smith, E.A.; Hostetter, J.M.; Hersam, M.C.; Claussen, J.C. Aerosol-jet-printed graphene immunosensor for label-free cytokine monitoring in serum. *ACS Appl. Mater. Interf.* **2020**, *12*, 8592–8603.
29. Secor, E.B.; Prabhumirashi, P.L.; Puntambekar, K.; Geier, M.L.; Hersam, M.C. Inkjet printing of high conductivity, flexible graphene patterns. *J. Phys. Chem. Lett.* **2013**, *4*, 1347–1351.
30. Ye, R.; James, D.K.; Tour, J.M. Laser-induced graphene. *Acc. Chem. Res.* **2018**, *51*, 1609–1920.
31. Lin, J.; Peng, Z.; Liu, Y.; Zepeda, F.; Ye, R.; Samuel, E.L.G.; Yacamn, M.J.; Yakobson, B.I.; Tour, J.M. Laser-induced graphene films from commercial polymers. *Nat. Commun*. **2014**, *5*, 5714.
32. Nayak, P.; Kurra, N.; Xia, C.; Alshareef, H. Highly efficient laser scribed graphene electrodes for on-chip electrochemical sensing applications. *Adv. Electron. Mater*. **2016**, *2*, 1600185.
33. Vaughan, E.; Larrigy, C.; Burke, M.; Sygellou, L.; Quinn, A.J.; Galiotis, C.; Iacopino, D. 2020. Visible laser scribing fabrication of porous graphitic carbon electrodes: Morphology, electrochemical properties and applications as disposable sensor platform. *ACS Appl. Electron. Mater*. **2016**, *2*, 3279–3288.
34. Prabhakaran, A.; Nayak, P. Surface engineering of laser-scribed graphene sensor enables non-enzymatic glucose detection in human body fluids. *ACS Appl. Nano Mater*. **2020**, *3*, 391–398.
35. Vanegas, D.; Patiño, L.; Mendez, C.; Oliveira, D.; Torres, A.; Gomes, C.; McLamore, E. Laser scribed graphene biosensor for detection of biogenic amines in food samples using locally sourced materials. *Biosensors* **2018**, *8*, 42–61.
36. Cardoso, A.R.; Marques, A.C.; Santos, L.; Carvalho, A.F.; Costa, F.M.; Martins, R.; Sales, M.G.F.; Fortunato, E. Molecularly imprinted chloramphenicol sensor

with laser-induced graphene electrodes. *Biosens. Bioelectron*. **2019**, *124–125*, 167−175.
37. Soares, R.R.A.; Hjort, R.G.; Pola, C.C.; Parate, K.; Reis, E.L.; Soares, N.F.F.; McLamore, E.S.; Claussen, J.C.; Gomes, C.L. Laser-Induced Graphene Electrochemical Immunosensors for Rapid and Label-Free Monitoring of Salmonella enterica in Chicken Broth. *ACS Sens.* **2020**, *5*, 1900–1911.
38. Fenzl, C.; Nayak, P.; Hirsch, T.; Wolfbeis, O.S.; Alshareef, H.N.; Baeumner, A.J. Laser-scribed graphene electrodes for aptamer-based biosensing. *ACS Sens*. **2017**, *2*, 616–620.
39. Rauf, S.; Lahcen, A.A.; Aljedaibi, A.; Beduk, T.; de Oliveira Filho, J.I.; Salama, K.N. Gold nanostructured laser-scribed graphene: A new electrochemical biosensing platform for potential point-of-care testing of disease biomarkers. *Biosens. Bioelectr*. **2021**, *180*, 113116.
40. Burke, M.; Larrigy, C.; Vaughan, E.; Paterakis, G.; Sygellou, L.; Quinn, A.J.; Herzog, G.; Galiotis, C.; Iacopino, D. Fabrication and electrochemical properties of three dimensional porous graphitic electrodes obtained by low-cost laser induced graphene (LIG). *ACS Omega* **2020**, *5*, 1540–1548.
41. Nicholson, R.S. Theory and application of cyclic voltammetry for measurement of electrode kinetics. *Anal. Chem*. **1965**, *37*, 1351–1355.
42. Bard, A.J.; Faulkner, L.R. *Electrochemical Methods*, 2nd ed.; John Wiley & Sons: New York, NY, USA, 2010.
43. Zhang, X.; Gao, F.; Cai, X.; Zheng, M.; Gao, F.; Jiang, S.; Wang, Q. Application of graphene–pyrenebutyric acid nanocomposite as probe oligonucleotide immobilization platform in a DNA biosensor. *Mater.Sci. Engineer. C* **2013**, *33*, 3851–3857.
44. Ul-Haqa, Z.; Naza, S.; Mesaik, A. Interleukin-4 receptor signaling and its binding mechanism: A therapeutic insight from inhibitors tool box. *Cyt. Gro. Fact. Rev.* **2016**, *32*, 3–15.
45. Munge, B.S.; Krause, C.E.; Malhotra, R.; Patel, V.; Rusling, J.F. Electrochemical immunosensors for interleukin-6. Comparison of carbon nanotube forest and gold nanoparticle platforms. *Electrochem. Commun*. **2009**, *11*, 1009–1012.
46. Li, T.; Yang, M. Electrochemical sensor utilizing ferrocene loaded porous polyelectrolyte nanoparticles as label for the detection of protein biomarker IL-6. *Sensor. Actuat. B* **2011**, *158*, 361–365.
47. Chikkaveeraiah, B.V.; Bhirde, A.; Malhotra, R.; Patel, V.; Gutkind, J.S.; Rusling, J.F. Single-wall carbon nanotube forest arrays for immunoelectrochemical measurement of four protein biomarkers for prostate cancer. *Anal. Chem.* **2009**, *81*, 9129–9134.
48. Lou, Y.; He, T.; Jiang, F.; Shi, J.-J.; Zhu, J.-J. A competitive electrochemical immunosensor for the detection of human interleukin-6 based on the electrically heated carbon electrode and silver nanoparticles functionalized labels. *Talanta* **2014**, *122*, 135–139.
49. Malhotra, R.; Patel, V.; Vaque´, J.P.; Gutkind, J.S.; Rusling, J.F. Ultrasensitive electrochemical immunosensor for oral cancer biomarker IL-6 using carbon nanotube forest electrodes and multilabel amplification. *Anal. Chem*. **2010**, *82*, 3118–3123.

50. Chen, H.; Choo, T.C.; Huan, J.; Wang, Y.; Liu, Y.; Platt, M.; Palaniappan, A.; Liedberg, B.; Tok, A.L.Y. Label-free electronic detection of interleukin-6 using horizontally aligned carbon nanotubes. *Mater. Des.* **2016**, *90*, 852–857.
51. Said EA, Al-Reesi I, Al-Shizawi N, Jaju S, Al-Balushi MS, Koh CY, Al-Jabri AA, Jeyaseelan L. Defining IL-6 levels in healthy individuals: A meta-analysis. J Med Virol. 2021 Jun;93(6):3915-3924. doi: 10.1002/jmv.26654
52. Herold T, Jurinovic V, Arnreich C, Lipworth BJ, Hellmuth JC, von Bergwelt-Baildon M, Klein M, Weinberger T. Elevated levels of IL-6 and CRP predict the need for mechanical ventilation in COVID-19. J Allergy Clin Immunol. 2020 Jul;146(1):128-136.e4. doi: 10.1016/j.jaci.2020.05.008.

Chapter 4: Direct Laser Writing of Chitosan-Borax Composites: Towards Sustainable Electrochemical Sensors

4.1 Abstract

In this chapter the laser-induced graphitisation process of sustainable chitosan-based formulations was investigated. In particular, optimal lasing conditions was investigated alongside the effect of borax concentration in the chitosan matrix. In all cases, it was found that obtained formulations were graphitisable with a CO_2 laser. This process gave rise to the formation of high surface area, porous, and electrically conductive laser-induced graphene (LIG) structures. It was found that borax, as cross-linker of chitosan, enabled the graphitisation process when its content was ≥ 30 wt% in the chitosan matrix, allowing the formation of a LIG phase with a significant content of graphite-like structures. The graphitisation process was investigated by Raman, TGA, XPS and FTIR spectroscopies. LIG electrodes obtained from CS/40B formulations displayed sheet resistance as low as 110 Ω/sq. Electrochemical characterisation gave a heterogeneous electron transfer rate, k^0, of 4 x 10^{-3} cm s^{-1}, indicating rapid electron transfer rates at the electrode surface. These results show promise for the introduction of a new class of sustainable composites for LIG electrochemical sensing platforms.

4.2 Introduction

Graphene is a material with renowned physical and electrical properties.[1] Graphene and graphene-like materials are used in areas such as electronics, electrochemical sensing, strain sensors, energy storage, catalysis and more.[2-6] The fabrication of graphene by standard methods such as chemical vapour deposition, liquid-phase exfoliation, or micromechanical exfoliation present challenges relating to achieving a cost-effective and time-effective procedure suitable for commercialisation.[7] Therefore, alternative fabrication methods such as the use of a laser to reduce graphene oxide, creating graphene-like surface features, have been explored for more than a decade.[8-10] Recently, direct laser writing protocols have been developed and systematically applied for the conversion of commercial polymers to a high quality graphene-like material.[11] Specifically, in 2014 Lin *et al.* obtained a graphene-like material, termed Laser-Induced Graphene (LIG), by direct laser writing of a commercial Kapton tape (polyimide) with a CO_2 laser. LIG is a porous, 3D structure, characterised by a high surface area, resulting from the generation of gases during the lasing process.[12] The LIG morphology, and hence its surface properties, can be tuned by controlling the laser parameters such as power, speed and laser wavelength.[13] LIG has been shown to be an excellent material for applications such as electrochemical sensing, energy storage, humidity sensing and biosensing, among others.[14-20]

Considering the extensive research currently being conducted into LIG-based devices and their wide range of applications, the sustainability of such a materials must be considered.[21, 22] In this scenario, it is worth considering alternatives to fossil-fuel

derived polymers as precursor materials for LIG production. Although the detailed mechanism of laser-induced polymer graphitisation is still not fully clear, it is known that LIG formation results from a combination of photothermal and photochemical processes, highly favoured in Kapton by the aromatic structure of polyimide.[23] In recent years various natural materials, such as wood, paper, leaves, coal, cloth, and cork have been used as LIG precursor substrates alternative to polyimide[15, 24-28] and applications of the resulting "green" LIG structures have ranged from electrochemical sensors to supercapacitors. Natural materials are converted to LIG based on the same principles as polyimide conversion: adsorption of radiation, local increase of temperature, cleavage of C-C, C-O, and C-H bonds and reorganisation and polymerisation of the aromatic structures into graphene-like structures.[29] Recently, attention has been given also to biopolymer materials, in an attempt to widen the range of graphitisable materials. For example, Larrigy *et al.* have successfully graphitised chitosan films using a multi-pass laser conversion technique, based on a combination of a CO_2 and a 405 nm lasers[30]. The resulting LIG showed a porous morphology with low sheet resistance, below 40 Ω/sq, suitable for electrochemical sensing applications. Huang *et al.* converted eco-friendly chitosan-based derivatives into LIG with a one-step CO_2 laser engraving in ambient air.[31] Low sheet resistances of 12.7 Ω/sq were achieved with chitosan hydrochloride-based sheets; however, these films were too prone to deformation or cracking to be used as devices. Instead, carboxymethyl chitosan-based films, with sheet resistances of 2.2 kΩ/sq, showed suitability for eco-friendly electronics in the form of triboelectric nanogenerators. The introduction of chitosan into the range of natural LIG precursor materials is an important development, due to its natural abundance, biocompatibility, biodegradability, nontoxicity, chemical stability, and high reactivity.[32] However, despite the above attractive properties,

chitosan exhibits low chemical stability in wet environments, which limits its application fields.[32] Sodium tetraborate decahydrate (borax) has been recently investigated as crosslinking agent to improve chitosan's mechanical and water barrier properties.[32, 33] Specifically, it has been found that the esterification reaction between borate ions and the hydroxyl moieties of chitosan creates a composite structure denser than pristine chitosan, resulting in increased water and gas barrier properties.[34] Moreover, incorporation of boron into cellulose-based materials (cotton, wood and paper) has been shown to exhibit effective flame retardant properties, leading to improved Limiting Oxygen Index (LOI) values, reduced peak Heat Release Rate (pHRR) and reduced smoke release.[34, 35] In particular, when mixed to polymer matrices, borax provided a glass-like coating on the fire-exposed surface and promoted the formation of char, which is well known to consist of amorphous carbon as well as graphite-like structures, according to different high temperature conditions.[36, 37] Coelho *et al.* and separately Pinheiro *et al.* have shown that Borax-treated chromatography paper can be converted to LIG structures, with electrochemical sensing and microsupercapacitor applications respectively.[38, 39] The role of borax is elucidated by a comparison with laser-treated raw chromatography paper. While the borax treatment allows the paper withstand the photothermal degradation process, leading to LIG formation, the raw sample is completely ablated by the laser.

In this chapter, we introduced borax as crosslinker of chitosan and investigated the graphitisation properties of the resulting formulations by use of infrared laser sources. Different concentrations of borax were used and it was found that a percentage > 30% (wt, with respect to CS content) was effective in producing formulations graphitisable by one or two laser passes. The obtained LIG structures displayed high porosity, 3D morphology and low sheet resistance. The potential use of this LIG material as

electrochemical sensor was investigated. It was found that LIG displayed a high heterogeneous electron transfer rate, comparable to the value found in other green LIG materials, indicating rapid electron transfer rates at the electrode surface. These results show promise for the introduction of a new class of sustainable formulations as LIG feedstock for the development of sustainable electrochemical sensing platforms.

4.3 Experimental Section

4.3.1 Materials

Medium molecular weight chitosan powder was purchased from Sigma Aldrich. Gluconic acid δ-lactone (GDL) and sodium tetraborate decahydrate (borax) were supplied from Sigma-Aldrich (Italy). All solutions were prepared using deionised Milli-Q water (resistivity 18.2 MΩ.cm).

4.3.2 CS-based Films Preparation

Chitosan (CS) powder was dissolved in D-(+)-Gluconic acid δ-lactone (GDL) aqueous solution at room temperature to prepare 20 mg mL^{-1} of CS solution. Then borax aqueous solution was added under stirring. The borax (B) concentration was varied to obtain a final content equal to 20, 30, 40 and 60 wt% with respect to the CS weight. Subsequently, the solution was poured into a glass plate and air-dried to allow solvent removal. The thickness of the obtained films was of about 100 μm, measured by micrometer screw gauge. CS-based films were coded CS/xB, where x represent the weight percentage of borax.

4.3.3 LIG Fabrication

LIG structures were fabricated by direct laser writing of CS/xB films with a CO_2 laser engraver (10.6 μm wavelength, 30 W power, HQ-3020B, GuangZ-hou Amonstar

Trade Co., Ltd.). Laser power was varied between 8-15% (for higher powers complete ablation of the material occurred), Laser speed was varied between 10-40%. In cases of combinations of low power and high speed, features were overlapped (written once, then again in the same spot, indicated by "×2" in the 'Laser settings' column of Table S1) to investigate the effect of multiple laser passes. Conditions were sought which produced an undamaged, black feature – indicating the formation of LIG.

4.3.4 Characterisation

Surface morphology was analysed using Zeiss Supra Scanning Electron Microscope (SEM) equipped with an Oxford X-Max 50 detector operating at an accelerating voltage of 10kV. Bright field transmission electron microscopy (TEM) analysis was performed by means of a FEI Tecnai G12 Spirit Twin (LaB6 source) at 120 kV acceleration voltage. TEM images were collected on a FEI Eagle 4 k CCD camera. Raman investigation was performed with a Renishaw inVia Raman system equipped with a 514 nm argon-ion laser. The focusing of the laser beam onto the sample was obtained through a Leica 20X objective with 0.4 N.A. Spectra were acquired at a laser power of 3 mW and acquisition time of 10 s. Attenuated Total Reflection-Fourier Transform Infrared (ATR-FTIR) analysis was carried out with a portable Bruker ALPHA II's Platinum ATR single reflection diamond ATR. X-ray photoemission (XPS) spectra was collected by using an Escalab 250Xi (Thermo Fisher Scientific, UK) spectrometer, equipped with a monochromatic Al Kα excitation source, electron and ion flood guns for charge neutralisation and a 6-channeltron detection system. The photoemission spectra were collected at 20 eV pass energy, and the diameter of analysed area was about 1 mm.

Thermal degradation of materials was evaluated by thermo-gravimetric analysis (TGA) that was carried out in N_2 flow (flow rate of 40 ml/min) using a TGAQ500-TA

Instruments, at a heating rate of 10°C/min in the temperature range from 35°C to 1000°C.

Initial estimations of sheet resistance were made by using a multimeter to measure the resistance across 3 x 9 mm features. For CS/B40 and CS/B60 samples, two-terminal current−voltage measurements (±1 V, 20 mV step) were obtained under ambient conditions on transmission line method (TLM) structures using an Wentworth PML 8000 probe station and Agilent E4980A parameter analyser. Track resistance values for varying channel lengths were calculated from linear fits of I-V plots. Plots of track resistance versus channel length were used to calculate sheet resistance (R_{SH}).

4.3.5 Electrochemical measurements

Electrochemical measurements were recorded using a CHI760 bi-potentiostat. A three electrode set-up was used, with Ag/AgCl as the reference electrode and a Pt wire as the counter electrode. LIG was used as the working electrode. An electrode measuring 3 x 10 mm was scribed, and the surface was passivated using polyimide tape to reduce the active surface area to approximately 3 x 3 mm (see Figure 4.7a). The measurements were made in a Teflon electrochemical cell with the working electrode at the base. A 10 min electrochemical cleaning cycle was performed using 1 M KCl, in which the potential was varied between -1.6 V and 0.8 V at a scan rate of 200 mV/s for 25 cycles. Afterwards, 5 mM $[Fe(CN)_6]^{3-/4-}$ was used for a standard electrode characterisation. The calculation of the heterogeneous electron transfer (HET) rate constant (k^0) for $[Fe(CN)_6]^{3-/4-}$ was performed using the method of Nicholson by assuming a transfer coefficient $\alpha = 0.5$ and using the following diffusion coefficients: $D_O = 7.63 \times 10^{-6}$ cm^2 s^{-1}, $D_R = 6.32 \times 10^{-6}$ cm^{2}s^{-1}.[40]

4.4 Results and discussion

4.4.1 Material optimisation

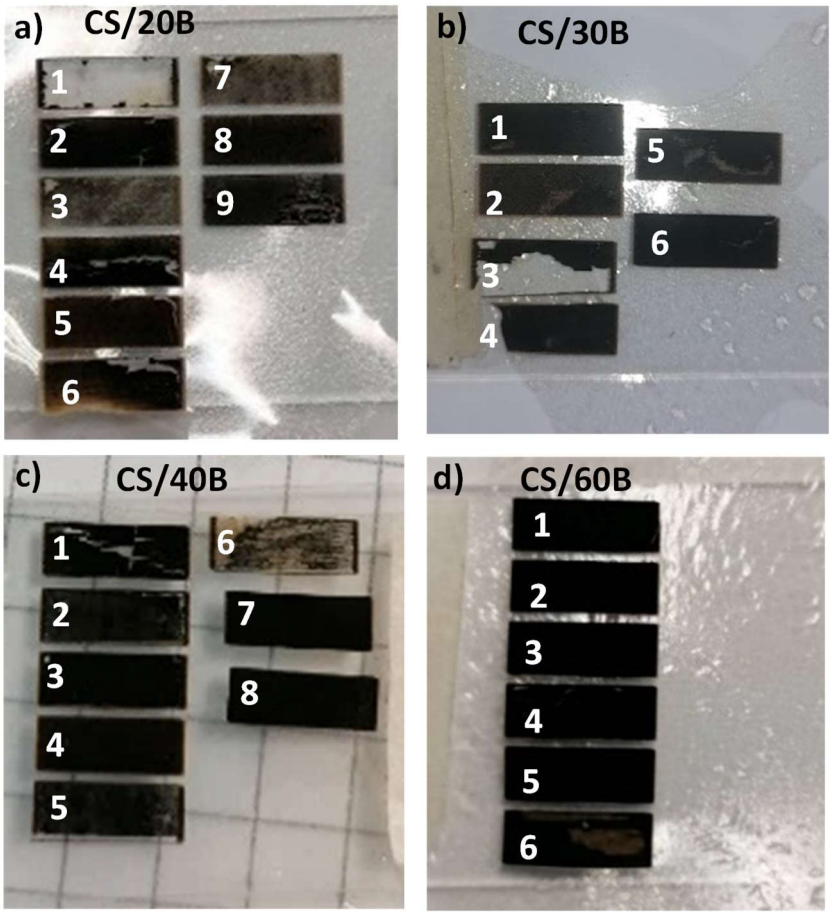


Figure 4.1 Effect of lasing of CS/xB films by various laser parameters.

Figure 4.1 shows photographs of the CS/xB structures obtained at various laser power (LP) and laser speed (LS) values. Initial selection of optimal laser writing parameters optimisation was determined by choosing the conditions that produced features with the highest conductivity. Figure 4.1 shows that the formation of LIG depended on the laser parameters as well as on the content of borax. In details, Figure 4.1a shows that for CS/20B formulations, ablation and crack formation occurred for the majority of LP-LS combinations, preventing formation of fully graphitised and low resistance features. Only one experimental writing condition (LP-LS 10-30 and two overlapped laser passes) led to formation of LIG features, albeit with high R_{sh} > 1 kΩ/sq. An

improvement in the graphitisation process was observed in Figure 4.1b, where the borax content was increased to 30 wt%. Graphitised structures with R_{sh} of about 500 Ω/sq were formed using the combination LP-LS 10-20 and two overlapped laser passes. Figure 4.1c shows photographs of the features obtained by laser writing of CS/40B formulations, which had the required properties to allow graphitisation with a range of laser settings, with low R_{sh} values reported for LP-LS 10-20 and two overlapped laser passes. Similarly, CS/60B formulations enabled LIG formation over a range of laser settings, as shown in Figure 4.1d.

TLM measurements were performed on both CS/40B- and CS/60B-LIG samples, as shown in Figure 4.2. For these TLM structures, 2 x 20 mm (10 squares) LIG features were scribed, with measurements taken at track lengths L1 = 4 mm, L2= 8 mm, L3 = 12 mm, L4 = 16 mm, L5 = 20 mm, beginning with the largest separation to avoid damaging the track between terminals for proceeding measurements. A square (S) is defined simply as a feature with length equal to width, and the number of squares is the track length divided by the width. The track resistance (Ri) between two consecutive pads could then be related to the number of squares via

$$Ri = Rc + (Rs)(S)$$

where Rc is the contact resistance, Rs is the sheet resistance of the sample. Values for Rs were thus obtained from linear regression of Ri versus S, as shown in Figure 4.2. The value for CS/40B-LIG was 110 ± 1 Ω sq^{-1}, and 341 ± 6 Ω sq^{-1} for CS/60B-LIG. TLM measurements were not taken for CS/30B, as the material could not support the required features.

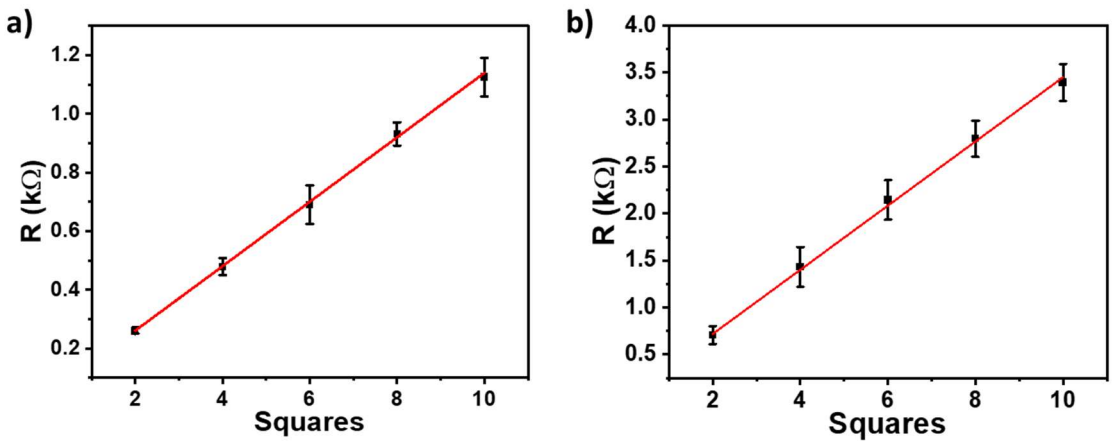


Figure 4.2 TLM measurements for **a)** CS/40B-LIG and **b)** CS/60B-LIG. Both LIG formations were at laser power 10% and speed 20%, with two overlapped laser passes.

Overall, these results suggest that increasing the borax content improves capacity of material to withstand the high temperature conditions necessary for the formation of LIG, since graphitisation of pure CS films with no Borax content did not occur under any laser experimental conditions (data not shown).

CS/xB-LIG Characterisation

To investigate the surface morphology, CS/xB-LIG features were examined by scanning electron microscopy (SEM). The SEM images shown in Figure 4.3 (a – h) confirm that all samples displayed the porous, exploded structure associated with LIG formation. This is a result of the laser impinging on the biopolymer substrate in presence of atmospheric oxygen. Similar to what has been reported for laser writing of polyimide and other natural substrates, we speculate that the laser irradiation created a local high-temperature and high-pressure environment, leading to the breaking of the CS's C-O, C=O, and C-N bonds, and to formation of high-pressure gas pockets that drove the generation of micro and nanopores, along with other structural defects.[14, 41-43] In general, high magnification SEM images (Figure 4.3b, d, f, h) showed formation of a dense and 3D graphitic network, with micro-holes and tears of different diameter on the LIG surface. Low magnification images (Figure 4.3a, c, e, g) displayed the typical peaks and valleys associated to the raster scanning movement of the laser. For

comparison, Figure 4.3i shows the SEM image of a pristine CS/40B film prior to graphitisation, which was characterised by a smooth surface. Figure 4.3j shows a 45° angle tilted SEM image of a graphitised CS/40B sample, showing LIG formation of about 35 μm thickness.

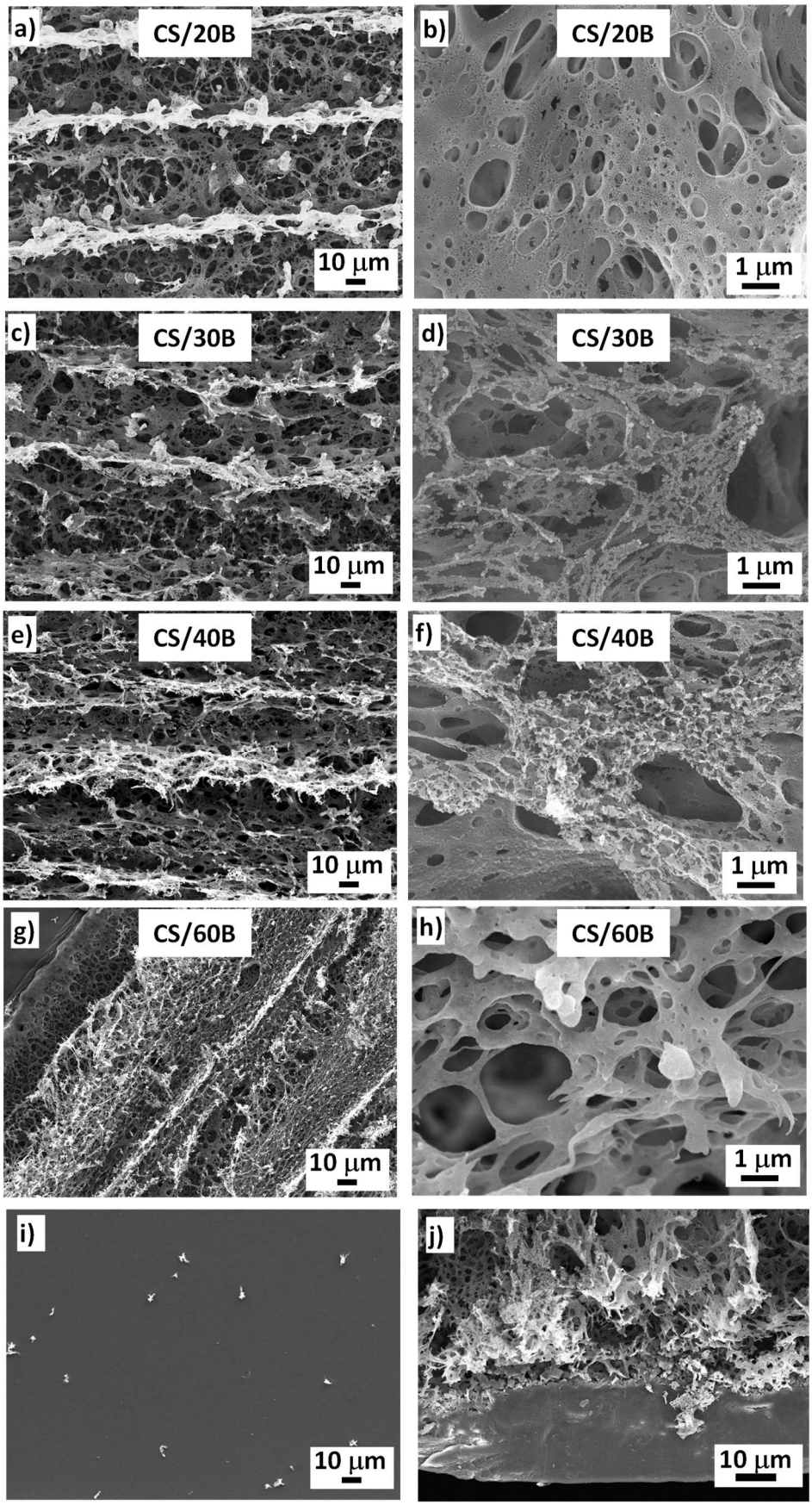


Figure 4.3 SEM images showing the process of laser graphitisation on the CS/xB systems. Low magnification SEM images of graphitised **a)** CS/20B; **c)** CS/30B; **e)** CS/40B; **g)** CS/60B.

High magnification SEM images of **b)** CS/20B; **d)** CS/30B; **f)** CS/40B; **h)** CS/60B; **i)** SEM image of pristine CS/40B; **j)** tilted SEM image of graphitised CS/40B.

Figure 4.4 shows representative Raman spectra for LIG structures obtained from CS/xB formulations. For CS/20B, Raman investigation confirmed the incomplete graphitisation as spectra were either featureless or characterised by broad D, G and 2D peaks, highlighting an inhomogeneous distribution of graphene-like structures. Of the 17 spectra that were recorded: 10 showed no peaks; 3 showed weak and broad D and G peaks; 4 spectra showed broad D, G and 2D peaks. Examples of shown in Figure 4.4a.

For borax concentrations 30 wt% and higher each Raman spectrum showed well resolved peaks, characteristic of graphene-like carbon structures: a D mode peak, assigned to a defect-activated radial breathing mode, centred close to 1350 cm^{-1}; a G mode peak, related to in-plane bond stretching of pairs of sp^2 carbon atoms, centred around 1584 cm^{-1}; a 2D mode, the second order overtone of the D peak, centred around 2696 cm^{-1} (Figure 4.4b).[44] A D' peak was also fitted around 1618 cm^{-1}, evident in the asymmetry of the G-peak, and associated with the formation of high quality polycrystalline graphite or creation of defects in natural graphite single crystals.[45, 46] A D + D', appeared around 2940 cm^{-1} in the higher quality spectra. The formation of D and D+D' bands is associated to the formation of graphene-like materials with significant defects originating from the intravalley double resonance and a combination mode, respectively.[47]

Peaks were fitted by a single Lorentzian curve. Twenty spectra were collected per LIG sample, with the average fitting results displayed in Table 4.1. The FWHM of both G, D, and 2D modes showed little variation across samples (minimum for CS/30B), with all values remaining below 100 cm^{-1}. These sharp peaks suggest a high degree of crystallinity, and the FWHM values are in line with high quality LIG

produced on polyimide.[14]. The I_D/I_G peak ratio was equal to 1 for CS/30B, and only slightly increased for borax amounts > 30 wt%, suggesting a low defect density. This result confirmed the nature of the LIG material, in agreement with the formation of highly ordered nanocrystalline graphitic domains in a disordered carbon matrix.[48] The relative intensity of the 2D peak also reached a maximum for the CS/30B formulation and then slowly decreased for higher boron concentrations. In parallel, the FWHM of the 2D peak reached a minimum for the CS/30B formulation and then slowly increased for higher boron content. The presence of sharp 2D peaks provided further evidence for a higher degree of ordering, consisting of randomly stacked graphene layers along the c axis,[11] with highest order observed for CS/30B and CS/40B structures. The high I_{2D}/I_G ratio indicated a low number of graphene layers.[11, 48]

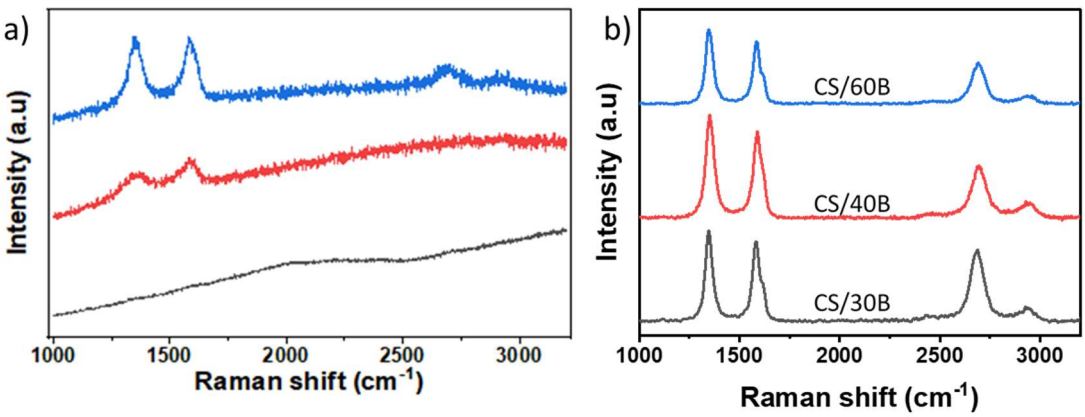


Figure 4.4 a) Three types of Raman spectra recorded for CS/20B sample: featureless (black; 10/17); weak, broad D and G peaks (red; 3/17); weak, broad D, G and 2D peaks (blue; 4/17); **b)** Representative Raman spectra of LIG structures obtained from direct laser writing of CS/xB biopolymer substrates.

Table 4.1 Raman characteristics of LIG structures obtained from direct laser writing of CS/xB formulation substrates. Error reported is standard deviation of 20 spectra. No error values reported for standard deviation less than 0.5 cm^{-1}.

Sample	$FWHM_D$ (cm^{-1})	$FWHM_G$ (cm^{-1})	$FWHM_{2D}$ (cm^{-1})	$I_{D/G}$	$I_{2D/G}$
CS/30B	41	38	69 ± 3	1.0 ± 0.1	0.8 ± 0.1
CS/40B	45 ± 1	39 ± 1	82 ± 2	1.2 ± 0.2	0.5 ± 0.1
CS/60B	49 ± 1	45 ± 1	84 ± 3	1.3 ± 0.1	0.5 ± 0.1

The CS/40B formulation was selected as optimal for further investigation and characterisation, as it was easily graphitisable, and combined excellent Raman characteristics with the lowest sheet resistance.

4.4.2 CS/40B-LIG Characterisation

Figure 4.5a shows a TEM image of a CS/40B-LIG structure displaying crystalline domains, better evidenced in the high magnification inset, embedded in an amorphous matrix. The high magnification TEM image (Figure 4.5a, inset) revealed the formation of multilayer structures, constituted by stacked graphene sheets, as well as nanoscale edges, ripples and wrinkles, in agreement with morphology of LIG samples obtained from other polymer and biopolymer matrices.[30] The calculated interlayer spacing was 3.5 Å (± 0.1), which is similar to values determined for LIG on polyimide, wood and cork.[11, 15, 24] Moreover, there is no morphological evidence of a separated borax phase, indicating that borax is incorporated and homogeneously distributed in the LIG structure.

Figure 4.5b shows the thermal stability of CS/40B films compared to CS film, evaluated by TGA analysis. The TGA curves presented different mass loss zones that were better highlighted in the corresponding DTA curves shown as inset of Figure 4.5b. The results show that the CS weight loss took place in two stages. The first one in the region of 60°C to 160°C, with a maximum temperature (Td_1) of 116°C, was mainly ascribed to water evaporation. The second stage from 160°C to 400°C (two overlapping steps), with a maximum degradation temperature (Td_2) of 288°, was attributed to the pyrolysis of the polysaccharide that presumably started by a random split of the glycosidic bonds, followed by a further decomposition forming predominantly acetic, propionic and butyric acids.[49] In the case of CS/40B films the water loss occurred by a different mechanism compared to bare CS formulations, due

to the presence of borax which can bind to water molecules, leading to stronger polymer-water interactions.[50] Moreover, due to the crosslinking between borax and the chitosan hydroxyl groups the second stage of degradation showed a Td_2 value of 309°C, which was 21°C higher than the Td_2 of the bare CS sample. This temperature shift is probably due to a reduction of the concentration and availability of reactive OH groups in the CS/40B sample. At temperature lower than 400 °C the anhydrous CS/40B sample converts to aliphatic char, which in turn at higher temperatures (≥ 400 °C) can give rise to cyclisation, decarboxylation, decarbonylation, and cross-linking reactions, leading to the formation of aromatic char. It is also important to note that crosslinking of CS with borax increased the residual weight at 800 °C. A residual weight of 29% and 37% was found for CS and CS/40B films, respectively. These results highlight the ability of borax to promote the generation of char components.[32]

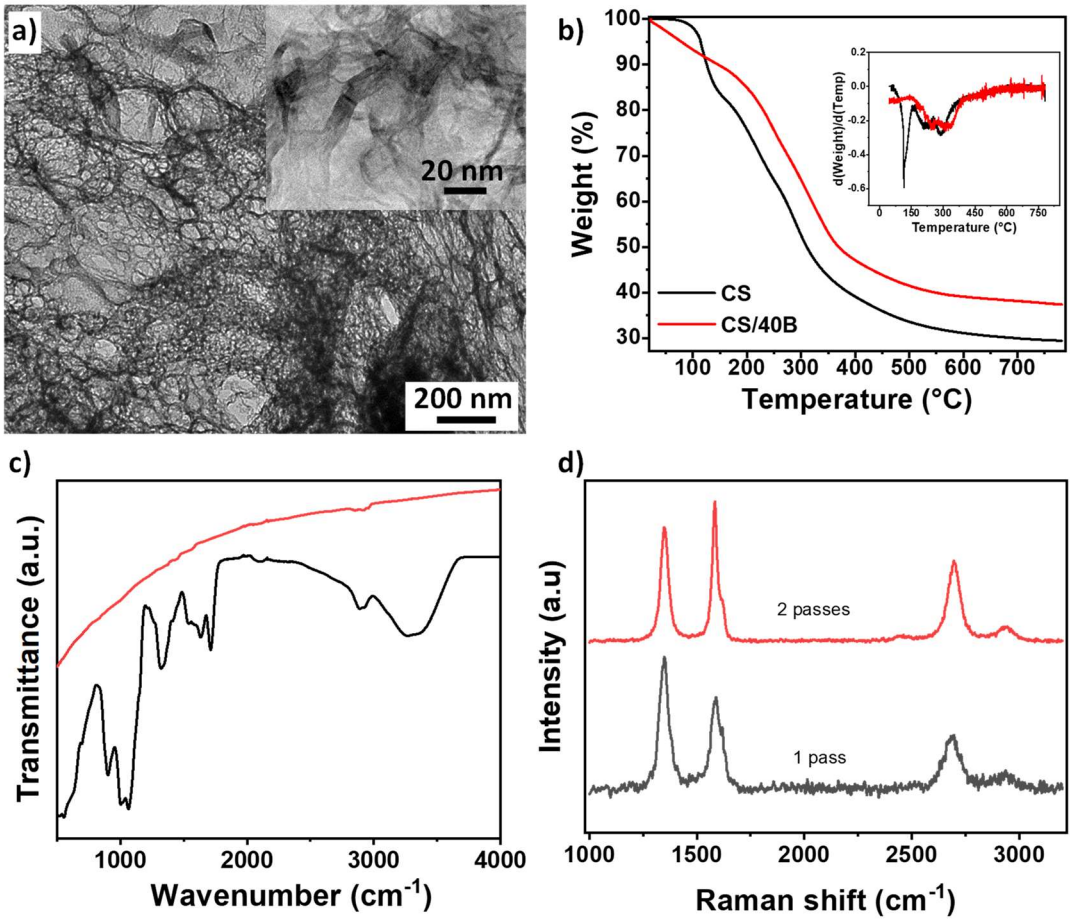


Figure 4.5 a) TEM image of LIG structure obtained from laser writing of CS/40B; **b)** TGA analysis of CS and CS/40B films. Inset: DTGA curves; **c)** FTIR spectra of pristine CS/40B film (black line) and CS/40B-LIG structure (red line); **d)** Raman spectra after first and second laser pass.

The process of LIG formation was analysed further by spectroscopic characterisation. Figure 4.5c shows ATR-FTIR spectra taken before and after graphitisation. The as-fabricated chitosan film showed bands in good agreement with published work on chitosan films.[30, 51-54] In the high wavenumber region of the spectrum (>2600 cm^{-1}) displayed common features: the band peaking at 3300 cm^{-1} caused by O-H stretching vibrations convoluted with N-H stretching; the band with a peak at 2890 cm^{-1} associated to C-H stretching vibrations. Such stretching vibrations are typical for polysaccharide molecules.[55] The presence of residual N-acetyl groups was confirmed by the presence of bands at 1636 cm^{-1} (C=C stretching of amide I) and 1535 cm^{-1} (N-H bending of amide II), respectively. The absorption peaks at 1064 and 896 cm^{-1} were ascribed to the anti-symmetric stretching vibration of C–O–C bridges

and glucopyranose ring in the chitosan matrix, suggesting an interaction between the glucopyranose ring in the chitosan matrix and borax.[56] In contrast, the FTIR spectrum of CS/40B-LIG was featureless, as expected for the conversion to graphitic and amorphous carbon.[15]

A more detailed analysis of the two-step graphitisation process was performed by monitoring the change in Raman spectra between the first and second laser pass. The results are displayed in Figure 4.5d. The progression to a more ordered graphene-like material was clearly seen with the application of a second laser pass as the FWHM of all peaks decreased; the D peak intensity decreased while the G peak and 2D peak intensities increased. Moreover, the I_{2D}/I_G increased from 0.4 to 0.5, while the I_D/I_G ratio decreased from 1.5 to 1.2 indicating the progression to a higher degree of ordering in the sample.

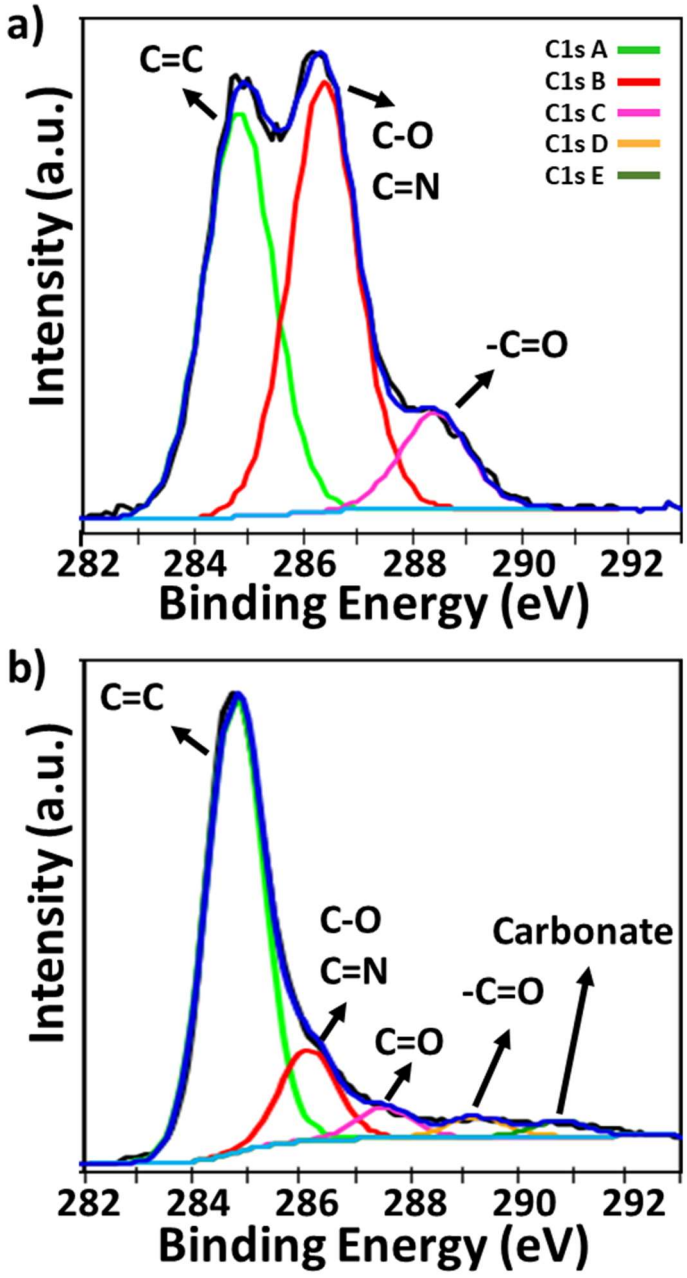


Figure 4.6 Deconvoluted XPS C1S spectra of **a)** pristine CS/40B film and **b)** graphitised CS/40B.

Figure 4.6 shows the deconvoluted C1s XPS spectra for the pristine CS/40B formulation and the CS/40B-LIG. The graphitised sample was dominated by a large C1s A peak, representing C=C sp^2 bonds. Other peaks have been labelled C1s B (C-C), C (C-OH, -C-O), D (C=O), and E (carbonate). Peak assignments and percentage component concentrations are shown in Table 4.2. An increase in the percentage of C=C carbon (graphene or graphite) was observed, from 26.4% for untreated CS/40B

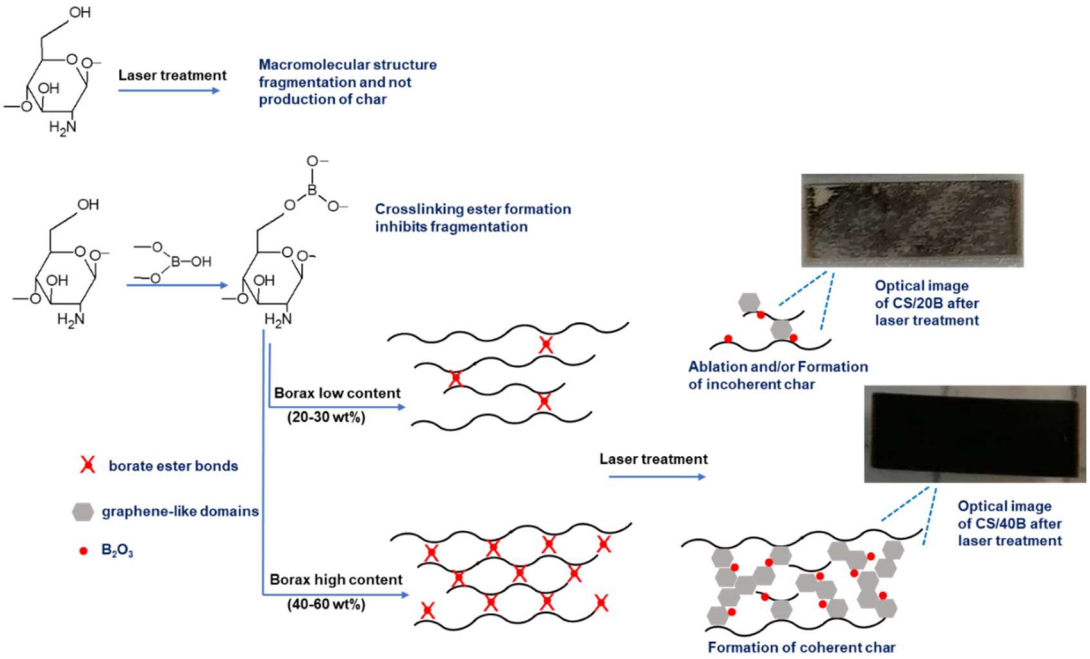
to 52.8% for CS/40B-LIG. The concentration of sp^2 carbon doubled, and the ratios of sp^2 carbon to other bonding forms and to oxygen content both more than tripled. Also confirmed was the remaining of surface carboxyl and carbonyl groups on the LIG sample, a useful surface feature for electrochemical applications. There was a substantial decrease in the total oxygen concentration in the CS/40B-LIG sample compared to the ungraphitised sample. In contrast, a relative increase in boron (from 2.4 to 7.5%) and sodium (from 3.2 to 4.6%) concentrations was observed in CS/40B-LIG samples compared to the ungraphitised samples. These data confirmed that borax facilitated the formation of LIG. Also, evidence the formation of B2O3 as a result of the graphitisation process was found from the XPS data. Overall, the XPS data confirmed that the CS/40B film was converted to LIG with high sp^2 carbon content, presence of surface oxygen groups, and that B_2O_3 was embedded as an oxide in the LIG network.

Table 4.2 Summary of XPS data for CS/40B pristine sample and LIG sample. For B1s peak, (a) indicates peak assignment for CS/40B; (b) indicates assignment for CS/40B-LIG.

Peak	Atomic Percentages (%)		Assignments
	CS/40B	CS/40B-LIG	
C1s A	26.4	52.8	C-C sp^2
C1s B	28.1	10.5	C-O, C-N
C1s C	6.2	3.6	C=O
C1s D		2.4	-C=O
C1s E		1.8	Carbonate
O1s A	0.5		C-O
O1s B	31	16.4	O=C
B1s	2.4	7.5	$Na_2B_4O_7$ (a), B_2O_3 (b)
Total C	60.7	71.1	
Total O	31.5	16.4	
C1s A/(B+C+D+E)	0.8	2.9	
C1s A/O	0.8	3.2	

Rationalising the experimental results, it is possible to speculate that borax, thanks to its intrinsic ability to generate char[34] and in the case of polysaccharides to cross-link macromolecules[32], is the key to allow formation of graphitisable formulations. In fact, it is well known that borate ions can form covalent bonds with the hydroxyl moieties of CS by forming borate ester bonds, which contribute to densifying the

polymeric network.[32, 33] In the absence of B or at B percentage lower than 30 wt %, the direct laser writing of films resulted in CS degradation by polymer weight fragmentation and no formation of aromatic char. The formation of a cross-linked structure inhibits fragmentation of the polymer chain and likely improves char formation by cyclisation and condensation.[36] The proposed graphitisation mechanism is shown in Scheme 4.1.



Scheme 4.1 Proposed mechanism of action of borax in LIG formation.

A comprehensive overview of the characteristics of LIG derived from sustainable sources is provided in Table 4.3. The Raman characteristics (intensity ratios of D/G and 2D/G peaks) do not vary widely for LIG derived from sustainable precursors. The sheet resistances are generally reported between 10 – 125 Ω/sq, with some materials ranging to kΩ/sq. In this context, the work presented in this paper is more resistive than most reported. Importantly, in terms of application, this material property does not inhibit the performance of electrochemical devices in comparison with those made using chromatography paper, cork, or chitosan.

Table 4.3 Comparison of CS/40B-LIG material characteristics with literature data.

Material	Laser	Raman (D/G)	Raman (2D/G)	R_{sh} (Ω/sq)	Application	Ref
Paper	UV (355 nm)			125	Humidity and temp. sensor	[61]
Wood	IR (10.6 µm)	0.8	0.5	10	Supercapacitors, water splitting electrodes	[62]
Watercolor paper	IR	1		40	-	[63]
Chromatography paper	IR	0.5		32	Strain sensor	[64]
Chromatography paper	IR	1.28	0.62	56	Electrochemical sensor	[65]
Chromatography paper	IR	>1	<1	30	Supercapacitor	[66]
Cellulose nanofibers	IR			16 k	-	[67]
Cork	UV	0.41	0.37	75	Pressure sensor	[68]
Cork	Visible (450 nm)	1	0.37	46	Electrochemical sensor	[69]
Chitosan	Visible (405 nm) & IR	~1		40	Electrochemical sensor	[70]
Carboxymethyl chitosan	IR	1.6	0.4	2.2 k	Triboelectric nanogenerators	[71]
Chitosan-borax composite	IR (10.6 µm)	1.2	0.5	110	Electrochemical sensor	This work

4.4.3 Electrochemical characterisation

An electrochemical characterisation of CS/40B-LIG was performed to assess its capability as electrode material for future electrochemical applications. Characterisation was performed with a three electrode electrochemical setup whereby LIG was used as working electrode. $[Fe(CN)_6]^{3-/4-}$, a standard redox probe which undergoes a reversible one-electron reaction, was used for this investigation. Cyclic voltammetry (CV) was employed to investigate the electron transfer kinetics of the CS/40B-LIG electrode. Figure 4.7a shows the electrode design used, with the dotted line indicating the area exposed to the analyte. The electrochemical cleaning of the electrode surface is shown in Figure 4.7b. The result of cycling in 1 M KCl for 10 min was the reduction of oxygen and oxygenated groups, at -0.4 V and -1.2 V respectively.[57]

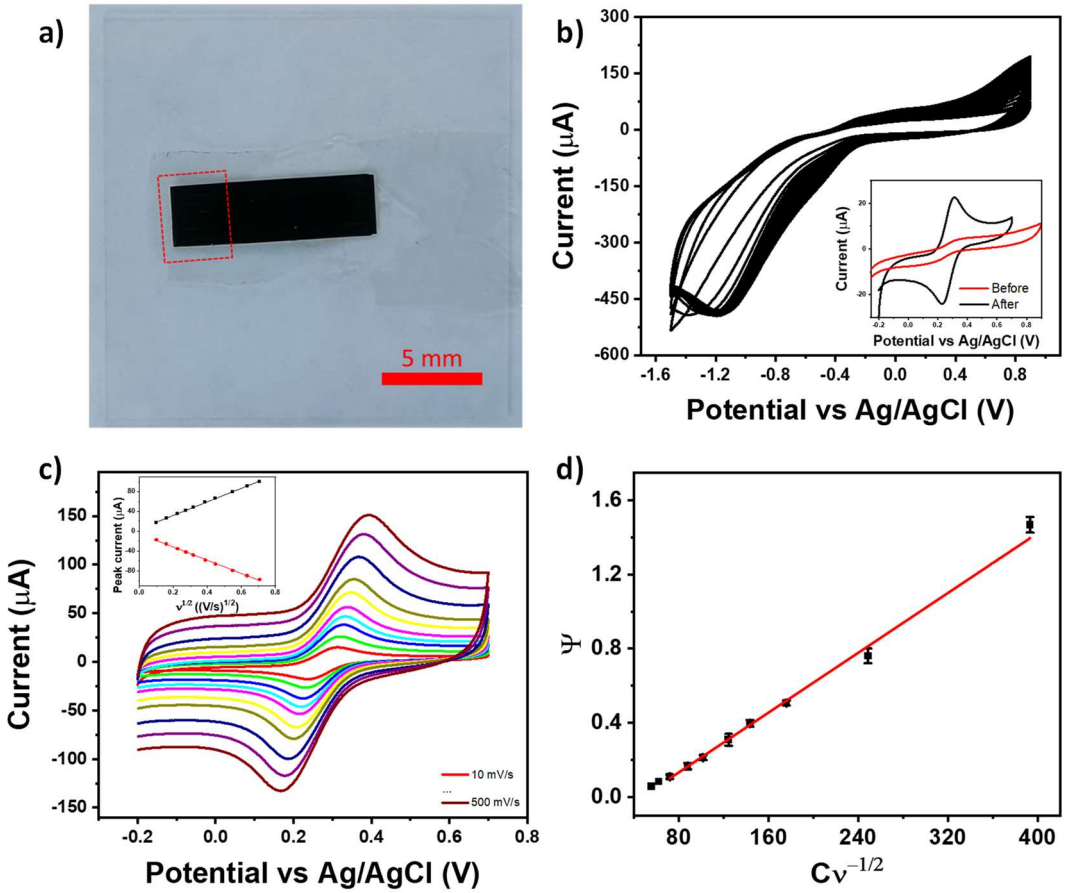


Figure 4.7 a) LIG electrode design with exposed area outlined by a dotted red square; **b)** cleaning cycles in 1 M KCl with oxygen reduction beginning around -0.5 V and oxygenated groups reduction peak appearing around -1.2 V. Inset showing effect of cleaning cycles on sensing of $Fe(CN)_6^{3-/4-}$; **c)** CV scans at varying scan rates for 5 mM $Fe(CN)_6^{3-/4-}$ in 1 M KCl. Inset shows peak oxidation and reduction current with square root of scan rate; **d)** k^0 calculation by the Nicholson method.

The effect of this electrochemical cleaning is seen in the inset of Figure 4.7b. The oxidation and reduction peak currents of $[Fe(CN)_6]^{3-/4-}$ increased in magnitude, the peaks became sharper and a reduced peak separation was observed. Figure 4.7c shows the cyclic voltammetry curves of $Fe(CN)_6^{3-/4-}$ measured between 10 and 100 mVs^{-1} scan rates. Fast electron transfer rates were observed, with ΔE_P values below 80 mV at 10 mVs^{-1}, and below 200 mV up to scan rates of 500 mVs^{-1}. The inset of Figure 4.7c shows linear plots of peak current (oxidation current and reduction current) with the square root of the scan rate, in line with the Randles-Ševčík equation and indicating a semi-infinite linear diffusion regime. Monitoring the values of ΔE_P with changing scan rate allowed for the determination of the hetero electron transfer rate (k^0) by the

Nicholas method. The value calculated for this material, shown in Figure 4.7d, was 4 x 10^{-3} cm s^{-1}. A comparison with literature values, including LIG on polyimide as a benchmark, is provided in Table 4.4. The k^0 value presented in this work is an order of magnitude larger than values seen for LIG on paper substrates, and much improved from electrochemical results previously reported for LIG on a chitosan-based biofilm. For [59] the electrochemical sensor was water-soluble, leading to a breakdown with time. The improvement of the water barrier properties of the chitosan-borax films presented in this paper allow for more stable devices. The rapid electron transfer kinetics presented here mean that this material is suitable for further use as an electrochemical sensing platform.

Table 4.4 Comparison of electron transfer properties for ferrocyanide with literature values for LIG on polyimide and natural precursors.

Material	Laser	ΔE_P (mV)	k^0_{app} (cm s^{-1})	Ref.
Polyimide	450 nm	61	1.26 x10^{-1}	[14]
Polyimide	405 nm	86	1.3 x10^{-2}	[48]
Filter paper	10.6 μm		7.8 x10^{-4}	[58]
Office paper	10.6 μm	>700	4.08 x10^{-4}	[39]
Chromatography paper	10.6 μm	370	6.85 x10^{-4}	[39]
Chitosan	10.6 μm and 405 nm	290		[59]
Cork	450 nm	90	9 x10^{-3}	[60]
Chitosan-borax	10.6 μm	110	4 x10^{-3}	This work

These results present an advanced material from renewable sources. Green LIG sensors are suitable for a variety of Internet of Things applications. The surface qualities of LIG allow for facile modification of the surface, making this an ideal platform for a green-biosensing platform. Chitosan-based films have been reported to have advantageous biocompatibility properties, and borax, used as a cross-linking agent, has also been reported to have such qualities.[72, 73] This is cause for further

optimism, in terms of deployment as a biosensing platform, however specific toxicity testing is required of all new material compositions.

4.5 Conclusions

The successful conversion of CS/xB formulations into high quality LIG has been presented. It was found that 40% wt. borax (with respect to CS weight) was the optimal content by monitoring electrical and Raman parameters of LIG. Borax content in the formulations' composition was found to play an important role in the formation of LIG by acting as a crosslinking agent for chitosan, and due to its flame retardant properties, which facilitated the high-temperature conditions necessary for LIG formation. The derived CS/40B-LIG displayed excellent properties as an electrochemical sensing platform. The k^0 value determined for $Fe(CN)_6$, 4 x 10^{-3} cm^2s^{-1}, is higher than that calculated for most other green-LIG sensors, and is higher than previous works on chitosan-based LIG. This showcases the potential for this material in future electrochemical applications. These CS-based films offer an important, environmentally friendly route to creating LIG materials, alternative to fossil fuel-derived synthetic polymers.

4.6 References

1. Novoselov, K.S., et al., *Electric Field Effect in Atomically Thin Carbon Films.* Science, 2004. **306**(5696): p. 666-669.
2. Zhu, J., et al., *Graphene and Graphene-Based Materials for Energy Storage Applications.* Small, 2014. **10**(17): p. 3480-3498.
3. Anindya Nag, A.M., Subhas Chandra Mukhopadhyay, *Graphene and its sensor-based applications: A review.* Sensors and Actuators A: Physical, 2018. **270**: p. 177-194.
4. A.G. Olabi, M.A.A., Tabbi Wilberforce, Enas Taha Sayed, *Application of graphene in energy storage device – A review.* Renewable and Sustainable Energy Reviews, 2021. **Volume 135**(110026).

5. Sang-Hoon Bae, Y.L., Bhupendra K. Sharma, Hak-Joo Lee, Jae-Hyun Kim, Jong-Hyun Ahn, *Graphene-based transparent strain sensor.* Carbon, 2013. **51**: p. 236-242.
6. Yam, K.M., et al., *Graphene-Based Heterogeneous Catalysis: Role of Graphene.* Catalysts, 2020. **10**(1): p. 53.
7. Ramesh, R., *Graphene: Fabrication Methods, Properties, and Applications in Modern Industries*, in *Graphene Production and Application*, A. Sadia, M.S. Akhtar, and S. Hyung-Shik, Editors. 2020, IntechOpen: Rijeka. p. Ch. 2.
8. Cote, L.J., R. Cruz-Silva, and J. Huang, *Flash Reduction and Patterning of Graphite Oxide and Its Polymer Composite.* Journal of the American Chemical Society, 2009. **131**(31): p. 11027-11032.
9. Mukherjee, R., et al., *Photothermally Reduced Graphene as High-Power Anodes for Lithium-Ion Batteries.* ACS Nano, 2012. **6**(9): p. 7867-7878.
10. El-Kady, M.F., et al., *Laser Scribing of High-Performance and Flexible Graphene-Based Electrochemical Capacitors.* Science, 2012. **335**(6074): p. 1326-1330.
11. Lin, J., et al., *Laser-induced porous graphene films from commercial polymers.* Nature Communications, 2014. **5**(1): p. 5714.
12. Vivaldi, F.M., et al., *Three-Dimensional (3D) Laser-Induced Graphene: Structure, Properties, and Application to Chemical Sensing.* ACS Applied Materials & Interfaces, 2021. **13**(26): p. 30245-30260.
13. Wang L, W.Z., Bakhtiyari AN, Zheng H., *A Comparative Study of Laser-Induced Graphene by CO2 Infrared Laser and 355 nm Ultraviolet (UV) Laser.* Micromachines (Basel), 2020. **11**(1094).
14. Vaughan, E., et al., *Visible Laser Scribing Fabrication of Porous Graphitic Carbon Electrodes: Morphologies, Electrochemical Properties, and Applications as Disposable Sensor Platforms.* ACS Applied Electronic Materials, 2020. **2**(10): p. 3279-3288.
15. Imbrogno, A., et al., *Laser-Induced Graphene Supercapacitors by Direct Laser Writing of Cork Natural Substrates.* ACS Applied Electronic Materials, 2022. **4**(4): p. 1541-1551.
16. Tan, P.S., et al., *Laser Scribing Fabrication of Graphitic Carbon Biosensors for Label-Free Detection of Interleukin-6.* Nanomaterials, 2021. **11**(8).
17. Madden, J., et al., *Electrochemical sensor for enzymatic lactate detection based on laser-scribed graphitic carbon modified with platinum, chitosan and lactate oxidase.* Talanta, 2022. **246**.
18. Paterakis, G., et al., *Highly Sensitive and Ultra-Responsive Humidity Sensors Based on Graphene Oxide Active Layers and High Surface Area Laser-Induced Graphene Electrodes.* Nanomaterials, 2022. **12**(15).
19. Liu, J., et al., *Laser-induced graphene (LIG)-driven medical sensors for health monitoring and diseases diagnosis.* Microchimica Acta, 2022. **189**(2): p. 54.
20. Yang, Y., et al., *A laser-engraved wearable sensor for sensitive detection of uric acid and tyrosine in sweat.* Nature Biotechnology, 2020. **38**(2): p. 217-224.
21. Pirson, T. and D. Bol, *Assessing the embodied carbon footprint of IoT edge devices with a bottom-up life-cycle approach.* Journal of Cleaner Production, 2021. **322**: p. 128966.

22. Piro, B., H.V. Tran, and V.T. Thu, *Sensors Made of Natural Renewable Materials: Efficiency, Recyclability or Biodegradability-The Green Electronics.* Sensors (Basel), 2020. **20**(20).
23. Vashisth, A., et al., *ReaxFF Simulations of Laser-Induced Graphene (LIG) Formation for Multifunctional Polymer Nanocomposites.* ACS Applied Nano Materials, 2020. **3**(2): p. 1881-1890.
24. Ye, R., et al., *Laser-Induced Graphene Formation on Wood.* Advanced Materials, 2017. **29**(37): p. 1702211.
25. de Araujo, W.R., et al., *Single-Step Reagentless Laser Scribing Fabrication of Electrochemical Paper-Based Analytical Devices.* Angewandte Chemie International Edition, 2017. **56**(47): p. 15113-15117.
26. Le, T.-S.D., et al., *Ultrafast Laser Pulses Enable One-Step Graphene Patterning on Woods and Leaves for Green Electronics.* Advanced Functional Materials, 2019. **29**(33): p. 1902771.
27. Zhang, C., et al., *Upgrading coal to multifunctional graphene-based materials by direct laser scribing.* Carbon, 2019. **153**: p. 585-591.
28. Chyan, Y., et al., *Laser-Induced Graphene by Multiple Lasing: Toward Electronics on Cloth, Paper, and Food.* ACS Nano, 2018. **12**(3): p. 2176-2183.
29. C. Claro, P.I., et al., *Sustainable carbon sources for green laser-induced graphene: A perspective on fundamental principles, applications, and challenges.* Applied Physics Reviews, 2022. **9**(4): p. 041305.
30. Larrigy, C., et al., *Porous 3D Graphene from Sustainable Materials: Laser Graphitization of Chitosan.* Advanced Materials Technologies, 2022. **n/a**(n/a): p. 2201228.
31. Huang, Q.-M., et al., *Laser-Induced Graphene Formation on Chitosan Derivatives toward Ecofriendly Electronics.* ACS Applied Nano Materials, 2023. **6**(12): p. 10453-10465.
32. Santillo, C., et al., *Hybrid Graphenene Oxide/Cellulose Nanofillers to Enhance Mechanical and Barrier Properties of Chitosan-Based Composites.* Front Chem, 2022. **10**: p. 926364.
33. Yan, N., et al., *Borate cross-linked graphene oxide–chitosan as robust and high gas barrier films.* Nanoscale, 2016. **8**(20): p. 10783-10791.
34. Dogan, M., et al., *Flame retardant effect of boron compounds in polymeric materials.* Composites Part B: Engineering, 2021. **222**: p. 109088.
35. Wang, F., J. Liu, and W. Lv, *Thermal degradation and fire performance of wood treated with PMUF resin and boron compounds.* Fire and Materials, 2017. **41**(8): p. 1051-1057.
36. Wicklein, B., et al., *Tuning the Nanocellulose–Borate Interaction To Achieve Highly Flame Retardant Hybrid Materials.* Chemistry of Materials, 2016. **28**(7): p. 1985-1989.
37. Duquesne, S. and S. Bourbigot, *10 Char Formation and Characterization.* Fire retardancy of polymeric materials, 2009: p. 239.
38. Coelho, J., et al., *Paper-based laser-induced graphene for sustainable and flexible microsupercapacitor applications.* Microchimica Acta, 2022. **190**(1): p. 40.

39. Pinheiro, T., et al., *Laser-Induced Graphene on Paper toward Efficient Fabrication of Flexible, Planar Electrodes for Electrochemical Sensing.* Advanced Materials Interfaces, 2021. **8**(22): p. 2101502.
40. Konopka, S.J. and B. McDuffie, *Diffusion coefficients of ferri- and ferrocyanide ions in aqueous media, using twin-electrode thin-layer electrochemistry.* Analytical Chemistry, 1970. **42**(14): p. 1741-1746.
41. Dreyfus, R.W., *CN temperatures above laser ablated polyimide.* Applied Physics A, 1992. **55**(4): p. 335-339.
42. Ye, R., D.K. James, and J.M. Tour, *Laser-Induced Graphene: From Discovery to Translation.* Advanced Materials, 2019. **31**(1): p. 1803621.
43. Dong, Y., S.C. Rismiller, and J. Lin, *Molecular dynamic simulation of layered graphene clusters formation from polyimides under extreme conditions.* Carbon, 2016. **104**: p. 47-55.
44. Childres, I., et al., *Raman spectroscopy of graphene and related materials.* New developments in photon and materials research, 2013. **1**.
45. Lespade, P., R. Al-Jishi, and M.S. Dresselhaus, *Model for Raman scattering from incompletely graphitized carbons.* Carbon, 1982. **20**(5): p. 427-431.
46. Nemanich, R.J., et al., *Raman scattering characterization of carbon bonding in diamond and diamondlike thin films.* Journal of Vacuum Science & Technology A, 1988. **6**(3): p. 1783-1787.
47. Hong, J., et al., *Origin of New Broad Raman D and G Peaks in Annealed Graphene.* Scientific Reports, 2013. **3**(1): p. 2700.
48. Burke, M., et al., *Fabrication and Electrochemical Properties of Three-Dimensional (3D) Porous Graphitic and Graphenelike Electrodes Obtained by Low-Cost Direct Laser Writing Methods.* ACS Omega, 2020. **5**(3): p. 1540-1548.
49. Neto, C.G.T., et al., *Thermal Analysis of Chitosan Based Networks.* Carbohydrate Polymers, 2005. **62**(2): p. 97-103.
50. Santillo, C., et al., *Hybrid Graphenene Oxide/Cellulose Nanofillers to Enhance Mechanical and Barrier Properties of Chitosan-Based Composites.* Frontiers in Chemistry, 2022. **10**.
51. Grossutti, M. and J.R. Dutcher, *Correlation Between Chain Architecture and Hydration Water Structure in Polysaccharides.* Biomacromolecules, 2016. **17**(3): p. 1198-1204.
52. Lawrie, G., et al., *Interactions between Alginate and Chitosan Biopolymers Characterized Using FTIR and XPS.* Biomacromolecules, 2007. **8**(8): p. 2533-2541.
53. Ritthidej, G.C., T. Phaechamud, and T. Koizumi, *Moist heat treatment on physicochemical change of chitosan salt films.* International Journal of Pharmaceutics, 2002. **232**(1): p. 11-22.
54. Qiao, C., et al., *Molecular interactions in gelatin/chitosan composite films.* Food Chemistry, 2017. **235**: p. 45-50.
55. Yusof, N.H., et al., *Microwave-Assisted Synthesis of Polyethyleneimine Grafted Chitosan Beads for the Adsorption of Acid Red 27.* Journal of Polymers and the Environment, 2020. **28**(2): p. 542-552.
56. Shankar, S. and J.-W. Rhim, *Bionanocomposite Films for Food Packaging Applications*, in *Reference Module in Food Science*. 2018, Elsevier.

57. Vivaldi, F., et al., *Sweat analysis with a wearable sensing platform based on laser-induced graphene.* APL Bioengineering, 2022. **6**(3): p. 036104.
58. Kulyk, B., et al., *Laser-induced graphene from paper for non-enzymatic uric acid electrochemical sensing in urine.* Carbon, 2022. **197**: p. 253-263.
59. Larrigy, C., et al., *Porous 3D Graphene from Sustainable Materials: Laser Graphitization of Chitosan.* Advanced Materials Technologies, 2023. **8**(4): p. 2201228.
60. Vaughan, E., et al., *Sustainable Laser-Induced Graphene Electrochemical Sensors from Natural Cork for Sensitive Tyrosine Detection.* Advanced Sensor Research, 2023. **n/a**(n/a): p. 2300026.
61. Kulyk, B., Silva, B. F. R., Carvalho, A. F., Barbosa, P., Girão, A. V., Deuermeier, J., Fernandes, A. J. S., Figueiredo, F. M. L., Fortunato, E., Costa, F. M., Laser-Induced Graphene from Paper by Ultraviolet Irradiation: Humidity and Temperature Sensors. Adv. Mater. Technol. 2022, 7, 2101311. https://doi.org/10.1002/admt.202101311
62. Ye, R., Chyan, Y., Zhang, J., Li, Y., Han, X., Kittrell, C., Tour, J. M., Adv. Mater. 2017, 29, 1702211. https://doi.org/10.1002/adma.201702211
63. Yieu Chyan, Joseph Cohen, Winston Wang, Chenhao Zhang, and James M. Tour. ACS Applied Nano Materials 2019 2 (5), 3007-3011. DOI: 10.1021/acsanm.9b00391
64. Bohdan Kulyk, Beatriz F. R. Silva, Alexandre F. Carvalho, Sara Silvestre, António J. S. Fernandes, Rodrigo Martins, Elvira Fortunato, and Florinda M. Costa. ACS Applied Materials & Interfaces 2021 13 (8), 10210-10221. DOI: 10.1021/acsami.0c20270
65. Pinheiro, T., Silvestre, S., Coelho, J., Marques, A. C., Martins, R., Sales, M. G. F., Fortunato, E., Laser-Induced Graphene on Paper toward Efficient Fabrication of Flexible, Planar Electrodes for Electrochemical Sensing. Adv. Mater. Interfaces 2021, 8, 2101502. https://doi.org/10.1002/admi.202101502.
66. Coelho, J., Correia, R.F., Silvestre, S. et al. Paper-based laser-induced graphene for sustainable and flexible microsupercapacitor applications. Microchim Acta 190, 40 (2023). https://doi.org/10.1007/s00604-022-05610-0
67. Sanghee Lee and Sangmin Jeon; ACS Sustainable Chemistry & Engineering 2019 7 (2), 2270-2275. DOI: 10.1021/acssuschemeng.8b04955
68. Carvalho, A. F., Fernandes, A. J. S., Martins, R., Fortunato, E., Costa, F. M., Laser-Induced Graphene Piezoresistive Sensors Synthesized Directly on Cork Insoles for Gait Analysis. Adv. Mater. Technol. 2020, 5, 2000630. https://doi.org/10.1002/admt.202000630
69. Vaughan, E., Santillo, C., Setti, M., Larrigy, C., Quinn, A.J., Gentile, G., Lavorgna, M. and Iacopino, D. (2023), Sustainable Laser-Induced Graphene Electrochemical Sensors from Natural Cork for Sensitive Tyrosine Detection. Adv. Sensor Res. 2300026. https://doi.org/10.1002/adsr.202300026
70. Larrigy, C., Burke, M., Imbrogno, A., Vaughan, E., Santillo, C., Lavorgna, M., Sygellou, L., Paterakis, G., Galiotis, C., Iacopino, D., Quinn, A. J., Porous 3D Graphene from Sustainable Materials: Laser Graphitization of Chitosan. Adv. Mater. Technol. 2023, 8, 2201228. https://doi.org/10.1002/admt.202201228

71. Qian-Ming Huang, Huiru Yang, Shaogang Wang, Xu Liu, Chunjian Tan, Anxin Luo, Siyuan Xu, Guoqi Zhang, and Huaiyu Ye; ACS Applied Nano Materials 2023 6 (12), 10453-10465. DOI: 10.1021/acsanm.3c01408
72. Ji Ha Lee, Tomoyuki Tachibana, Hijiri Wadamori, Keita Yamana, Riku Kawasaki, Shogo Kawamura, Hinata Isozaki, Mina Sakuragi, Isamu Akiba, and Akihiro Yabuki, *Drug-Loaded Biocompatible Chitosan Polymeric Films with Both Stretchability and Controlled Release for Drug Delivery*, ACS Omega 2023 8 (1), 1282-1290 DOI: 10.1021/acsomega.2c06719
73. Amit Kumar Sharma, Priya, Balbir Singh Kaith, Bhagya Shree, Simran, Saiyam, *Borax mediated synthesis of a biocompatible self-healing hydrogel using dialdehyde carboxymethyl cellulose-dextrin and gelatin*, Reactive and Functional Polymers, Volume 166, 2021, 104977, https://doi.org/10.1016/j.reactfunctpolym.2021.104977.

Chapter 5: Sustainable Laser Induced Graphene Electrochemical Sensors from Natural Cork for Sensitive Tyrosine Detection

5.1 Abstract

Cork Laser Induced Graphene (cork-LIG) electrochemical sensors were fabricated by direct laser writing of natural cork sheets. Laser writing was performed with a hobbyist visible laser. The obtained cork-LIG structures displayed graphene-like Raman signatures, high conductivity and fast electron-transfer rates. After a ten minute electrochemical pre-treatment, electrodes were used for detection of Tyrosine in the presence of Uric Acid, Dopamine, Ascorbic Acid, Urea and Glucose. Linear detection of Tyrosine was achieved in the 5-150 μM range with a limit of detection (LOD) of 3.03 μM. Calibration of Dopamine detection was achieved with a LOD of 1.1 μM. Finally, the cork-LIG electrochemical sensors showed linear response of Tyr in artificial sweat in the relevant physiological range of 5-250 μM (sensitivity, 1.8 x10^{-2} A M^{-1}). The LOD was calculated as 3.75 μM. These results open the door to the exploitation of renewable materials such as cork for the development of high-quality, green sensors for the monitoring of health and wellbeing parameters.

Published: Adv. Sensor Res. 2023, 2300026. https://doi.org/10.1002/adsr.202300026

5.2 Introduction

Cork is a renewable, recyclable, natural material derived from the bark of the *Quercus suber L*. tree. Cork is periodically harvested (every 9 – 12 years), renewing itself without causing any harm to the tree. The chemical composition of cork is different than wood. It possess lower content of cellulose and hemicellulose, a higher content of the aromatic biopolymer lignin, and has a high content of the aliphatic and aromatic biopolymer suberin.[1, 2] At the microscopic level, cork displays a morphology with a honeycomb structure characterized by pentagonally- and hexagonally-arranged hollow cells. The cell walls are covered with highly hydrophobic suberin and lignin molecules (Figure 5.1b, c). The high surface area and hollow structure, as well as its chemical composition, confer cork a unique set of properties such as lightness, low-density, compressibility, impermeability, high resistance to combustion, and low thermal conductivity.[3, 4] As result, cork is used in a wide variety of products ranging from stoppers for wine bottles, seals and pads in woodwind instruments, thermal and acoustic insulation, activated carbon. Cork has even been applied as a thermal and anti-vibration shield in spacecraft by both NASA and ESA.[4]

Direct Laser Writing techniques have recently emerged as suitable methods for the fast and versatile production of graphene-like materials.[5] In this approach, pioneered by Tour *et al*., a CO_2 laser is used to "write" features on flexible polymers, usually polyimide.[6-8] The writing process leads to the formation of Laser Induced Graphene (LIG), a high surface area, 3D, conductive (< 20 Ω sq^{-1}), graphene-like material resulting from the localised high-temperature, high-pressure environment created by the laser. Among the wide range of uses, the high surface area and high density of defects of LIG materials have proven particularly suitable for electrochemical

applications.[9-11] Great efforts in the last few years have focused on the development of laser writing processes applicable to biodegradable and naturally sourced materials, alternative to synthetic, fossil fuel derived polymers. By widening the range of laser wavelengths from the IR (10.6 um) to the visible (450 and 405 nm) and UV (355 nm), several groups have demonstrated production of LIG from paper,[12-14] cardboard,[15] wood,[16] lignin-rich materials,[17] chitosan-based films,[18] cloth and even food (coconut shells and potato peels).[19, 20] Remarkably, these green LIG materials have exhibited Raman spectroscopic signatures of graphene-like materials with I_{2D}/I_G ratios > 0.6 and I_D/I_G ratios close to 1, as well as low sheet resistances (< 50 $\Omega\,sq^{-1}$). Successful proof of concept demonstrations of next generation green electronics have been demonstrated, such as glucose electrochemical sensing,[21] electronic functionalities for paper electronics,[22] wood electronics[23] and energy harvesting/storage.[24]

Cork is used either as natural cork, as harvested from the tree, or as agglomerated cork, in which pulped cork is reformed into sheets using a binding agent. Carbonisation of natural cork at 1000 °C has been shown to result in a polyaromatic carbon material, between graphitic carbon and amorphous carbon. The honeycomb cell structure of cork was maintained after carbonisation, which resulted in an ideal structure for use as a high-performance field emitting device.[25] Recently, laser graphitization of natural and agglomerated cork has been demonstrated with IR, UV and visible low cost hobbyist lasers. For example, Imbrogno *et al.* used one-step visible laser writing on natural cork stoppers to fabricate cork-LIG supercapacitors, which showed > 11 mF cm^{-2} areal capacitance and only 14% loss over 10000 charge discharge cycles.[26] Carvalho *et al.* have used agglomerated and natural cork-LIG as piezoresistive material for the monitoring of human gait in insoles.[27] Agglomerated cork-LIG triboelectric

generators were used in combination with polyimide LIG electrodes, which generated open circuit voltages > 3.5 V and peak power > 8 mV.[28]

In this manuscript we present for the first time the use of natural cork-LIG electrodes as an electrochemical sensing platform. Cork-LIG was fabricated with a one-step laser irradiation process (450 nm) on pristine cork sheets. Following laser conditions optimization, the fabricated cork-LIG displayed low sheet resistance (10 Ω sq^{-1}), a Raman signature of disordered crystalline graphene-like material and high density of sp^2 carbon bonds. Electrode materials with fast electron transfer rates (k^0_{app} = 9 x 10^{-3} cm s^{-1} for $[Fe(CN)_6]^{3-/4-}$) were obtained after an electrochemical activation process. This process, lasting only 10 min, improved the surface quality of cork-LIG by increasing the percentage of C=C bonds and decreasing the percentage of C-O bonds arising from the laser burning process. As result, sensitive detection of Tyr and concomitant detection of Tyr, dopamine (DA) and uric acid (UA) was achieved, with linear responses in the relevant detection range for physiological fluids. These results introduce a novel, eco-friendly, high-sensitivity electrochemical sensor with qualities that enable monitoring of metabolites in the human body.

5.3 Experimental section

5.3.1 Materials

Natural cork sheets with dimensions 40 x 60 mm with thickness 2 mm were purchased from Alomejor and used without further treatment. L-Tyrosine, dopamine hydrochloride, uric acid, L-ascorbic acid, urea and D-glucose were purchased from Merck and used without further purification. Sodium Acetate Buffer (ABS) was purchased from Merck at 3 M and diluted to 0.01 M for experiments. Ferrocyanide ($[Fe(CN)_6]^{4-}$) was prepared from $K_4Fe(CN)_6$ (Merck). All solutions were prepared using deionized Milli-Q water (resistivity 18.2 MΩ.cm).

5.3.2 Electrode fabrication

Cork-LIG electrodes were fabricated with a KKmoon Compact Automatic Desktop Laser Engraving Machine equipped with a laser with 3 W power and illumination wavelength of 450 nm. Electrode structures were designed in Microsoft PowerPoint and transferred to the laser engraving software, which wrote them to the cork substrate by raster scanning of the laser beam. Laser power (LP, % of 3 W) and depth adjustment (DA – a KKmoon parameter related to laser dwell time) were adjusted in the laser engraving software. Ag/AgCl paste was purchased from Merck and applied directly to the cork. Conductive silver paint (Merck) was applied to the device for electrically contacting the electrodes to the potentiostat.

5.3.3 Characterisation

Graphitic carbon electrodes were morphologically characterized by a cold-cathode field-emission Scanning Electron Microscope (SEM, JSM- 7500F, JEOL UK Ltd.) operating at 5 kV acceleration voltage. Bright field transmission electron microscopy (TEM) analysis was performed by means of a FEI Tecnai G12 Spirit Twin (LaB6 source) at 120 kV acceleration voltage. TEM images were collected on a FEI Eagle 4 k CCD camera. White light optical microscopy images were acquired with a Zeiss Stemi 508 Microscope interfaced to a Zeiss Axiocam 208 colour microscope camera. Raman investigation was performed with Horiba-XPlora equipped with a 532 nm laser (70 mW at sample). Spectra were acquired at a laser power of 10% and 30 s acquisition time. X-ray photoelectron spectroscopic (XPS) measurements were acquired at room temperature by using an Escalab 250Xi (Thermo Fisher Scientific, UK) spectrometer, equipped with a monochromatic Al Kα excitation source, electron and ion flood guns for charge neutralization and a 6-channeltron detection system. The photoemission spectra were collected at 20 eV pass energy, and the diameter of analysed area was

about 1 mm. The XPS core level spectra of C1s and N1s were analysed using a fitting routine, where each spectrum was decomposed into a series of individual mixed Gaussian-Lorentzian peaks following a Shirley background subtraction. Surface wettability was measured by a Dataphysics OCA 20 Wetting angle system in air at ambient temperature by dropping distilled water droplets (1 mm diameter) on the surfaces. The average contact angle value was acquired by measuring at three to six different positions per sample.

Two-terminal current−voltage measurements (±1 V, 20 mV step) were obtained under ambient conditions on transmission line method (TLM) structures using an Wentworth PML 8000 probe station and Agilent E4980A parameter analyser. Track resistance values for varying channel lengths were calculated from linear fits of I-V plots. Plots of track resistance versus channel length were used to calculate sheet resistance (R_{SH}) and contact resistance (R_{CT}).

5.3.4 Electrochemical analysis

Cyclic voltammetry (CV) and Square Wave Voltammetry (SWV) electrochemical measurements were performed with a CHI760 bi-potentiostat. The parameters for the SWV measurements were: 0.005 V increment; 0.025 V amplitude; 5 Hz frequency. Cork-LIG structures, produced at the same laser settings, were used as a working (WE) and counter (CE) electrode. An acrylic based nail varnish was used to delimit the WE area, improving the reproducibility of the active area. Ag/AgCl paste, applied directly to the cork, was used as a reference electrode. For the initial electrochemical optimisation, an external Ag/AgCl RE and a Pt wire CE were used. The device was assembled in a Teflon cell with a circular area of 8 mm diameter exposed to the electrolyte. Heterogeneous electron transfer (HET) rate constants (k^0_{app}) were determined from the anodic/cathodic peak separation using the method of

Nicholson[29] by assuming transfer coefficient $\alpha = 0.5$ and using the following diffusion coefficients: $[Fe(CN)_6]^{4-/3-}$ $D_0 = 7.26 \times 10^{-6}$ cm^2 s^{-1}, $D_R = 6.67 \times 10^{-6}$ cm^2 s^{-1}.[30]

5.3.5 Electrochemical pre-treatment activation

Prior electrochemical analysis cork-LIG electrodes were cycled in 1 M KCl for 50 cyclic voltammetry cycles (10 minutes) from -0.7 to 0.9 V at 200 mVs^{-1}. The reduction of surface oxygen close to -0.5 V was vital for achieving an enhanced electrode performance. A single wide scan was performed prior to the cycling, to ensure that the oxygen reduction event was captured within the -0.7 to 0.9 V electrochemical window in the case of an initial overpotential.

5.4 Results and discussion

5.4.1 Device fabrication

The as-acquired cork substrate measured 20 × 20 x 2 mm, as shown in Figure 5.1a. This was divided into individual 2 cm^2 sheets for devices. The chemical structures of lignin and suberin are displayed in Figure 5.1b, c respectively.

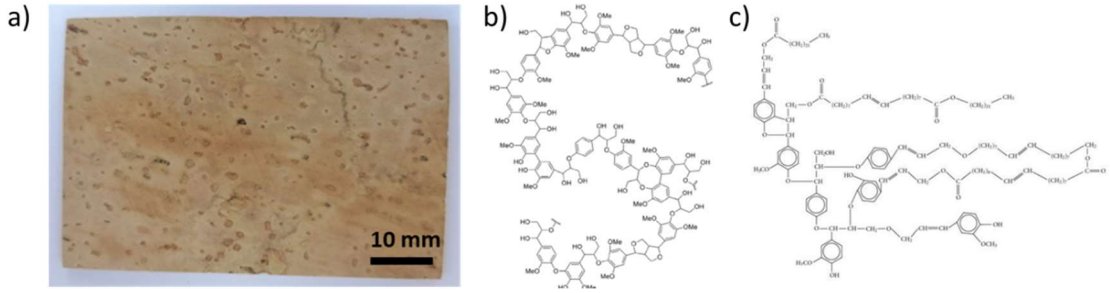


Figure 5.1 a) Natural cork sheet as acquired; **b)** lignin chemical structure; **c)** suberin chemical structure.

Figure 5.2a shows the schematic of the fabrication of the cork-LIG electrochemical sensor platform. Two identical cork-LIG electrodes measuring 11 × 1.5 mm, with 1 mm separation, were scribed using a 450 nm laser. These were used as the working and counter electrode. The active area of the working electrode was reduced to

approximately 2 × 1.5 mm by passivation with an acrylic-based nail varnish. Ag/AgCl ink was applied close to the LIG electrodes for use as a reference electrode. Conductive Ag paint was applied to the electrodes to allow for connection of the device to the potentiostat when placed in the Teflon cell. A photograph of the ready-to-use device is shown in Figure 5.2b, with the dimensions indicated in the microscope image of Figure 5.2c. Fabrication time with the laser was 44 seconds per device, and application of the Ag/AgCl and conductive Ag paint brought the entire fabrication time to approximately 10 minutes for six devices (cork sheets of 40 x 60 mm served for six devices). For the initial optimisation of the laser parameters, an external Ag/AgCl reference and a Pt wire counter electrode were used.

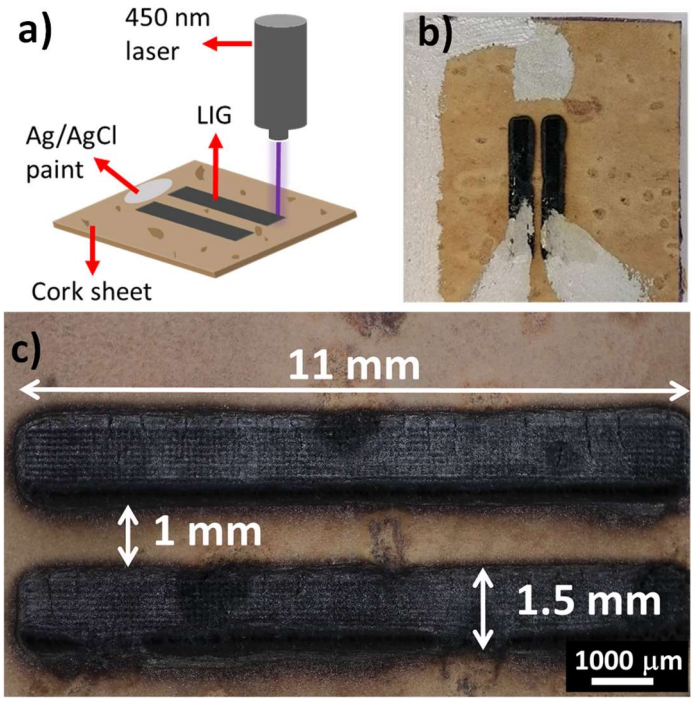


Figure 5.2 **a)** Schematic of the laser engraving of the LIG electrodes on cork substrate; **b)** photographic image of the planar 3-electrode device on cork; **c)** white light microscope image of the cork-LIG electrodes.

5.4.2 Laser settings optimisation

LIG electrodes are known for their fast electron transfer rates and high specific surface area, both of which are highly dependent on the laser conditions (wavelength, power, speed).[11, 31] While these characteristics have widely been explored for

polyimide-LIG, very few examples of cork-LIG are available in literature.[26-28] As such, a detailed investigation of the laser writing process on cork was performed in order to find the optimum conditions for device fabrication. This was done by writing rectangular features (3 mm x 9 mm) on cork at various laser power/speed (depth adjustment) combinations followed by an investigation of the electrical, Raman, and electrochemical behaviour of the cork-LIG.

Figure 5.3a shows a photograph of the cork-LIG features on cork obtained by using 20% to 60% laser powers (LP, % of 3 W) and 20 to 50 depth adjustment (DA) combinations. The resulting cork-LIG structures showed visible differences: at the low end of the scale (low LP, low DA – LP20-DA20) the features appeared dark grey, sharply defined, and were co-planar with the cork substrate. At the high end of the scale (high LP, high DA – LP50-DA50, LP30-DA60) the features appeared black, included a spreading of the graphitized area beyond the desired shape, and were receeded into the cork. These structures were classified as surface features and receeded features and further analyzed.

Electrical characterization (see Figure 5.3b) showed that with increasing power, the graphitised features displayed a decreasing sheet resistance – from 54 Ω sq^{-1} at LP30-DA20 to 10 Ω sq^{-1} at LP60-DA30, following a trend already indentified for polyimide LIG and also for green LIG derived from biodegradable precursors.[17] Results for LP20% were omitted, as they displayed resistances in the kΩ order of magnitude. Based on these initial findings, cork-LIG samples obtained from six laser settings were selected for further analysis. Representitive Raman spectra for each of the six samples, based on qualities averaged over 15 spectra per sample, are displayed in Figure 5.3c. The cork-LIG structure obtained at LP30-DA40 represented the surface feature, whereas the cork-LIG structure written at LP60-DA30 represented the extreme of the

receeded feature. Despite the visual differences, Raman characterisation was not sufficient to discern the quality of one cork-LIG structure over another. Each structure showed distinct and sharp D, G, and 2D peaks. Only small variations of the peaks FWHMs, positions and intensity ratios (I_D/I_G and I_{2D}/I_G) were observed (see full details in Table 5.1). This data indicates that high quality LIG was produced at each setting. In order to gain further insight into the most apporopriate laser settings for the fabrication of electrode materials, electrochemical characterisation of cork-LIG electrodes was carried out using cyclic voltammetry (CV). The standard reversible redox couple Ferro/ferricyanide ($[Fe(CN)_6]^{3-/4-}$) was used for this characterisation. The peak to peak separation (ΔE_P) and peak current (I_p) were considered as quality selection paramenters. For this optimisation step a simple design of a 3 mm wide LIG electrode spanning the 8 mm base of the electrochemical cell was used as working electrode together with external counter (Pt) and reference (Ag/AgCl) electrodes. Figure 5.3d displays six CV curves at 100 mV s^{-1} scan rate obtained at the selected laser settings. The cork-LIG produced at LP50-DA30 (green curve) showed the sharpest peaks, with the largest I_P values and the lowest ΔE_P values. The superiority of the LP50-DA30 electrode is clearly evident in the histogram shown as inset in Figure 5.3d. LP50-DA30 was the optimal setting considering kinetics, current response, and repeatability. All further data presented in this work were obtained with cork-LIG structures fabricated at LP50-DA30.

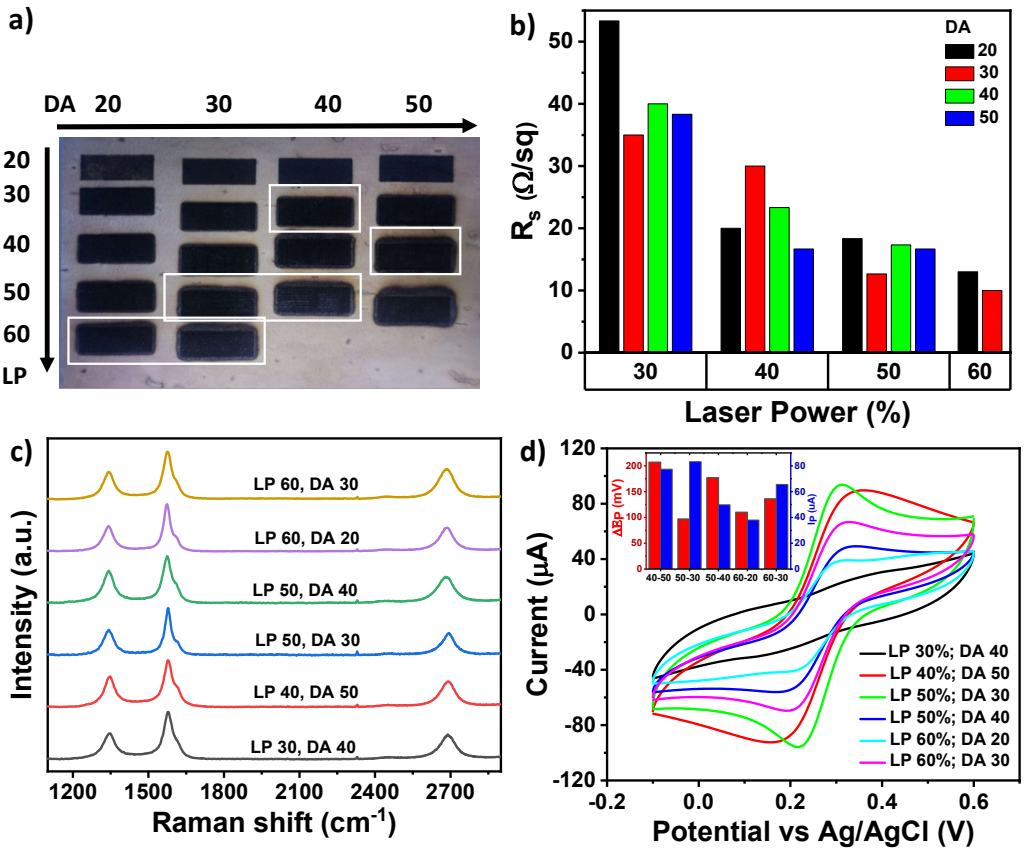


Figure 5.3 a) 3 x 9 mm features written on cork with varying laser parameters (LP 20 to 60% and DA 20 to 50); **b)** Sheet resistance measured for cork-LIG structures shown in a; **c)** Representative Raman spectra of cork-LIG features shown in a); **d)** CV scans (100 mV s^{-1}) of 5 mM $Fe[CN]_6^{3-/4-}$ in 1 M KCl at cork-LIG working electrodes obtained under laser settings described in a). Inset: peak separation and peak current of CVs.

Table 5.1 Full Raman spectroscopy data for six laser settings. Mean value shown, σ is the standard deviation for 15 measurements per setting.

Sample	$FWHM_D$	$FWHM_G$	$FWHM_{2D}$	I_D/I_G	I_{2D}/I_G	Pos-D	Pos-G	Pos-2D
30% LP-40 DA	55 (σ = 7)	44 (σ = 6)	75 (σ = 9)	0.8 (σ = 0.1)	0.9 (σ = 0.1)	1344 (σ = 3)	1577 (σ = 3)	2686 (σ = 5)
40% LP-50 DA	64 (σ = 15)	50 (σ = 11)	73 (σ = 9)	0.8 (σ = 0.2)	0.8 (σ = 0.2)	1345 (σ = 3)	1578 (σ = 3)	2688 (σ = 4)
50% LP-30 DA	57 (σ = 14)	42 (σ = 13)	70 (σ = 14)	0.8 (σ = 0.2)	0.9 (σ = 0.3)	1345 (σ = 3)	1578 (σ = 3)	2689 (σ = 5)
50% LP-40 DA	59 (σ = 11)	47 (σ = 7)	80 (σ = 17)	0.9 (σ = 0.3)	0.9 (σ = 0.1)	1343 (σ = 3)	1576 (σ = 3)	2683 (σ = 6)
60% LP-20 DA	60 (σ = 16)	42 (σ = 10)	71 (σ = 10)	0.7 (σ = 0.2)	0.9 (σ = 0.2)	1346 (σ = 4)	1579 (σ = 3)	2689 (σ = 6)
60% LP-30 DA	51 (σ = 6)	40 (σ = 9)	68 (σ = 12)	0.7 (σ = 0.2)	1 (σ = 0.2)	1345 (σ = 3)	1577 (σ = 3)	2688 (σ = 5)

5.4.3 Material characterisation

Following selection of the optimal writing conditions, further characterisation of the cork-LIG material was carried out.

SEM micrographs of the pristine cork surface and the cork-LIG surface are displayed in Figure 5.4. Low (a) and high (b) magnification images of raw cork show the typical ordered structure characterized by cells organized in an alveolar structure, with tight

pentagonal and hexagonal packing.[3] Crouvisier-Urion *et al.* have distinguished the cell structure of harvested cork along planes perpendicular to the axial, radial and tangential directions with respect to the tree.[3] The hexagonal/pentagonal structure of the surface is characteristic of the radial plane, with rectangular cells seen in the cross section (Figure 5.4e, f) corresponding to the tangential/axial plane. Upon laser graphitization, low (c) and high (d) magnification SEM images show that the original honeycomb structure of the cork was maintained. The cell bases appear ablated, leaving residual long, hollow columns. This is similar to the conversion seen for carbonisation of cork at 1000 °C, but in contrast to UV cork-LIG in which cork cells collapsed to leave thin LIG layers.[25, 27] The effect of the laser raster movement is evident in Figure 5.4d. The surface morphology displayed distinctive grooves. The structure differed from the familiar wrinkled, porous structure seen in polyimide LIG (PI-LIG).[8, 11] It is known that the morphology of PI-LIG is caused by explosions of trapped gas pockets created by the out-gassing of nitrogen and oxygen during graphitisation.[8] In the case of cork-LIG, the underlying porous nature of pristine cork likely allowed for the removal of oxygen without creating pressurised, trapped gas. The cross sectional SEM (Figure 5.4e) shows that the cork was graphitised to uneven depths. This is most likely due to the inhomogeneity of the naturally precursor. The LIG width ranged from 500 – 680 μm, while the largest recession of the LIG surface from the cork surface was 195 μm. This is very deep for LIG formation, surpassed in literature only by LIG formed on wood (see Table 5.3).

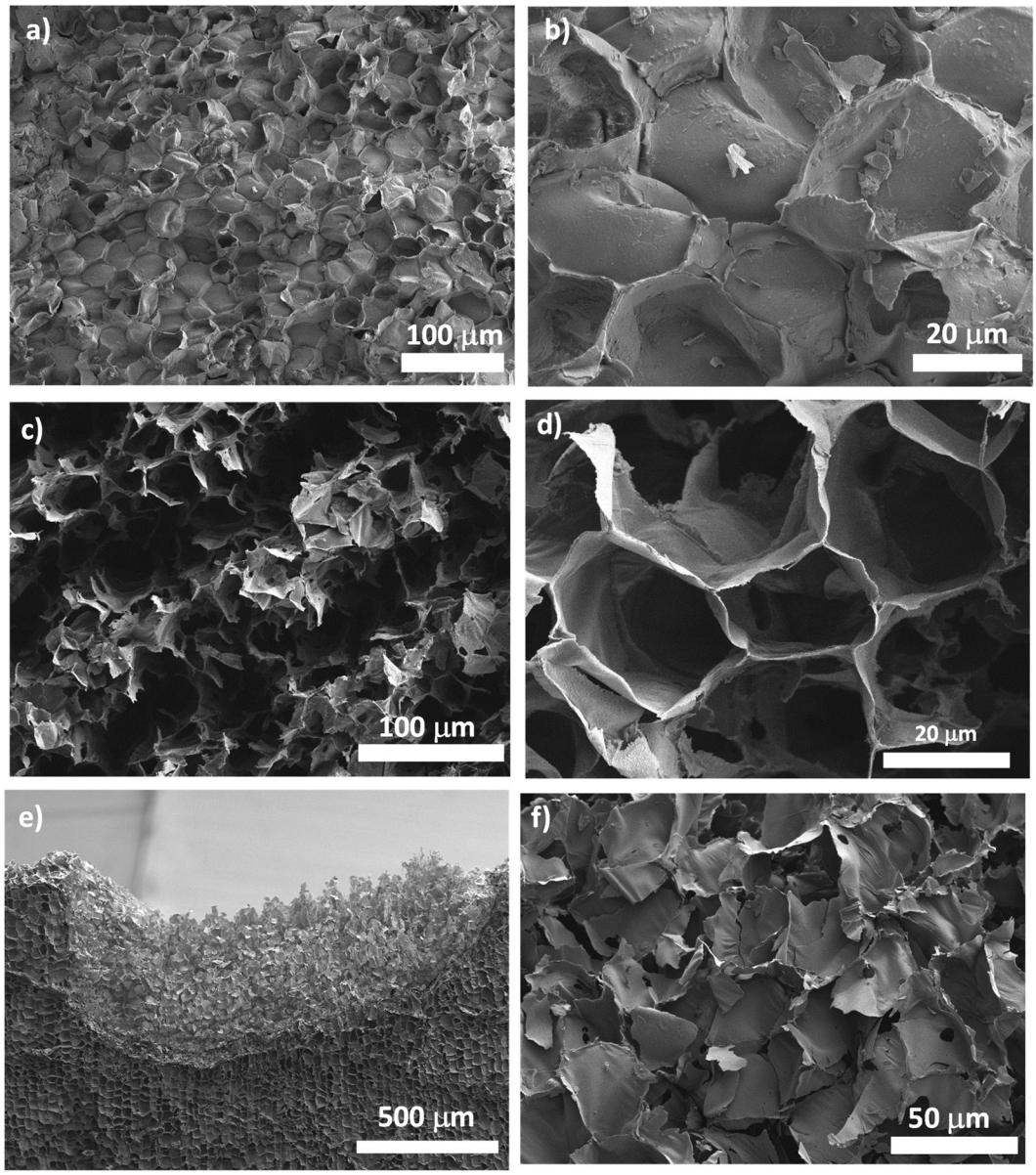


Figure 5.4 SEM micrographs displaying **a)** low-magnification raw cork surface; **b)** high-magnification raw cork surface; **c)** low-magnification cork-LIG surface; **d)** high-magnification cork-LIG surface; **e)** cross-section of cork-LIG electrode (enhanced contrast); **f)** high-magnification cross-section cork-LIG.

Figure 5.5a shows a representative Raman spectrum for the cork-LIG material obtained under optimized laser parameters. The spectrum is characterized by three main peaks centred at 1345, 1578 and 2689 cm^{-1} corresponding to the D peak (induced by bent sp^2 carbon bonds and associated with the presence of defects), G peak (corresponding to the E2g vibration mode of graphitic carbon) and 2D peak, respectively.[32, 33] The D, G and 2D peaks were each fitted with Lorentzian peaks with full width at half maximums (FWHM) of 57, 42 and 70 cm^{-1} respectively. The

sharpness of these peaks indicates the high quality of the cork-LIG. The low intensity of the D peak relative to the G peak confirms the low density of defects formed.[34] The high intensity of 2D peak shows the formation of graphene-like carbon structures. The ratio of integrated intensities I_D/I_G equal to 0.8 confirms the crystalline nature of the ablated surface, whereas the high I_{2D}/I_G of 0.9 indicates a multilayer graphene structure.[35] In accordance with the work of Robertson and Ferrari, this cork-LIG Raman data suggest a material with nanocrystalline graphitic domains in a disordered carbon matrix.[32] This profile is consistent with 2D graphitic structures consisting of randomly stacked graphene layers along the c-axis, already reported for LIG structures obtained by laser writing of polyimide with this 450 nm laser and with high power infrared laser sources.[8, 11, 34]

TEM data (Figure 5.5 b) displays many multi-layered graphene domains. The calculated interlayer spacing was 3.47 Å. For bilayer graphene, the figure is 3.4 Å, while for bulk graphite it can vary between 3.34 – 3.69 Å. [36, 37] For LIG structures obtained from cork, wood and PI the average lattice spacing ranged from 3.4 – 3.5 Å.[8, 16, 26]

Figure 5.5 c, d show the deconvoluted C1S XPS scans of pristine cork and cork-LIG, respectively. Both spectra are dominated by a large C1s A peak, representing the contribution from C=C bonds. Contributions from other carbon bonds were labelled B (C-C), C (C-OH, -C-O) and D (C=O). Table 5.2 shows the summary of atomic percentages found in XPS for pristine cork sheets, cork-LIG, and the electrochemically activated cork-LIG (to be discussed later). The structures were compared in terms of C1s-A atomic %, ratio of A:(B+C+D) peaks in the C1s, total oxygen atomic percentage, ratio of C1s-A:O, and the D parameter. In the pristine cork sample the C1s-A peak represented an overall atomic percentage of 42.3 %, which increased to

61.0% in the cork-LIG material. The large peak observed in the raw cork was ascribed to cork's primary constituents suberin and lignin, both highly aromatic compounds (Figure 5.1b, c).[38] The increased signal in the laser-treated region was associated to the conversion from cork to LIG, a graphene-like material – in agreement with the Raman data. In particular, the ratio of the A peak with the other carbon components [A/(B+C+D)] indicates the content of C=C carbon (graphite or graphene) whereas the ratio of the A peak with the total oxygen indicates the quality of the laser treatment. As expected, both parameters were greater in the cork-LIG than the untreated cork, indicating a higher content of C=C bonds and a lower content of oxygen. The oxygen content of graphitic structures has also been cited as an indirect method of deducing the density of edge defects, associated with an enhanced chemical and electrochemical reactivity.[39, 40] Oxygen groups form and migrate to graphitic edge sites.[41, 42] The oxygen content in LIG (12%) can be related to a large exposure of edge planes. The value of the D parameter was 14 eV for the cork-LIG. Values of 13.5 – 15 eV are typical for graphene, whereas for graphite it is 21.2 eV. The low D value for the untreated sample is typical for polymers with different C-O bonds.[43].

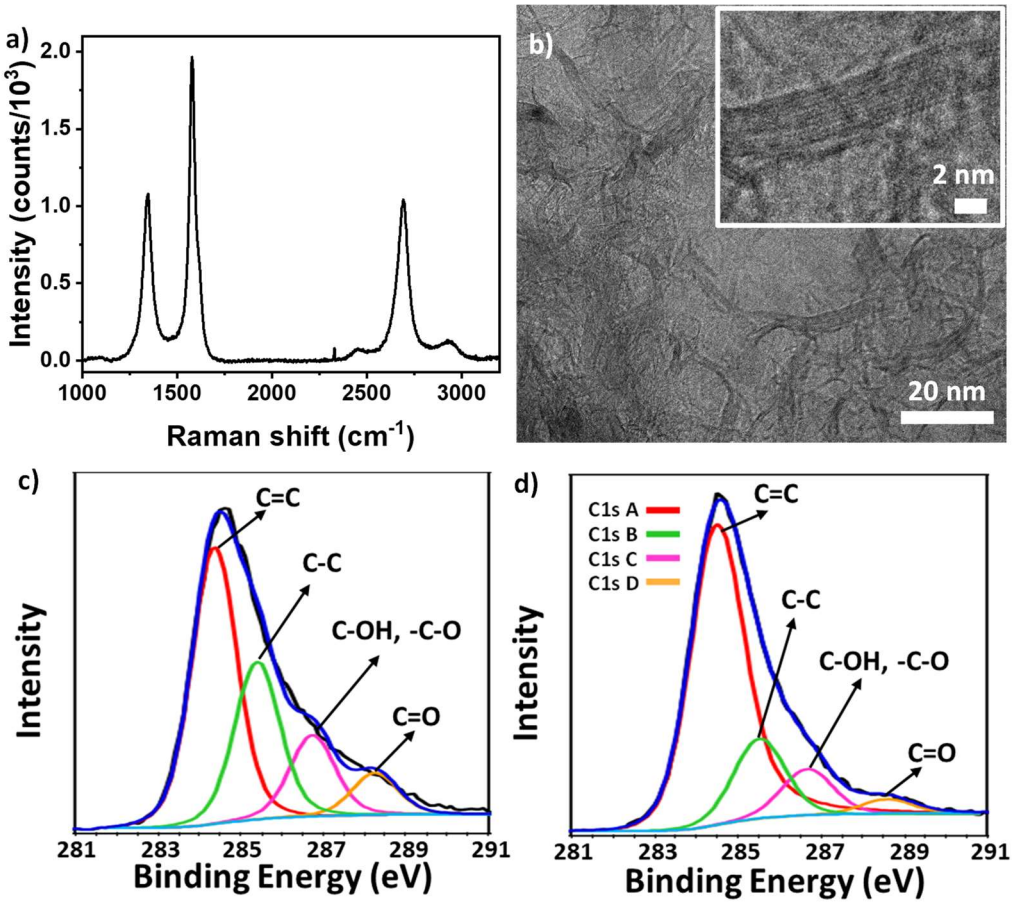


Figure 5.5 a) Representative Raman spectrum of cork-LIG electrode; **b)** TEM image of cork-LIG surface; **c)** C1S XPS spectrum of raw cork; **d)** C1S XPS spectrum of cork-LIG.

Table 5.2 Summary of XPS analysis of raw cork sample, LIG on cork, and reduced cork-LIG.

Peak	**Atomic Percentages (%)**			**Assignments**
	Cork	**Cork-LIG**	**Activated cork-LIG**	
C1s A	42.3	61	78.7	C-C sp^2
C1s B	12.4	8.4	2.1	C-O(H), C-O
C1s C	6.4	2.6		C=O, O-C=O
C1s D	24.1	14.6	10	C-C sp^3
O1s A	9.1	5.3	3.5	C-O
O1s B	2.7	3.8	2.7	O=C-O, H2O
O1s C	1.9	2.9	2.0	O-H
N1s	2			N-C
Total C	85.1	86	90.8	
Total O	13.7	12	8.2	
C1s A/(B+C+D)	0.99	2.38	6.25	
C1s A/O	3.13	5	10	
D-Parameter (eV)	14.5	14	15	

TLM measurements are displayed in Figure 5.6 a. The channel resistance versus track length data averaged from 7 TLM devices is shown. Sheet resistance, R_{SH}, of 10.8 Ω sq^{-1} was calculated by linear regression. This value is as low as has been reported for LIG on natural substrates (see Table 5.3).

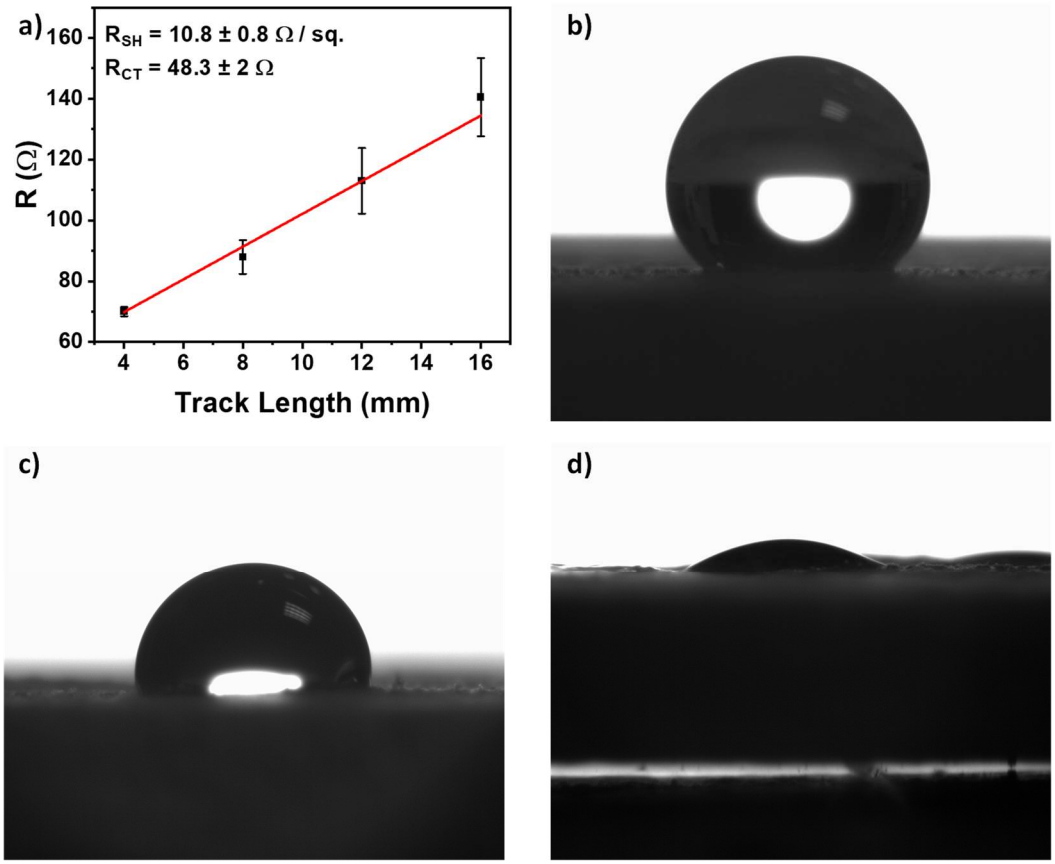


Figure 5.6 a) TLM measurements. Error bars are standard error of n = 7 measurements; contact angle measurement of **b)** raw cork; **c)** cork-LIG; **d)** electrochemically pre-treated cork-LIG.

The quality of LIG material obtained by graphitization of PI and lignin-rich substrates is compared in Table 5.3. The sheet resistance (R_{sh}) reported here was comparable or lower than the resistance calculated for most fabricated structures and lower than the R_{sh} reported for cork graphitized by UV laser. When comparing with other natural materials, pre-treatments should be noted for [12], [44] (both sprayed with flame retardant 'AntiFlame'), [45] (wax coating), [46] (FeCl3 coating), and [21] (sodium borate pre-treatment and wax coating).

Table 5.3 Comparison of LIG derived from natural material.

Material	Laser	Raman (D/G)	Raman (2D/G)	Depth (μm)	R_{sh} (Ω sq^{-1})	Ref.
Polyimide	IR	0.5		30	23	[8]
Paper	UV				125	[12]
Wood	IR	0.8	0.5	800	10	[16]
Watercolour paper	IR	1			40	[46]
Filter Paper	IR	1			40	[44]
Chromatography paper	IR	0.5			32	[14]
Chromatography paper	IR	1.28	0.62	10–30	56	[21]
Cellulose nanofibers	IR			70	16000	[13]
Paper cardboard	IR	0.7		300		[15]
Agglomerated Cork	IR			300	115	[28]
Agglomerated Cork	IR	0.5	0.5	100	10	[45]
Agglomerated Cork	UV		0.37	140	75	[27]
Natural Cork	450 nm	1	0.37		46	[26]
Natural Cork	450 nm	0.8	0.9	500 - 680	10.8	This work

5.4.4 Electrochemical characterisation

The electrochemical properties of the fabricated electrodes were investigated by using the $[Fe(CN)_6]^{3-/4-}$ redox mediator probe. The 3-electrode sensor shown in Figure 5.2b was used for all measurements. While performing this characterization, drastic changes were observed during 10 minutes of $[Fe(CN)_6]^{3-/4-}$ cycling. Figure 5.7a shows 50 CV scans taken at 200 mV s^{-1} scan rate on a cork-LIG electrode, with the 1st and 50th scan highlighted. A reduction of ca. 4 times was observed in the ΔE_P value, from ~ 500 mV for scan 1 to <130 mV for scan 50, as well as an increase in peak current of ca 2.5 times (from 47 μA for cycle 1 to 119 μA for cycle 50). Figure 5.7b shows the changes of ΔE_P and I_P observed for 300 CV cycles. The ΔE_P values sharply dropped during the first 50 cycles and showed small fluctuations thereafter. The I_P values sharply increased during the first 50 cycles and contined to increase at a lower rate for

susequent cycles. In order to decide at what stage of this cycling activation process to stop, CVs at varying scan rates (50 – 1000 mV s^{-1}) were taken at the 50th and 100th cycle. The increase of I_P beyond cycle 50 was not accompanied by an equivalent improvement in the kinetic qualities. Therefore, an activation period of 10 min (50 cycles) was deemed sufficient for the electrode to achieve optimal kinetic performance, and satisfactory I_P responses. Also, longer activations times may be associated with electrode degradation as the analyte penetrates the porous material (observed in practice).

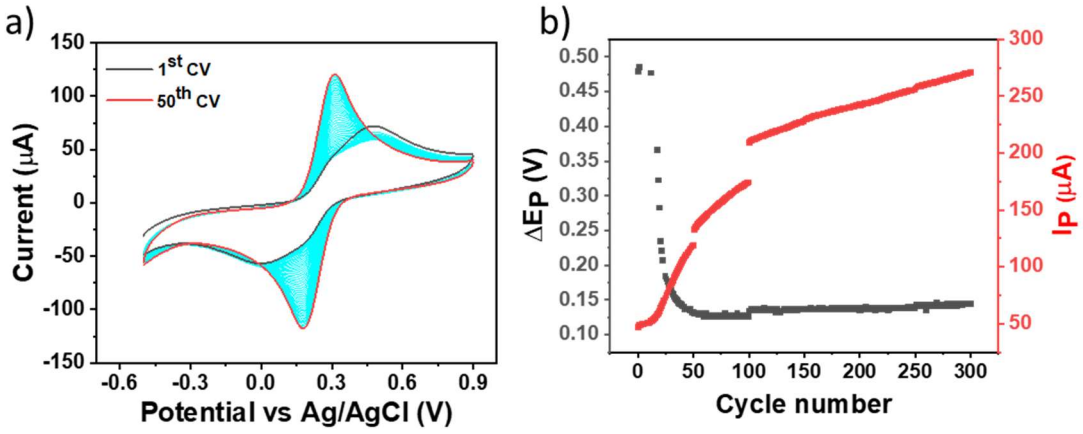


Figure 5.7 a) 50 CV scans (1st and 50th highlighted) measured on cork-LIG electrodes using $[Fe(CN)_6]^{3-/4-}$ (5 mM, 1 M KCl) at 200 mV s^{-1}; **b)** Peak separation and current intensities measured for 300 CV cycles

The reason for the improved electrochemical performance was investigated by observing the potential which triggered the activation. Figure 5.8 a – d shows sets of 10 CVs of $[Fe(CN)_6]^{3-/4-}$ performed at the same electrode, with the low potential incremented by -0.2 V each time. Importantly, each potential range includes the oxidation and reduction potentials for $[Fe(CN)_6]^{3-/4-}$; however, no peaks begin to be seen until the potential window reaches a low potential of -0.6 V. Figure 5.8 d shows 50 CVs of 1 M KCl at 200 mV/s. A reduction peak at ~ -0.4 V is highlighted by a red circle. This has previously been ascribed to the reduction of surface oxygen at LIG electrodes.[47] The CVs of $[Fe(CN)_6]^{3-/4-}$ in Figure 5.8 f were taken immediately after

the cycling in KCl, and displaed sharp peaks without additional activation time. This shows the improved performance is due to the reduction of surface oxygen, rather than any effect directly related to the redox cycling of $[Fe(CN)_6]^{3-/4-}$. For all subsequent measurements, a solution of 1 M KCl was used for the activation treatment.

Figure 5.8g shows a typical set of CV measurements in $Fe(CN)_6]^{3-/4-}$ at varying scan rates obtained after the 10 min activation process. Remarkably, even at rapid scan rates of 1 V s^{-1}, ΔE_P values of < 200 mV were maintained. The formal potential ($E_{1/2}$) for $Fe(CN)_6]^{3-/4-}$ was found to be 231 mV for the 3-electrode planar system, with standard deviation of 4 mV over 55 measurements. The low deviation indicates the stability of the Ag/AgCl paste RE. Compared with the same redox couple in the same system measured with an external electrode, there was a 36 mV potential shift ($E_{1/2}$ = 267 mV). The average ΔE_P calculated at 100 mV s^{-1} scan rate over four electrodes was 90 mV (± 4 mV), indicating a quasi-reversible reaction with fast HET rates.

XPS analysis was carried out on the pre-treated cork-LIG electrode in order to elucidate the mechanism behind the observed electrochemical activation process. Figure 5.8h shows the deconvoluted C1s XPS spectrum of the pre-treated cork-LIG. The C1sA peak dominated the spectrum, as already observed for the pristine cork and the raw cork-LIG samples (see Figure 5.5 c, d; Table 5.2). However, the atomic percentage assigned to the C1sA peak increased from 61 % measured for cork-LIG to 78.7 % measured for pre-treated cork-LIG, suggesting a large relative increase in C=C bonding following the pre-treatment. The ratio of the A peak to other carbon peaks more than doubled and the oxygen content decreased by almost a third. It is clear that the electrochemical treatment was accompanied by a stark improvement in graphene quality. The C1s-B, -C and -D peaks (see Table 5.2), which all relate to forms of C-O bonding, were considerably reduced, in line with the electrochemical reduction of

surface oxygen. The need for a reduction/activation treatment has been reported for LIG electrodes fabricated from polyimide, and was associated to the impurities of LIG derived from the decomposition process and ambient temperature.[47]

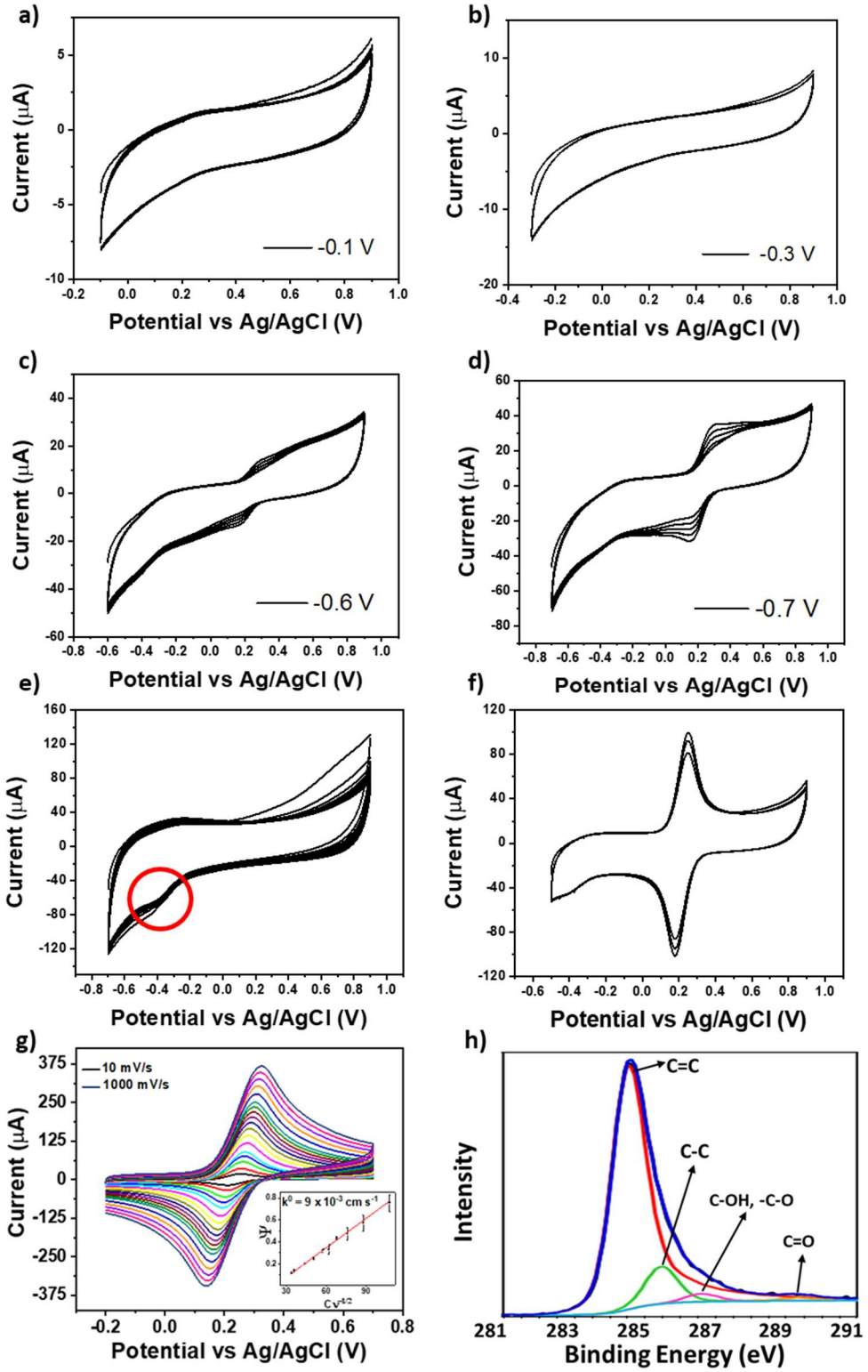


Figure 5.8 10 CV cycles of $[Fe(CN)_6]^{3-/4-}$ 5 mM in 1 M KCl with high potential border of 0.9 V and low potential of **a)** -0.1 V **b)** –0.3 V **c)** –0.6 V **d)** -0.7 V; **e)** 50 CV scans of 1 M KCl with oxygen reduction peak highlighted by a red circle; **f)** CV of $[Fe(CN)_6]^{3-/4-}$ 5 mM in 1 M KCl after activation of (e); **g)** CV of $[Fe(CN)_6]^{3-/4-}$ pre-treated cork-LIG electrode at varying scan rate from 10 mV s^{-1} to 1 V s^{-1}. Inset: calculation of k^0 for n = 5 electrodes; **h)** C1s XPS spectrum of pre-treated cork-LIG electrode after 10 minutes $Fe(CN)_6]^{3-/4-}$ cycling.

The effect of using an electrode with such a porous structure as revealed by SEM (Figure 5.4) was investigated. Figure 5.9a shows a set of CVs of ferrocyanide with ν varying from 1 – 750 mV s^{-1}. At low scan rates (< 50 mVs^{-1}) peak separation values below the reversible limit (59 mV for a one electron reaction) were observed for numerous electrodes, as shown in Figure 5.9b, where the dotted red line indicates the theoretical minimum. These results on a porous electrode suggest that a thin layer mechanism, resulting from electrolyte trapped within the porous network, occurs in parallel with the bulk semi-infinite linear diffusion regime operating at the surface. Indeed, the peak current behaviour in the low scan rate region suggested a thin-layer contribution, where the peak current was linear with the scan rate (Figure 5.9c). For semi-infinite linear diffusion, peak currents was proportional to the square root of the scan rate. This was the dominant mechanism at ν > 50 mVs^{-1}, and the contribution of the thin layer mechanism did not perturb the expected peak current response (Figure 5.9d). Lyons et al. explained such scan rate dependant behaviour by reasoning that high scan rates there is not enough time for diffusion through the pores of the electrode and hence no significant contribution from thin layer behaviour; at low scan rates, there is a significant contribution from species diffusing within the electrode structure.[48] In general, plots of peak anodic and cathodic current *vs* square root of scan rate across a wide range of scan rates above 50 mV s^{-1} displayed excellent linearity, in line with the Randles-Ševčík equation and indicating the dominant semi-infinite linear diffusion regime. Streeter et al. have investigated similar effects on glassy carbon electrodes modified with carbon nanotubes, where analyte can become

trapped between nanotubes and exhibit thin layer behaviour.[49] They have warned against interpreting low peak separation values solely in terms of improved catalytic effects or kinetics. The thin-layer mechanism must be taken into account. In the literature on LIG devices, this effect is not commonly investigated. Hence, for a comparison with literature, a value of the heterogeneous electron transfer kinetic constant (k^0_{app}) must be calculated. For this we have restricted the data used to the high scan rate region (100 – 1000 mVs^{-1}) where the semi-infinite linear diffusion regime dominates.

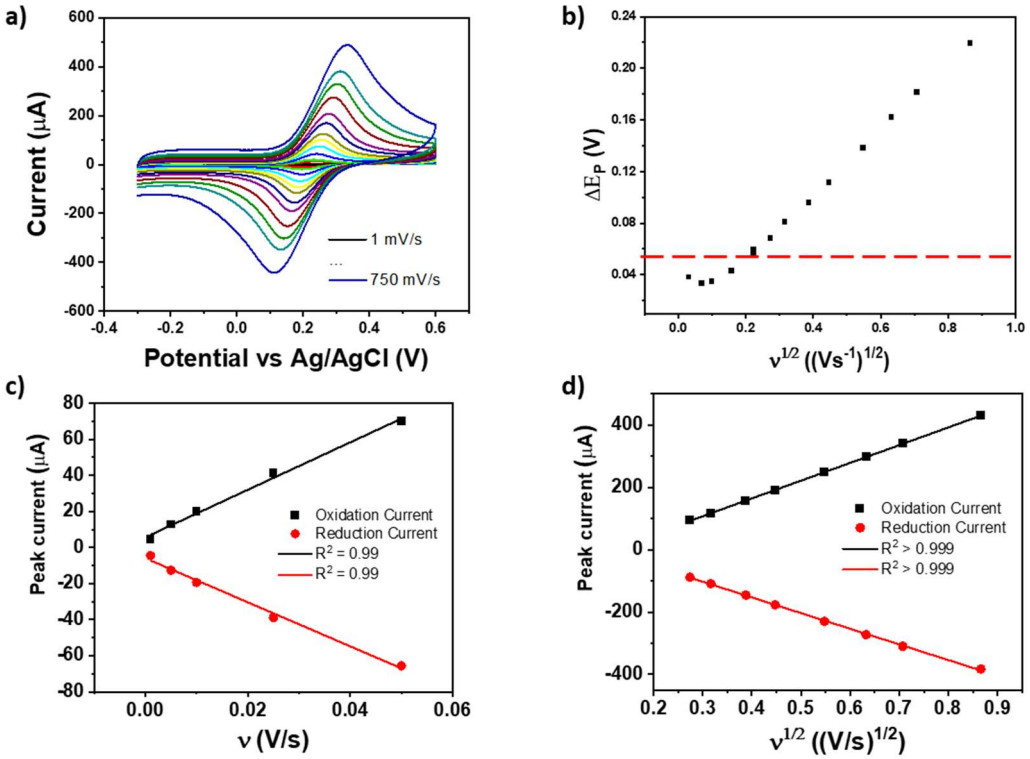


Figure 5.9 a) Set of CV curves of with varying scan rate; **b)** peak separation with scan rate. Dotted line indicates theoretical minimum ΔE_P; **c)** low scan rate CVs with ΔE_P below theoretical minimum; **d)** peak current linear plot with scan rate; **e)** peak current linear plot with square root of scan rate.

From the ΔE_P values, k^0_{app}, was calculated by the Nicholson method.[29] The value calculated for these cork-LIG electrodes was 9×10^{-3} cm s^{-1}. Table 5.4 reports the electrochemical characteristics of cork-LIG in comparison with other LIG electrode

materials obtained by direct laser writing of sustainable substrates and benchmarked against PI-LIG. The cork-LIG exhibited the lowest ΔE_P of the natural LIGs. The k^0_{app} was one order of magnitude higher than the value calculated for filter paper. In comparison with polyimide LIG electrodes previously obtained in our group with other hobbyist lasers (450 nm and 405 nm), the cork-LIG displayed comparable ΔE_P but lower HET rate.

Table 5.4 Electrochemical performance of LIG produced from various precursors and by various lasers using $[Fe(CN)_6]^{3-/4}$**.** ΔE_P values quoted at scan rates varying between 50 – 150 mV s^{-1} and at 100 mV s^{-1} for this work.

Material	Laser	ΔE_P (mV)	k^0_{app} (cm s^{-1})	Ref.
Filter paper	IR (10.6 µm)		7.8×10^{-4}	[44]
Office paper	IR (10.6 µm)	>700	4.08×10^{-4}	[21]
Chromatography paper	IR (10.6 µm)	370	6.85×10^{-4}	[21]
Chitosan	IR (10.6 µm)	290		[18]
Polyimide	Visible (450 nm)	61	1.26×10^{-1}	[11]
Polyimide	UV (405 nm)	86	1.3×10^{-2}	[10]
Cork	Visible (450 nm)	90	9×10^{-3}	This work

Surface wettability was measured by contact angle. The results of the raw cork, cork-LIG, and electrochemically pre-treated cork-LIG are shown in Figure 5.6 b – d. Both the raw cork and the cork-LIG surfaces were found to be hydrophobic, with contact angles of 124.5° and 107.5° respectively. After electrochemical pre-treatment of the surface a contact angle of 29° was measured. A more hydrophilic surface is desirable for electrochemical applications, as analyte gaining access to the high surface-area, porous LIG structure would result in enhanced current responses. Because the electrochemical pre-treatment resulted in a lowering of the oxygen content, it is understood that the improvement in wettability is due to the removal of surface residues from the lasing process.

5.4.5 Tyrosine detection

Tyrosine (Tyr) is a small but important electrochemically active amino acid involved in the regulation of dopamine, adrenaline and thyroid hormones. Although Tyr is a

non-essential amino acid, its imbalance has been associated with the development of serious illnesses, including eating disorders, liver diseases and tyrosinemia.[50-52] Due to its relevance in brain signalling and in the production of stress hormones, it is important to develop rapid, accurate and low cost methods for monitoring of Tyr levels in biological fluids.

The three-electrode device, after 10 minutes of pre-treatment, was used for Tyr detection without modification. Sodium acetate buffer (ABS), 0.01 M, was chosen as the supporting electrolyte for initial measurements, as the Tyrosine oxidation peak was shifted away from the hydrolysis at ~1 V. Figure 5.10a shows a typical set of square wave voltammetry (SWV) scans for varying Tyr concentrations between 5 and 250 μM. The Tyr peak was centred around 670 mV. Peak current was found to increase linearly with Tyr concentration in the range 5 – 150 μM, as shown in Figure 5.10b. From this analysis the sensitivity of the device was calculated at 8.7 $x10^{-3}$ μA/μM, with an LOD of 4.8 μM by the 3σ/m method. Given that Tyr levels in sweat are known to range from 70 to >200 μM, and in urine from 60 to 130 μM, this is a useful dynamic range.[53] Since Uric acid (UA) is found in most biofluids alongside Tyr, the effect of UA's presence in solution with Tyr was investigated. Figure 5.10c shows SWV scans of varying concentration Tyr (5 – 250 μM) in presence of constant UA concentration (50 μM). UA detection was characterised by a peak centred at 300 mV, which did not interfere in the monitoring of Tyr, whose peak remained centred at 670 mV. A linear calibration curve was obtained, as shown in Figure 5.10d, with sensitivity of 8.2 $x10^{-3}$ μA/μM, in excellent agreement with the value measured in absence of UA. Next, SWQ scans were taken of varying Tyr and UA concentrations. Figure 5.10e shows the increase in intensity for the peak centred at as UA concentrations varied between 5 and 250 μM. The scans also showed the parallel increase in peak intensity for Tyr

concentrations between 5 and 250 μM. A linear calibration (Figure 5.10f) was obtained for Tyr, showing the reaction of UA to not be a competing or interfering reaction.

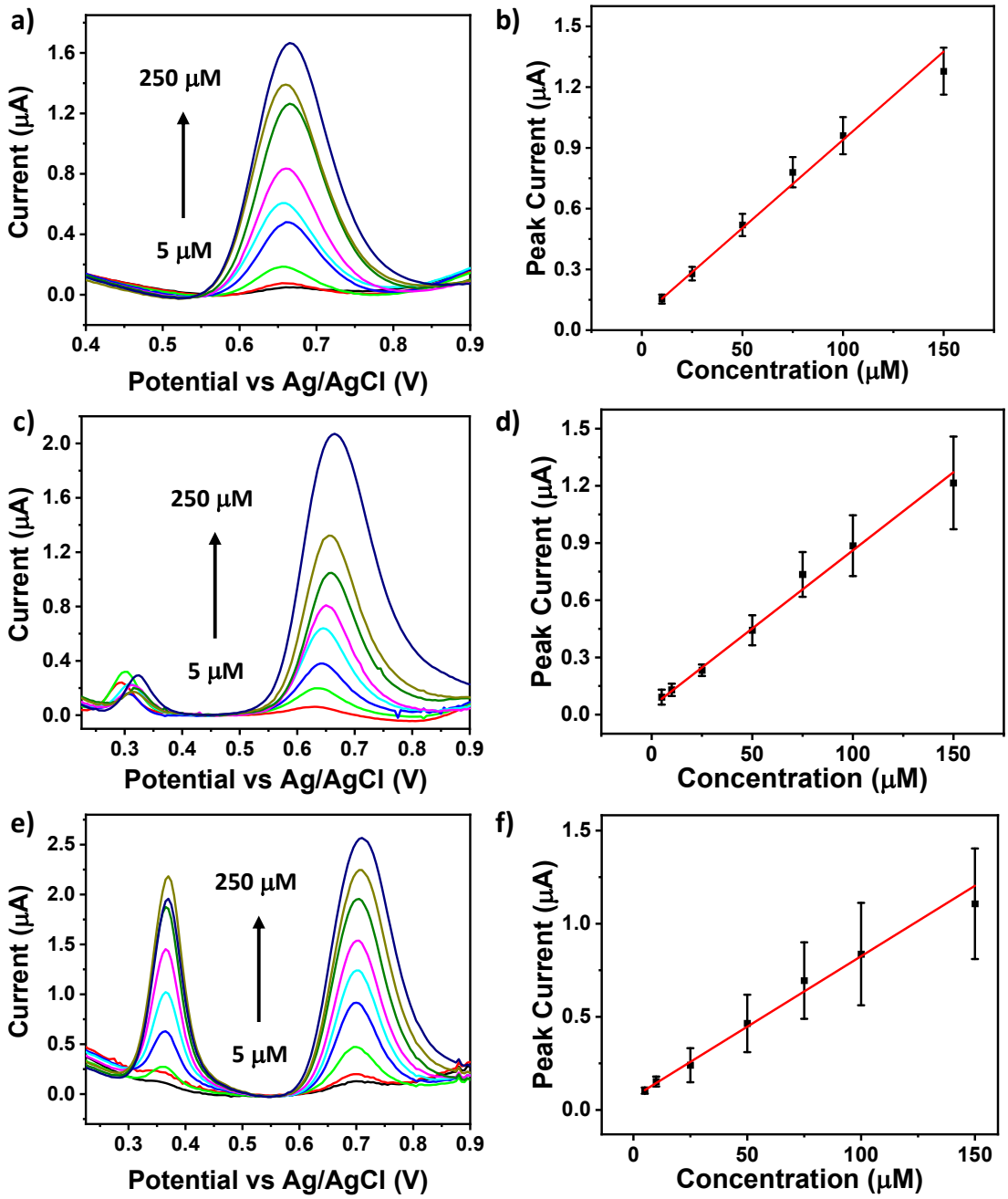


Figure 5.10 a) Typical set of SWV measurements for various Tyr concentrations; **b)** calibration plot; **c)** Detection of Tyr in the presence of 50 μM UA; **d)** linear calibration plot for Tyr in 50 μM UA; **e)** simultaneous variation of UA and Tyr concentration; **f)** linear calibration plot for Tyr. n = 3 devices for all calibrations.

An individual calibration for DA was performed, shown in Figure 5.11. A LOD of 1.1 μM was determined. This value is lower than that reported for LIG produced from commercial polyimide.[11] Dopamine was detected with a logarithmic relation between

concentration and current with a dynamic range of 1 – 100 μM. The calculated sensitivity was 2.8 μA/log(μM).

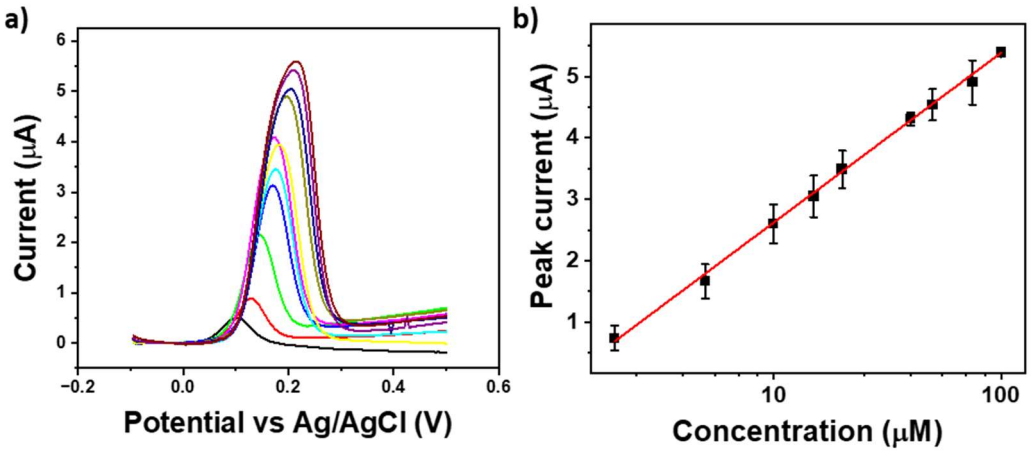


Figure 5.11 a) SWVs recorded for 1 - 100 μM DA; **b)** calibration plot for DA.

The selectivity of the cork-LIG electrode towards Tyr was evaluated by taking SWV scans of Tyr in the presence of UA, Urea, Glucose, dopamine (DA) and ascorbic acid (AA) at biologically relevant concentration levels (50 μM UA, 10 mM Urea, 150 μM Glucose, 25 μM DA, 50 μM AA).[53] Figure 5.12a shows that DA, UA and Tyr displayed well separated and well-defined peaks, centred at 180, 330 and 670 mV respectively. No peaks for urea, glucose or AA appeared. The Tyr peak intensity is in line with the previous calibrations. The cork-LIG electrochemical platform allowed simultaneous detection of DA, UA and Tyr within a narrow potential window, owing to the fast electron transfer kinetics of the material. It is difficult to assign the individual detections to any catalytic activity due to surface groups, as the activation step effectively removes these – as revealed by XPS.

Finally, the applicability of the cork-LIG electrochemical sensor for the determination of Tyr was tested in artificial sweat. The matrix of the artificial sweat was prepared with slight changes according to literature.[54, 55] Artificial sweat contained NaCl (20 g L^{-1}), NH_4Cl (17.5 g L^{-1}), lactic acid (15 g L^{-1}), acetic acid (5 g L^{-1}), ascorbic acid (10 μM), uric acid (60 μM) and urea (10 mM). The pH was adjusted

to 8.1 using KOH, to negatively shift the Tyr peak potential, so that hydrolysis at 1V does not interfere with the measurement. [54] The current responses of the cork-LIG electrochemical sensor were recorded for different Tyr concentrations in artificial sweat, as shown in Figure 5.12b. Linear calibration was achieved from 5 – 250 μM (Figure 5.12c). Comparing the slopes of both calibration curves of the Tyr sensor in ABS (8.7 A M^{-1}**)** and artificial sweat (1.8 x 10^{-2} AM^{-1}), more sensitive detection was achieved in the sweat solution. The LOD in the sweat solution was 3.75 μM. Considering the normal Tyr level in sweat (60 - 300 μM), the proposed electrochemical sensor could be an excellent candidate for the development of both disposable and wearable environmentally friendly diagnostic devices. Table 5.5 compares the Tyr detection of the cork-LIG electrode with other published electrochemical platforms. The reported LOD of 3.75 μM is comparable with the LODs reported for PI-LIG, showing that environmentally friendly substrates can be exploited as precursors to high-quality LIG electrochemical sensors.

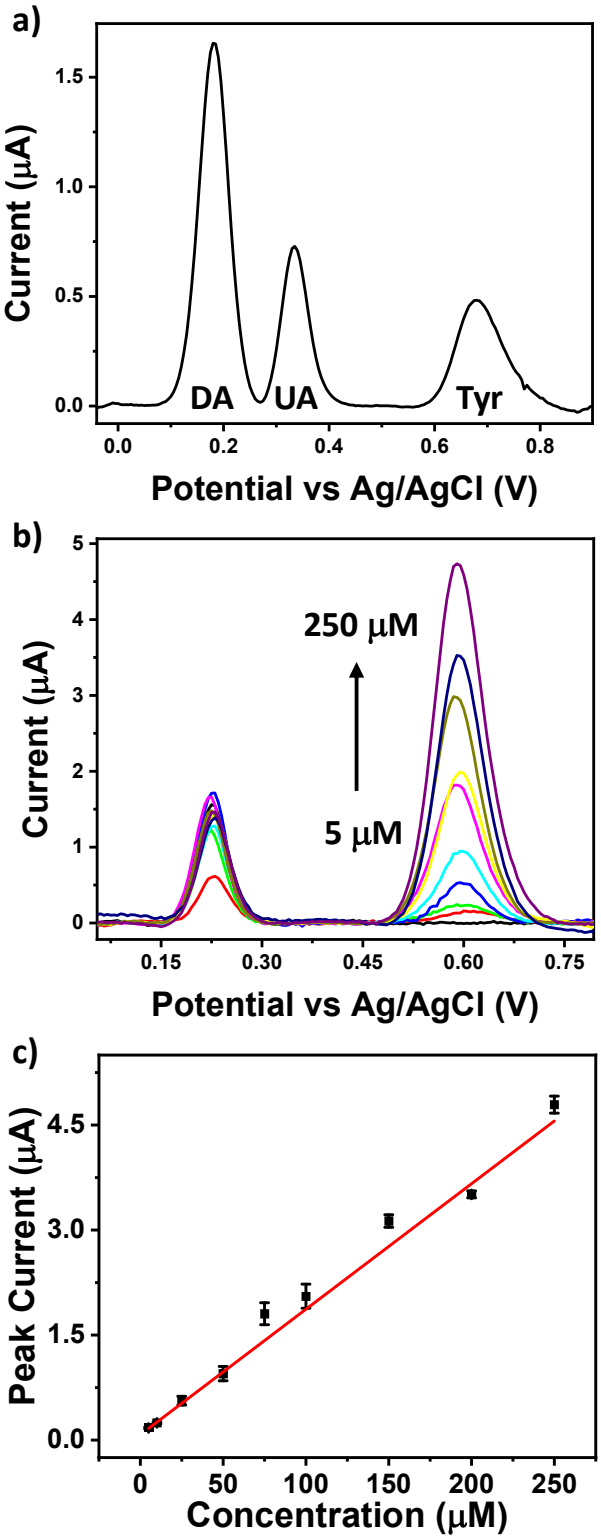


Figure 5.12 a) Detection of 50 μM Tyr in the presence of 50 μM Uric Acid, 10 mM Urea, 150 μM Glucose, 25 μM DA, 50 μM AA; **b)** SWV plots of varying Tyr concentration in artificial sweat solution; **c)** linear calibration plot of b) for n = 3 devices.

Table 5.5 Tyr detection by different electrode materials

Material	LOD (M)	Sensitivity	Reference
PI-LIG	1.5×10^{-6}		[56]
PI-LIG	3.6×10^{-6}	0.61 μM cm^{-2}	[57]
rGO–Cu modified pencil graphite	1×10^{-7}	0.4 μA ppm^{-1} mm^{-2}	[58]
GR/Au NPs/GCE	47×10^{-9}		[59]
rGO/ABPE	0.06×10^{-6}	3.314 μA $μM^{-1}$ cm^{-2}	[60]
Egr/GC	1.81×10^{-6}	1.24×10^{-2} A M^{-1}	[61]
Cork-LIG	3.75×10^{-6}	1.8×10^{-2} A M^{-1}	This work

5.5 Conclusions

Novel electrochemical sensors were fabricated by direct laser writing of natural cork from Quercus suber L. The cork-LIG structures displayed a porous, 3D, high surface area morphology, suitable for electrochemical applications. Three terminal electrode sensors were fabricated in less than 10 min, using cork-LIG as working and counter electrode and Ag/AgCl paste as reference electrode. Following a 10 min electrochemical activation process in $[Fe(CN)_6]^{3-/4}$, the cork-LIG electrodes displayed an average ΔE_P of 90 mV at a scan rate of 100 mV s^{-1}, close to the ideal value for a reversible reaction.[62] The HET kinetics were found to be one order of magnitude higher than other LIG electrodes obtained from wood and/or lignin rich natural substrates. The electrochemical sensors showed excellent sensing performance. Dopamine was detected with an LOD of 1.1 μM. Sensitive detection of Tyr in an artificial sweat solution was achieved with LOD of 3.75 μM. Here we have presented a natural material, entirely renewable, recyclable, whose electrical and electrochemical properties rival those of the highest quality LIG. This is exemplified by the simultaneous detection of DA, UA and Tyr in a narrow potential window, and the sensitive detection in sweat. We can consider the Tyr detection and characterisation a showcase of the capabilities of a new and exciting form of LIG sensor. A wide range

of sensing applications are made possible by the rapid electron transfer rates at the cork-LIG electrode. This study shows the suitability of cork as natural and abundant precursor material for the realization of next generation green electronics.

5.6 References

1. Silva, S.P., M.A. Sabino, E.M. Fernandes, V.M. Correlo, L.F. Boesel, and R.L. Reis, *Cork: properties, capabilities and applications.* International Materials Reviews, 2005. **50**(6): p. 345-365.
2. White, R.H., *Effect of Lignin Content and Extractives on the Higher Heating Value of Wood.* Wood and Fiber Science, 1987. **19**(4): p. 446 - 452.
3. Crouvisier-Urion, K., J. Chanut, A. Lagorce, P. Winckler, Z. Wang, P. Verboven, B. Nicolai, J. Lherminier, E. Ferret, R.D. Gougeon, J.P. Bellat, and T. Karbowiak, *Four hundred years of cork imaging: New advances in the characterization of the cork structure.* Sci Rep, 2019. **9**(1): p. 19682.
4. Duarte, A.P. and J.C. Bordado, *Cork – A Renewable Raw Material: Forecast of Industrial Potential and Development Priorities.* Frontiers in Materials, 2015. **2**.
5. Griffiths, K., C. Dale, J. Hedley, M.D. Kowal, R.B. Kaner, and N. Keegan, *Laser-scribed graphene presents an opportunity to print a new generation of disposable electrochemical sensors.* Nanoscale, 2014. **6**(22): p. 13613-13622.
6. Strong, V., S. Dubin, M.F. El-Kady, A. Lech, Y. Wang, B.H. Weiller, and R.B. Kaner, *Patterning and electronic tuning of laser scribed graphene for flexible all-carbon devices.* ACS Nano, 2012. **6**(2): p. 1395-403.
7. Ye, R., D.K. James, and J.M. Tour, *Laser-Induced Graphene.* Accounts of Chemical Research, 2018. **51**(7): p. 1609-1620.
8. Lin, J., Z. Peng, Y. Liu, F. Ruiz-Zepeda, R. Ye, E.L. Samuel, M.J. Yacaman, B.I. Yakobson, and J.M. Tour, *Laser-induced porous graphene films from commercial polymers.* Nat Commun, 2014. **5**: p. 5714.
9. Nayak, P., N. Kurra, C. Xia, and H.N. Alshareef, *Highly Efficient Laser Scribed Graphene Electrodes for On-Chip Electrochemical Sensing Applications.* Advanced Electronic Materials, 2016. **2**(10): p. 1600185.
10. Burke, M., C. Larrigy, E. Vaughan, G. Paterakis, L. Sygellou, A.J. Quinn, G. Herzog, C. Galiotis, and D. Iacopino, *Fabrication and Electrochemical Properties of Three-Dimensional (3D) Porous Graphitic and Graphenelike Electrodes Obtained by Low-Cost Direct Laser Writing Methods.* ACS Omega, 2020. **5**(3): p. 1540-1548.
11. Vaughan, E., C. Larrigy, M. Burke, L. Sygellou, A.J. Quinn, C. Galiotis, and D. Iacopino, *Visible Laser Scribing Fabrication of Porous Graphitic Carbon Electrodes: Morphologies, Electrochemical Properties, and Applications as Disposable Sensor Platforms.* ACS Applied Electronic Materials, 2020. **2**(10): p. 3279-3288.

12. Kulyk, B., B.F.R. Silva, A.F. Carvalho, P. Barbosa, A.V. Girão, J. Deuermeier, A.J.S. Fernandes, F.M.L. Figueiredo, E. Fortunato, and F.M. Costa, *Laser-Induced Graphene from Paper by Ultraviolet Irradiation: Humidity and Temperature Sensors.* Advanced Materials Technologies, 2022. **7**(7): p. 2101311.
13. Lee, S. and S. Jeon, *Laser-Induced Graphitization of Cellulose Nanofiber Substrates under Ambient Conditions.* ACS Sustainable Chemistry & Engineering, 2019. **7**(2): p. 2270-2275.
14. Kulyk, B., B.F.R. Silva, A.F. Carvalho, S. Silvestre, A.J.S. Fernandes, R. Martins, E. Fortunato, and F.M. Costa, *Laser-Induced Graphene from Paper for Mechanical Sensing.* ACS Appl Mater Interfaces, 2021. **13**(8): p. 10210-10221.
15. de Araujo, W.R., C.M.R. Frasson, W.A. Ameku, J.R. Silva, L. Angnes, and T.R.L.C. Paixão, *Single-Step Reagentless Laser Scribing Fabrication of Electrochemical Paper-Based Analytical Devices.* Angewandte Chemie International Edition, 2017. **56**(47): p. 15113-15117.
16. Ye, R., Y. Chyan, J. Zhang, Y. Li, X. Han, C. Kittrell, and J.M. Tour, *Laser-Induced Graphene Formation on Wood.* Advanced Materials, 2017. **29**(37): p. 1702211.
17. C. Claro, P.I., T. Pinheiro, S.L. Silvestre, A.C. Marques, J. Coelho, J.M. Marconcini, E. Fortunato, L.H. C. Mattoso, and R. Martins, *Sustainable carbon sources for green laser-induced graphene: A perspective on fundamental principles, applications, and challenges.* Applied Physics Reviews, 2022. **9**(4): p. 041305.
18. Larrigy, C., M. Burke, A. Imbrogno, E. Vaughan, C. Santillo, M. Lavorgna, L. Sygellou, G. Paterakis, C. Galiotis, D. Iacopino, and A.J. Quinn, *Porous 3D Graphene from Sustainable Materials: Laser Graphitization of Chitosan.* Advanced Materials Technologies, 2022. **n/a**(n/a): p. 2201228.
19. Awasthi, H., U.S. Jayapiriya, H. Renuka, M.D. Wagh, A. Kothuru, A.K. Srivastava, and S. Goel, *Flexible Paper and Cloth Substrates with Conductive Laser Induced Graphene Traces for Electroanalytical Sensing, Energy Harvesting and Supercapacitor Applications.* IEEE Sensors Journal, 2022: p. 1-1.
20. Chyan, Y., R. Ye, Y. Li, S.P. Singh, C.J. Arnusch, and J.M. Tour, *Laser-Induced Graphene by Multiple Lasing: Toward Electronics on Cloth, Paper, and Food.* ACS Nano, 2018. **12**(3): p. 2176-2183.
21. Pinheiro, T., S. Silvestre, J. Coelho, A.C. Marques, R. Martins, M.G.F. Sales, and E. Fortunato, *Laser-Induced Graphene on Paper toward Efficient Fabrication of Flexible, Planar Electrodes for Electrochemical Sensing.* Advanced Materials Interfaces, 2021. **8**(22): p. 2101502.
22. Park, H., M. Kim, B.G. Kim, and Y.H. Kim, *Electronic Functionality Encoded Laser-Induced Graphene for Paper Electronics.* ACS Applied Nano Materials, 2020. **3**(7): p. 6899-6904.
23. Dreimol, C.H., H. Guo, M. Ritter, T. Keplinger, Y. Ding, R. Günther, E. Poloni, I. Burgert, and G. Panzarasa, *Sustainable wood electronics by iron-catalyzed laser-induced graphitization for large-scale applications.* Nat Commun, 2022. **13**(1): p. 3680.

24. Le, T.-S.D., Y.A. Lee, H.K. Nam, K.Y. Jang, D. Yang, B. Kim, K. Yim, S.-W. Kim, H. Yoon, and Y.-J. Kim, *Green Flexible Graphene–Inorganic-Hybrid Micro-Supercapacitors Made of Fallen Leaves Enabled by Ultrafast Laser Pulses.* Advanced Functional Materials, 2022. **32**(20): p. 2107768.
25. Lee, J.S., H.J. Lee, J.M. Yoo, T. Kim, and Y.H. Kim, *High-Performance Field Emission from a Carbonized Cork.* ACS Applied Materials & Interfaces, 2017. **9**(50): p. 43959-43965.
26. Imbrogno, A., J. Islam, C. Santillo, R. Castaldo, L. Sygellou, C. Larrigy, R. Murray, E. Vaughan, M.K. Hoque, A.J. Quinn, and D. Iacopino, *Laser-Induced Graphene Supercapacitors by Direct Laser Writing of Cork Natural Substrates.* ACS Applied Electronic Materials, 2022. **4**(4): p. 1541-1551.
27. Carvalho, A.F., A.J.S. Fernandes, R. Martins, E. Fortunato, and F.M. Costa, *Laser-Induced Graphene Piezoresistive Sensors Synthesized Directly on Cork Insoles for Gait Analysis.* Advanced Materials Technologies, 2020. **5**(12): p. 2000630.
28. Stanford, M.G., J.T. Li, Y. Chyan, Z. Wang, W. Wang, and J.M. Tour, *Laser-Induced Graphene Triboelectric Nanogenerators.* ACS Nano, 2019. **13**(6): p. 7166-7174.
29. Nicholson, R.S., *Theory and Application of Cyclic Voltammetry for Measurement of Electrode Reaction Kinetics.* Analytical Chemistry, 1965. **37**(11): p. 1351-1355.
30. Konopka, S.J. and B. McDuffie, *Diffusion coefficients of ferri- and ferrocyanide ions in aqueous media, using twin-electrode thin-layer electrochemistry.* Analytical Chemistry, 1970. **42**(14): p. 1741-1746.
31. Murray, R., M. Burke, D. Iacopino, and A.J. Quinn, *Design of Experiments and Optimization of Laser-Induced Graphene.* ACS Omega, 2021. **6**(26): p. 16736-16743.
32. Ferrari, A.C. and J. Robertson, *Interpretation of Raman spectra of disordered and amorphous carbon.* Physical Review B, 2000. **61**(20): p. 14095-14107.
33. Ferrari, A.C. and D.M. Basko, *Raman spectroscopy as a versatile tool for studying the properties of graphene.* Nature Nanotechnology, 2013. **8**(4): p. 235-246.
34. Lespade, P., R. Al-Jishi, and M.S. Dresselhaus, *Model for Raman scattering from incompletely graphitized carbons.* Carbon, 1982. **20**(5): p. 427-431.
35. Nguyen, V.T., H.D. Le, V.C. Nguyen, T.T. Tam Ngo, D.Q. Le, X.N. Nguyen, and N.M. Phan, *Synthesis of multi-layer graphene films on copper tape by atmospheric pressure chemical vapor deposition method.* Advances in Natural Sciences: Nanoscience and Nanotechnology, 2013. **4**(3): p. 035012.
36. Popov, A.M., I.V. Lebedeva, A.A. Knizhnik, Y.E. Lozovik, B.V. Potapkin, N.A. Poklonski, A.I. Siahlo, and S.A. Vyrko, *AA stacking, tribological and electronic properties of double-layer graphene with krypton spacer.* The Journal of Chemical Physics, 2013. **139**(15): p. 154705.
37. Çakmak, G. and T. Öztürk, *Continuous synthesis of graphite with tunable interlayer distance.* Diamond and Related Materials, 2019. **96**: p. 134-139.
38. Periera, H., *Variability of the chemical composition of cork.* BioResources, 2013. **8**(2): p. 2246-2256.

39. Banks, C.E., T.J. Davies, G.G. Wildgoose, and R.G. Compton, *Electrocatalysis at graphite and carbon nanotube modified electrodes: edge-plane sites and tube ends are the reactive sites.* Chemical Communications, 2005(7): p. 829-841.
40. Santos, N.F., S.O. Pereira, A. Moreira, A.V. Girão, A.F. Carvalho, A.J.S. Fernandes, and F.M. Costa, *IR and UV Laser-Induced Graphene: Application as Dopamine Electrochemical Sensors.* Advanced Materials Technologies, 2021. **6**(6): p. 2100007.
41. Yang, R.T. and C. Wong, *Mechanism of Single-Layer Graphite Oxidation: Evaluation by Electron Microscopy.* Science, 1981. **214**(4519): p. 437-438.
42. Wildgoose, G.G., P. Abiman, and R.G. Compton, *Characterising chemical functionality on carbon surfaces.* Journal of Materials Chemistry, 2009. **19**(28): p. 4875-4886.
43. Kaciulis, S., A. Mezzi, S.K. Balijepalli, M. Lavorgna, and H.S. Xia, *Electron spectroscopy of rubber and resin-based composites containing 2D carbon.* Thin Solid Films, 2015. **581**: p. 80-85.
44. Kulyk, B., S.O. Pereira, A.J.S. Fernandes, E. Fortunato, F.M. Costa, and N.F. Santos, *Laser-induced graphene from paper for non-enzymatic uric acid electrochemical sensing in urine.* Carbon, 2022. **197**: p. 253-263.
45. Silvestre, S.L., T. Pinheiro, A.C. Marques, J. Deuermeier, J. Coelho, R. Martins, L. Pereira, and E. Fortunato, *Cork derived laser-induced graphene for sustainable green electronics.* Flexible and Printed Electronics, 2022. **7**(3): p. 035021.
46. Chyan, Y., J. Cohen, W. Wang, C. Zhang, and J.M. Tour, *Graphene Art.* ACS Applied Nano Materials, 2019. **2**(5): p. 3007-3011.
47. Vivaldi, F., A. Dallinger, N. Poma, A. Bonini, D. Biagini, P. Salvo, F. Borghi, A. Tavanti, F. Greco, and F. Di Francesco, *Sweat analysis with a wearable sensing platform based on laser-induced graphene.* APL Bioeng, 2022. **6**(3): p. 036104.
48. Gareth P Keeley, M.E.G.L., *The effects of thin layer diffusion at glassy carbon electrodes modified with porous films of single-walled carbon nanotubes.* International Journal of Electrochemical Science, 2009. **4**(6): p. 794 - 809.
49. Streeter, I., G.G. Wildgoose, L. Shao, and R.G. Compton, *Cyclic voltammetry on electrode surfaces covered with porous layers: An analysis of electron transfer kinetics at single-walled carbon nanotube modified electrodes.* Sensors and Actuators B: Chemical, 2008. **133**(2): p. 462-466.
50. D'Andrea, G., R. Ostuzzi, A. Bolner, F. Francesconi, F. Musco, F. d'Onofrio, and D. Colavito, *Study of tyrosine metabolism in eating disorders. Possible correlation with migraine.* Neurological Sciences, 2008. **29**(1): p. 88.
51. Levine, R.J. and H.O. Conn, *Tyrosine metabolism in patients with liver disease.* J Clin Invest, 1967. **46**(12): p. 2012-20.
52. González-Lamuño, D., P. Sánchez-Pintos, F. Andrade, M.L. Couce, and L. Aldámiz-Echevarría, *Treatment adherence in tyrosinemia type 1 patients.* Orphanet Journal of Rare Diseases, 2021. **16**(1): p. 256.
53. Harvey, C.J., R.F. LeBouf, and A.B. Stefaniak, *Formulation and stability of a novel artificial human sweat under conditions of storage and use.* Toxicology in Vitro, 2010. **24**(6): p. 1790-1796.

54. Callewaert, C., B. Buysschaert, E. Vossen, V. Fievez, T. Van de Wiele, and N. Boon, *Artificial sweat composition to grow and sustain a mixed human axillary microbiome.* J Microbiol Methods, 2014. **103**: p. 6-8.
55. Kilic, T., V. Brunner, L. Audoly, and S. Carrara. *Smart e-Patch for drugs monitoring in schizophrenia*. in *2016 IEEE International Conference on Electronics, Circuits and Systems (ICECS)*. 2016.
56. Matias, T.A., R.G. Rocha, L.V. Faria, E.M. Richter, and R.A.A. Munoz, *Infrared Laser-Induced Graphene Sensor for Tyrosine Detection.* ChemElectroChem, 2022. **9**(14): p. e202200339.
57. Yang, Y., Y. Song, X. Bo, J. Min, O.S. Pak, L. Zhu, M. Wang, J. Tu, A. Kogan, H. Zhang, T.K. Hsiai, Z. Li, and W. Gao, *A laser-engraved wearable sensor for sensitive detection of uric acid and tyrosine in sweat.* Nat Biotechnol, 2020. **38**(2): p. 217-224.
58. Kavitha, C., K. Bramhaiah, and N.S. John, *Low-cost electrochemical detection of l-tyrosine using an rGO–Cu modified pencil graphite electrode and its surface orientation on a Ag electrode using an ex situ spectroelectrochemical method.* RSC Advances, 2020. **10**(39): p. 22871-22880.
59. Liu, M., J. Lao, H. Wang, Z. Xu, J. Li, L. Wen, Z. Yin, C. Luo, and H. Peng, *Electrochemical Determination of Tyrosine Using Graphene and Gold Nanoparticle Composite Modified Glassy Carbon Electrode.* Russian Journal of Electrochemistry, 2021. **57**(1): p. 41-50.
60. Deng, P., J. Xiao, J. Feng, Y. Tian, Y. Wu, J. Li, and Q. He, *Highly sensitive electrochemical sensor for tyrosine detection using a sub-millimeter electrode.* Microchemical Journal, 2021. **165**: p. 106106.
61. Varodi, C., F. Pogăcean, M. Coroş, A. Ciorîță, and S. Pruneanu, *Electrochemical L-Tyrosine Sensor Based on a Glassy Carbon Electrode Modified with Exfoliated Graphene.* Sensors (Basel), 2022. **22**(10).
62. Allen J. Bard, L.R.F., *Electrochemical Methods: Fundamentals and Applications*. 2 ed. 2001: Wiley.

Chapter 6: Summary and Future Work

6.1 Summary of Thesis

The goal of this thesis was to work towards the development of low-cost, sustainable electrochemical sensors of high quality. This research followed a clear trajectory, circumscribed by the following elements: introduction of a low-cost, low-power laser system to work on the well-established LIG precursor polyimide, and perform a full material characterisation including electrochemical performance; develop this material and explore its functionalisation capabilities; move to explore bio-polymer compositions and their prospects for developing a LIG platform; finally, to work on entirely renewable and sustainable natural cork, to investigate this material's potential as a LIG electrochemical sensing platform.

In Chapter 1, an overview of LIG and LIG production was given. It was shown that LIG is versatile material. With a desired application in mind, the fabrication process is readily altered to produce an optimal form of LIG. This was elucidated by a literature review of the processes and applications which have resulted in a wide field of LIG electrochemical sensing research. The field is expanding, with research driven by use of new laser systems, exploration of new applications, and the use of sustainable precursor materials.

In Chapter 2, LIG electrodes were fabricated by a direct laser writing method by using a low-cost hobbyist laser with 450 nm laser illumination. Material qualities were examined by XPS, Raman, SEM and contact angle. The material was found to be porous with a 3D structure, in line with the general characteristics of LIG as produced by other lasing methods. The micro-structure, rich in defects and edge planes, was conducive to good electrochemical sensing capabilities. The HET kinetic rates,

characterised by $[Ru(NH3)_6]^{3+/2+}$ and $[Fe(CN)_6]^{3-/4-}$ redox mediators, were rapid and compared favourably to other carbon electrodes in the literature. The effect of porosity on the ET kinetics was assessed by comparison between geometric area and electrochemically active area, and the possibility of the contribution of such thin layer diffusion mechanisms was explored. Such a contribution was considered to be too small to perturb the dominant diffusion limited mass transfer process. The parasitic effects of working with a highly resistive electrode material were explored, and design solutions found for decoupling the electrode material from the external circuit. These results were crucial for the work of the subsequent chapters. Electrode designs were updated to minimize the contribution of and LIG track as purely a current-carrying element – meaning that the role of LIG was purely as a site for electrochemical reactions to occur. Finally, the LIG electrodes showed excellent biosensing performance and were able to perform electrochemical detection of AA, DA and UA in solution without further electrode modification and by both CV and DPV methods, with a LOD of 5.5 μM for DA.

In Chapter 3, the work of Chapter 2 built upon for developing a LIG sensor for IL6 detection. The LIG surface was shown to be suitable for modification with anti-IL6. Attachment of IL6 caused a shielding effect for the LIG electrode, causing current responses to $[Fe(CN)_6]^{3-/4-}$ to drop proportionally to the log of IL6. The immunosensor was able to detect IL-6 in the linear range 10–500 pg/mL with an LOD of 5.1 pg/mL in PBS. These LIG biosensors maintained a linear current-Log[C] relationship in serum media. The material of this chapter presented the first IL6 LIG electrochemical sensor.

In Chapter 4, a new direction was taken towards a more sustainable LIG. Films based on formulations of the natural bio-polymer Chitosan were used. These films

were successfully converted to a high quality LIG by a range of recipes and laser setting configurations. Multi-step lasing techniques were used for these conversions. The materials were characterised by Raman, XPS and electrical measurements. These results will prove useful for future work of LIG on sustainable materials.

In the final experimental chapter of this thesis, work on sustainable LIG precursors was continued. Natural cork, from Quercus suber L., were treated with the 450 nm laser and turned into LIG structures. Cork-LIG electrodes had not been used before in the literature for chemical sensing. This required the performance of a thorough optimisation process for defining the optimal laser parameters. A material characterisation, similar to the work of Chapter 1 on polyimide, was performed. The cork-LIG structures displayed a porous, 3D, high surface area morphology, though markedly different from PI LIG structures. Three terminal electrode sensors were fabricated in less than a minute, using cork-LIG as working and counter electrode and Ag/AgCl paste as reference electrode. Following a 10 min electrochemical activation process in KCl, the cork-LIG electrodes displayed close to the ideally reversible kinetics. The electrochemical sensors showed excellent sensing performance. Dopamine was detected with a LOD of 1.1 μM. Sensitive detection of Tyr was achieved with LOD of 3.75 μM in artificial sweat solution. In Chapter 5, a natural material, entirely renewable, recyclable was presented, whose electrical and electrochemical properties rival those of the highest quality LIG. As with the detection of DA in Chapter 1, Tyr detection on cork-LIG electrodes is a showcase of the capabilities of a new and exciting form of LIG sensor. A wide range of sensing applications are made possible by the rapid electron transfer rates at the cork-LIG electrode. This chapter shows the suitability of cork as natural and abundant precursor material for the realisation of next generation green electronics.

A comparison of the material properties of the LIG used in the separate chapters of this thesis is provided in Table 6.1. Natural cork-LIG reports the best values in terms of Raman $I_{D/G}$, sp^2 carbon content and sheet resistance – though it should be noted once more that the cork-LIG develops ~500 μm into the material, which improves the conductivity. The polyimide-LIG has the largest Raman $I_{2D/G}$ ratio, as well as the fastest electron-transfer rates for the $[Fe(CN)_6]^{3-/4-}$ reaction.

For device fabrication, the cork electrodes have the added advantage of being self-standing. For polyimide and for chitosan-borax, a rigid substrate is necessary to support the device, glass cover slips being used in both cases. Cork also has several other advantages related to the mechanical properties of the material: for polyimide, the mismatch between the strain of LIG and polyimide itself sometimes causes tears and peels in the material; for chitosan-borax, the film can lacks flexibility, which can lead to cracking. The main material advantage of polyimide over cork is its reproducible surface qualities – cork, being a natural material, with an inconsistent dispersion of lenticels across different samples, which can affect the LIG quality.

Table 6.1 Comparison of material characteristics of LIG derived from polyimide, cork and the chitosan-borax composite. $I_{D/G}$ and $I_{2D/G}$ refer to intensity ratios derived from Raman results; C sp^2 data is from XPS, and DE_P and k^0_{app} refer to the $[Fe(CN)_6]^{3-/4-}$ reaction.

Material	Laser	$I_{D/G}$	$I_{2D/G}$	C sp^2 %	R_{SH}	ΔE_P (mV)	k^0_{app} ($cm\ s^{-1}$)
Polyimide	450 nm	1.2	1.2	62.5	16	61	1.26×10^{-1}
Chitosan-borax	10.6 μm	1.2	0.5	52.8	110	110	4×10^{-3}
Natural Cork	450 nm	0.8	0.9	78.7	10.8	90	9×10^{-3}

In terms of application, our polyimide-LIG has already proven to be a wonderful material for biosensing, as showcased in Chapter 3 of this thesis for IL-6 detection. Additionally, through an external collaboration, we have functionalised this electrode for enzymatic lactate detection, with excellent results (see publication 5 below). In addition to electrochemical sensing, through another external collaboration, we have

used this material to fabricate a highly-sensitive humidity sensor (see publication 3 below). The application of the bare cork-LIG electrode for low LOD dopamine sensing, and tyrosine sensing in an artificial sweat solution provided excellent results.

As seen in Table 6.1 above, the chitosan-borax-LIG lags behind the other forms that we have developed in terms of material quality. As things stand, we are at the very early stages of the development of this material. So far have proven it to be the most exciting material in the class of chitosan-derived-LIG electrochemical sensors.

6.2 Future Work

The results presented in Chapter 2 showcase LIG produced by the low-power 450 nm system as an excellent material for electrochemical sensing. This was continued in Chapter 3, where surface bio-functionalisation of the surface allowed selective and sensitive IL6 detection. Such a procedure can be, and has been, carried out for other biomarkers. For example, in another collaborative work which we have published, we used the 450 nm LIG platform for Lactate detection. This work can be continued, towards an expanding field of LIG bio-sensors. The work of Chapter 2 is not confined to the realm of electrochemical sensing. A humidity sensor was developed, in collaboration with partners at FORTH in Greece, based on a 450 nm LIG interdigitated supercapacitor (publication 2 below). Gas sensing with LIG electrodes is currently being explored within our group.

According to our initial electrochemical characterisation, the chitosan-borax-LIG electrode performs better than any chitosan-based LIG electrodes in literature, and indeed displays faster electron transfer rates than most *green-LIG* sensors in literature (see Table 4.4).

The cork-LIG electrodes present an exciting opportunity to develop a new family of green-electrochemical sensors. The work presented in chapter 5 was performed on

the raw-LIG electrode, and already we are conducting work on a Cu nanoparticle-modified cork-LIG electrode, for enzyme-free electrochemical detection of glucose. These preliminary results are excellent. Similar to what we have done with polyimide-LIG, further functionalisation will be explored to examine the range of application of this material.

For all of our developed LIG devices, barriers to commercial adoption of this technology still exist. Generally, we have showcased the capabilities of the materials. While we have performed interferent studies for IL-6 detection and used an artificial sweat solution for determining selectivity towards Tyrosine, these are lab-prepared solutions. Real solutions are still more complex matrices. For a commercial biosensor, more thorough experimentation in real solutions is necessary. There are a number of questions of device design which still must be addressed: precise control of electrode design, in terms of delimiting a repeatable electrode area; integration with on-device circuitry to minimise access resistance to the electrode surface, while minimising the contact resistance. Routes for controlling the active area in a precise repeatable manner include depositing a bespoke insulating mask onto the device, or printing a polymer mask. The method that we currently use for integration of LIG devices with external instrumentation is by using conductive silver paint and flat clips. Within our group, progress is being made towards creating devices which can be contacted through the material.

6.3 Publications

1. **Vaughan, E.**, Santillo, C., Setti, M., Larrigy, C., Quinn, A. J., Gentile, G., Lavorgna, M., Iacopino, D. *Sustainable Laser-Induced Graphene Electrochemical Sensors from Natural Cork for Sensitive Tyrosine Detection.* Advanced Sensor Research, 2023. https://doi.org/10.1002/adsr.202300026

2. Larrigy, C., Burke, M., Imbrogno, A., **Vaughan, E.**, Santillo, C., Lavorgna, M., Sygellou, L., Paterakis, G., Galiotis, C., Iacopino, D., Quinn, A. J., *Porous 3D Graphene from Sustainable Materials: Laser Graphitization of Chitosan*. Adv. Mater. Technol. 2022, 2201228. https://doi.org/10.1002/admt.202201228
3. Paterakis George, **Eoghan Vaughan**, Dinesh R. Gawade, Richard Murray, George Gorgolis, Stefanos Matsalis, George Anagnostopoulos, John L. Buckley, Brendan O'Flynn, Aidan J. Quinn, Daniela Iacopino, and Costas Galiotis; *Highly Sensitive and Ultra-Responsive Humidity Sensors Based on Graphene Oxide Active Layers and High Surface Area Laser-Induced Graphene Electrodes* Nanomaterials 2022, 12, no. 15: 2684. https://doi.org/10.3390/nano12152684
4. Murray, R., O'Neill, O., **Vaughan, E.,** Iacopino, D., Blake, A., Lyons, C., O'Connell, D., O'Brien, J., Quinn, A. J.; *Direct-write formation of integrated bottom contacts to laser-induced graphene-like carbon*. Nanotechnology 2022, 33, 405204. https://doi.org/10.1088/1361-6528/ac7c7b
5. Julia Madden, **Eoghan Vaughan**, Michael Thompson, Alan O' Riordan, Paul Galvin, Daniela Iacopino, Sofia Rodrigues Teixeira; *Electrochemical sensor for enzymatic lactate detection based on laser-scribed graphitic carbon modified with platinum, chitosan and lactate oxidase*. Talanta, Volume 246, 2022, 123492, ISSN 0039-9140, https://doi.org/10.1016/j.talanta.2022.123492
6. Alessandra Imbrogno, Jahidul Islam, Chiara Santillo, Rachele Castaldo, Labrini Sygellou, Cathal Larrigy, Richard Murray, **Eoghan Vaughan**, Md. Khairul Hoque, Aidan J. Quinn, and Daniela Iacopino; *Laser-Induced Graphene Supercapacitors by Direct Laser Writing of Cork Natural Substrates.* ACS Applied Electronic Materials 2022, 4 (4), 1541-1551 https://doi.org/10.1021/acsaelm.1c01202

7. **Eoghan Vaughan,** Tan, Pei Shee, Jahidul Islam, Niall Burke, Daniela Iacopino, and Joanna B. Tierney. 2021. *Laser Scribing Fabrication of Graphitic Carbon Biosensors for Label-Free Detection of Interleukin-6.* Nanomaterials 11, no. 8: 2110. https://doi.org/10.3390/nano11082110

8. **Eoghan Vaughan**, Cathal Larrigy, Micheal Burke, Labrini Sygellou, Aidan J. Quinn, Costas Galiotis, Daniela Iacopino. *Visible Laser Scribing Fabrication of Porous Graphitic Carbon Electrodes: Morphologies, Electrochemical Properties, and Applications as Disposable Sensor Platforms.* ACS Applied Electronic Materials **2020** *2* (10), 3279-3288. https://doi.org/10.1021/acsaelm.0c00612

9. Micheal Burke, Cathal Larrigy, **Eoghan Vaughan**, George Paterakis, Labrini Sygellou, Aidan J. Quinn, Grégoire Herzog, Costas Galiotis, Daniela Iacopino *Fabrication and Electrochemical Properties of Three-Dimensional (3D) Porous Graphitic and Graphenelike Electrodes Obtained by Low-Cost Direct Laser Writing Methods.* ACS Omega 2020 5 (3), 1540-1548: https://10.1021/acsomega.9b03418